DESIGN AND NUMERICAL SIMULATION OF TWO DIMENSIONAL ULTRA COMPACT COMBUSTOR MODEL SECTIONS FOR EXPERIMENTAL OBSERVATION OF CAVITY-VANE FLOW INTERACTIONS

THESIS

David S. Moenter, Lieutenant Commander, USN

AFIT/GAE/ENY/06-S07

DEPARTMENT OF THE AIR FORCE
AIR UNIVERSITY

AIR FORCE INSTITUTE OF TECHNOLOGY

Wright-Patterson Air Force Base, Ohio

The views expressed in this thesis are those of the author and do not reflect the official policy or position of the United States Air Force, United States Navy, Department of Defense, or the United States Government.

AFIT/GAE/ENY/06-S07

DESIGN AND NUMERICAL SIMULATION OF TWO-DIMENSIONAL ULTRA COMPACT COMBUSTOR MODEL SECTIONS FOR EXPERIMENTAL OBSERVATION OF CAVITY-VANE FLOW INTERACTIONS

THESIS

Presented to the Faculty

Department of Aeronautics and Astronautics

Graduate School of Engineering and Management

Air Force Institute of Technology

Air University

Air Education and Training Command

In Partial Fulfillment of the Requirements for the

Degree of Master of Science in Aeronautical Engineering

David S. Moenter, BS

Lieutenant Commander, USN

September 2006

AFIT/GAE/ENY/06-S07

DESIGN AND NUMERICAL SIMULATION OF TWO-DIMENSIONAL ULTRA COMPACT COMBUSTOR MODEL SECTIONS FOR EXPERIMENTAL OBSERVATION OF CAVITY-VANE FLOW INTERACTIONS

David S. Moenter, BS
Lieutenant Commander, USN

Approved:

_____	_____
Dr. Ralph A. Anthenien (Chairman)	date
_____	_____
LtCol Raymond Maple, USAF (Member)	date
_____	_____
Dr. Mark Reeder (Member)	date

AFIT/GAE/ENY/06-S07

Abstract

An improved computational fluid dynamics (CFD) model was developed for numerical simulation of the Ultra Compact Combustor (UCC) concept to enhance turbulent flow characterization of the circumferentially traveling, centrifugal-force enhanced combustion, cavity flow into the engine main flow passage via a radial cavity in the turbine axial guide vanes. The CFD model uses a dense grid on a 60^o periodic, axi-symmetric combustor section, with the RNG k-ε turbulence model to resolve turbulent flow details. An overall analysis and performance evaluation of the experimentally tested UCC configuration and an axially shortened cavity baseline configuration was conducted at various experimentally documented operating conditions.

This CFD model is then applied in designing two sector test rigs to simulate a portion of the UCC flow to allow optical access to the cavity-vane flow interaction, an area inaccessible on a full test rig. The design steps include a 2-D planar, periodic model eliminating centrifugal-force effects and the design of two non-periodic test sections with an extended cavity simulating mass entrainment before interacting with the cavity-vane and main flow. The planar and curved sector rigs were evaluated and cavity flow parameters analyzed at experimental and atmospheric conditions for comparison with the 3-D baseline configuration.

Acknowledgements

Most importantly, I am indebted to my loving wife, whose patience and support throughout my AFIT Master's program and this research has been incredible. Also to my three wonderful young children, whose curiosity and enthusiasm is always inspiring.

I am indebted to Dr. Ralph Anthenien, who as my thesis advisor, who not only provided the technical expertise and moral support in guiding me through the research of this complicated topic, but also allowed me the freedom and leeway to take on a few unplanned avenues in the research, resulting in some findings that would otherwise have not been discovered.

LtCol Raymond Maple, for always being available to lend an ear and an idea during the long hours spent making the various CFD software programs work for me.

Last, but certainly not least, I am very much indebted to 2ndLt Jonathon Anisko and Capt Roger Greenwood, whose preceding CFD research on the UCC laid the groundwork which my research merely built upon.

David S. Moenter

Table of Contents

Page

Abstract iv

Acknowledgements v

Table of Contents vi

List of Figures ix

List of Tables xiv

List of Symbols xvi

List of Abbreviations xix

I. .....Introduction and Overview 1
- 1.1 Research Perspective 1
- 1.2 Ultra Compact Combustor Concept 2
- 1.3 Combustor Design Criteria 5
- 1.4 Thesis Research Outline 5

II. .....Background and Theory 8
- 2.1 Literature Review 8
  - 2.1.1 Conventional Combustor Layout. 8
  - 2.1.2 Inter-Turbine-Burner and Continuous-Turbine-Burner Performance Increases. 9
  - 2.1.3 Centrifugal Force Combustion. 10
  - 2.1.4 Trapped Vortex Combustion. 11
  - 2.1.5 UCC Experimental Research. 12
  - 2.1.6 UCC CFD Research. 13
- 2.2 Computational Fluid Dynamics 15
  - 2.2.1 CFD Software. 15
  - 2.2.2 Numerical Grid Considerations. 16
  - 2.2.3 Turbulence Modeling. 17
  - 2.2.4 Wall Functions. 20
  - 2.2.5 Non-premixed Combustion and Species Modeling. 23
  - 2.2.6 NO_X Modeling. 27
  - 2.2.7 FLUENT Post-processing. 29
- 2.3 Heat Transfer 30
- 2.4 Combustor Performance Criteria 31
  - 2.4.1 Combustor Loading Parameter. 31
  - 2.4.2 Pressure Loss. 32
  - 2.4.3 Emissions. 32
  - 2.4.4 Combustion Efficiency. 33
  - 2.4.5 Outlet Temperature Distribution. 34
  - 2.4.6 Cavity G-loading. 35

Page

2.5 Design Considerations for an Experimental Combustor Sector Rig 35
2.5.1 UCC Flow Area of Interest. 35
2.5.2 Recreating 360 degree UCC Cavity Flow Characteristics. 36
2.5.3 Laser Diagnostic Considerations. 38

III. .....Methodology 39
3.1 Design and Evaluation Process Outline 39
3.2 Models and CFD Grid Development 40
3.2.1 Configuration Model Design. 40
3.2.2 Grid Construction Techniques. 46
3.2.3 Coarse versus Dense Grid. 47
3.2.4 Summary of Configurations and Numerical Models. 51
3.3 Numerical Methods 52
3.3.1 Experimental and Numerical Operating Conditions. 52
3.3.2 Boundary Conditions. 53
3.3.3 Periodic Boundaries. 55
3.3.4 Turbulence Modeling. 56
3.3.5 Combustion and Species Transport Modeling. 56
3.3.6 Fuel Injection. 57
3.3.7 Pollutant Modeling 59
3.3.8 Solver and Solution Procedure 60
3.3.6 Solution Convergence Criteria 60
3.4 Combustor Configuration Performance Evaluation and Comparison 61
3.4.1 Qualitative Measures of Performance Comparison. 61
3.4.2 Quantitative Measures of Performance Comparison. 61

IV. .....Results and Discussion 63
4.1 3-D Experimental Configuration, Improved CFD Model Evaluation and Comparison with Experimental and Coarse Grid CFD Data 63
4.1.1 Performance and Emissions Data Evaluation. 64
4.1.2 Overall Solution Visualization. 66
4.1.3 Cavity Flow, G-loading, and Cavity-vane Interaction Evaluation. 71
4.1.4 Exhaust Temperature Distribution Evaluation 77
4.1.5 Standard k-ε and RNG k-ε Model Comparison. 80
4.1.6 Dense Grid Effects. 82
4.1.7 Validity of Improved CFD Model. 85
4.2 3-D Short Baseline Axi-symmetric Model 85
4.2.1 Performance and Emissions Data Evaluation. 86
4.2.2 Overall Solution Visualization. 87
4.2.3 Cavity Flow, G-loading, and Cavity-vane Interaction Evaluation. 90
4.2.4 Exhaust Temperature Distribution Evaluation 99
4.3 2-D Short Planar Baseline Model 101
4.3.1 Performance and Emissions Data Evaluation. 102

Page

4.3.2 Overall Solution Visualization. 103
4.3.3 Cavity Flow and Cavity-vane Interaction Evaluation. 105
4.3.4 Exhaust Temperature Distribution Evaluation. 109
4.4 2-D Curved Cavity Sector Rig 111
4.4.1 Performance and Emissions Data Evaluation. 112
4.4.2 Overall Solution Visualization. 113
4.4.3 Cavity flow, G-loading, and Cavity-vane Interaction Evaluation. 116
4.4.4 Exhaust Temperature Distribution Evaluation. 120
4.5 2-D Planar Cavity Sector Rig 121
4.5.1 Performance and Emissions Data Evaluation. 122
4.5.2 Overall Solution Visualization. 123
4.5.3 Cavity flow and Cavity-vane Interaction Evaluation. 125
4.5.4 Exhaust Temperature Distribution Evaluation. 129

V. Conclusions 130
5.1 Overview of Research Results 130
5.1.1 CFD Modeling. 130
5.1.2 3-D UCC Flow Analysis. 131
5.1.3 Design of UCC Sector Rigs. 132
5.2 Future Research 133

Appendix A: 3-D Baseline Configuration Flow Cutaways ATM2 134

Appendix B: 2-D Curved Cavity Sector Rig Flow Cutaways ATM2 136

Appendix C: 2-D Planar Cavity Sector Rig Flow Cutaways ATM2 138

Bibliography 140

Vita 142

List of Figures

Page

Figure 1: Ultra Compact Combustor Concept. (Greenwood, 2005:1-4) 4

Figure 2: Ultra Compact Combustor Operational Concepts (Anthenien et al, 2001:6) 4

Figure 3: T-S diagram comparison of conventional combustor/afterburner engine (light dashed line) with addition of a turbine burner to engine (dark solid line), for improved cycle efficiency. Used without permission. (Sirignano and Liu, 1999:2) 10

Figure 4: Trapped Vortex Combustion Concept, (Greenwood, 2005:1-2). 12

Figure 5: Original UCC experimental rig schematic, with support spider, no axial vane. Flow-path is left to right. (Zelina, Sturgess, and Shouse, 2004) 13

Figure 6: Curved sector rig schematic illustrating concept of extended cavity length to reproduce re-circulating cavity mass flow and combustion processes. 37

Figure 7: UCC 1.5-inch short cavity baseline model in *Solidworks.* 41

Figure 8: Basic design of 2-D 1.5-inch flat cavity, periodic UCC model with inlet, outlet, and cavity walls excluded. 42

Figure 9: General design of UCC curved cavity sector rig, shown excluding main flow top walls. 44

Figure 10: General design of UCC flat sector rig, shown excluding main flow top walls. 44

Figure 11: Coarse grid of 1.875 inch cavity UCC configuration from Anisko's research. 48

Figure 12: Improved dense grid of 1.875 inch cavity UCC configuration. 49

Figure 13: Wall y* contours of UCC long cavity configuration at LMLP operating condition. Note darkest blue areas are y*<11.225. 50

Figure 14: Fuel particle tracks of 70 μm mean diameter injection in experimental configuration, LMLP condition solution, colored by mean diameter (m). 58

Figure 15: Fuel particle tracks of 50 μm mean diameter injection in experimental configuration, LMLP condition solution, colored by mean diameter (m). 58

Page

Figure 16: Location of visualization and evaluation planes on 3-D experimental configuration, LMLP condition, with contours of temperature (K) shown. Combustor flow is right to left. 62

Figure 17: Velocity vectors colored by temperature (K) for the experimental configuration, LMLP condition, RNG *k*-*ε* turbulence model, viewed facing exhaust outlet. 67

Figure 18: Contours of velocity magnitude (m/s) on experimental configuration, LMLP condition, RNG *k*-*ε* turbulence model. 69

Figure 19: Contours of turbulence intensity (%, read as e+01) on experimental configuration, LMLP condition, RNG *k*-*ε* turbulence model. 69

Figure 20: Velocity vectors colored by temperature (K) for the experimental configuration, LMLP condition, standard *k*-*ε* turbulence model. 70

Figure 21: Contours of turbulence intensity (%, read as e+01) on experimental configuration, LMLP condition, standard *k*-*ε* turbulence model. 71

Figure 22: Cavity fuel plane velocity vectors colored by temperature (K) for experimental configuration, LMLP, RNG *k*-*ε* model (top) and standard *k*-*ε* (bottom), viewed from exhaust with swirl clockwise. 73

Figure 23: Tangential velocity (m/s) contours on U_θ plane, experimental configuration, LMLP, RNG *k*-*ε* (left) and standard *k*-*ε* (right) turbulence models. Cavity flow is out of page. 74

Figure 24: Circumferential averaged tangential velocities plotted by radius on U_θ plane for experimental configuration. 76

Figure 25: Circumferential averaged g-loading plotted by radius on U_θ plane for experimental configuration. 76

Figure 26: Velocity vectors colored by temperature (K) for cavity-vane plane on experimental configuration, LMLP, RNG *k*-*ε* model. Cavity flow (upper half) is out of page, main flow across RVC (lower half) is right to left. 77

Figure 27: Temperature (K) contours for outlet plane on experimental configuration, LMLP, RNG k-ε (left) and standard k-ε (right) turbulence models. Outlet plane viewed from behind combustor, cavity swirl is clockwise. 79

Figure 28: Circumferential averaged temperature plotted by normalized radius for outlet plane of experimental configuration. 80

Figure 29: Velocity vectors colored by temperature (K) on fuel plane for experimental configuration, LMLP, coarse grid and model, adapted from Anisko's research with permission. Viewed from combustor exhaust, cavity swirl is clockwise. 83

Page

Figure 30: Temperature (K) contours for outlet plane on experimental configuration, LMLP, coarse grid and model, adapted from Anisko's research with permission. Viewed from rear of combustor, swirl is clockwise. 83

Figure 31: Circumferential radial averages of temperature plotted by normalized radius for outlet plane of experimental configuration, LMLP condition, coarse grid and model, adapted from Anisko's research with permission. 84

Figure 32: Contours of temperature (K) for the 3-D baseline configuration, LMLP condition, viewed from exhaust outlet, main mass flow right to left, out of page. 88

Figure 33: Contours of velocity magnitude (m/s) on 3-D baseline configuration, LMLP condition. 89

Figure 34: Contours of turbulence intensity (%, read as e+01) on 3-D baseline configuration, LMLP condition. 89

Figure 35: Cavity fuel plane velocity vectors colored by temperature (K) for 3-D baseline configuration, LMLP condition, viewed from exhaust with swirl clockwise. 92

Figure 36: Cavity plane velocity vectors colored by temperature (K) for axial planes coincident with forward cavity air inlets (top) and aft cavity air inlets (bottom) for 3-D baseline configuration, LMLP condition, viewed from exhaust with swirl clockwise. 93

Figure 37: Circumferential averaged tangential velocities plotted by radius on U_θ plane for baseline configuration. 96

Figure 38: Circumferential averaged g-loading plotted by radius on U_θ plane for 3-D baseline configuration. 96

Figure 39: Velocity vectors colored by temperature (K) for cavity-vane plane on 3-D baseline configuration, LMLP condition. 98

Figure 40: 3-D baseline configuration, HMHP condition, cavity fuel and cavity-vane planes velocity vectors with temperature (K). Flow swirls from clockwise on cavity fuel plane. 98

Figure 41: Circumferential averaged temperature plotted by normalized radius for outlet plane of 3-D baseline configuration. 101

Figure 42: Contours of temperature (K) and 2-D planar baseline configuration layout, LMLP condition. Translational periodic boundary surfaces shown at ends of cavity. 104

Figure 43: Contours of velocity magnitude (m/s) (left) and turbulence intensity (%, read as e+01) (right) for 2-D planar baseline configuration, LMLP condition. 104

Page

Figure 44: Cavity fuel plane (top, cavity flow left to right) and cavity-vane plane (bottom, cavity flow out of page) velocity vectors colored by temperature (K) for 2-D planar baseline configuration, LMLP condition. 108

Figure 45: Circumferentially averaged x-component velocities plotted by cavity height on U_θ plane for 2-D planar baseline configuration. 109

Figure 46: Contours of temperature (K) for the 2-D curved sector rig, LMLP condition. Viewed from exhaust, main channel flow out of page, cavity flow is clockwise left to right. 112

Figure 47: Contours of velocity magnitude (m/s) (top) and turbulence intensity (%, read as e+01) (bottom) for 2-D curved sector rig, LMLP condition. 115

Figure 48: Comparison of 2-D curved cavity sector rig cavity fuel plane (top, cavity flow clockwise left to right) and 3-D baseline configuration cavity fuel plane (bottom, cavity flow clockwise left to right). Velocity vectors colored with temperature (K), viewed from exhaust, LMLP condition. 117

Figure 49: Comparison of 2-D curved cavity sector rig cavity-vane plane (top, cavity flow out of page) and 3-D baseline configuration cavity-vane plane (bottom, cavity flow out of page). Velocity vectors colored with temperature (K), LMLP condition. 118

Figure 50: Circumferential averaged tangential velocities plotted by radius on U_θ plane for 2-D curved sector rig. 120

Figure 51: Circumferential averaged g-loading plotted by radius on U_θ plane for 2-D curved sector rig. 120

Figure 52: Contours of temperature (K) for 2-D planar sector rig, LMLP condition. 122

Figure 53: Contours of velocity magnitude (m/s) (top) and turbulence intensity (%, read as e+01) (bottom) for 2-D planar sector rig, LMLP condition. 124

Figure 54: Comparison of 2-D planar sector rig cavity fuel plane (top, cavity flow left to right) and 3-D baseline configuration cavity fuel plane (bottom, cavity flow clockwise left to right). Velocity vectors colored with temperature (K), viewed from exhaust, LMLP condition. 126

Figure 55: Comparison of 2-D planar sector rig cavity-vane plane (top, cavity flow out of page) and 3-D baseline configuration cavity-vane plane (bottom, cavity flow out of page). Velocity vectors colored with temperature (K), LMLP condition. 127

Figure 56: Circumferential averaged tangential velocities plotted by radius on U_θ plane for 2-D planar sector rig. 128

Page

Figure 57: Contours of temperature (K) on 3-D baseline configuration, ATM2 operating condition. 134

Figure 58: Contours of turbulence intensity (%, read as e+01) on 3-D baseline configuration, ATM2 operating condition. 134

Figure 59: Velocity vectors with temperature (K) on cavity fuel plane for 3-D baseline configuration, ATM2 operating condition. Viewed from exhaust, cavity flow is clockwise. 135

Figure 60: Velocity vectors with temperature (K) on cavity-vane plane for 3-D baseline configuration, ATM2 operating condition. Cavity flow is out of page. 135

Figure 61: Contours of temperature (K) on 2-D curved cavity sector rig, ATM2 operating condition. 136

Figure 62: Contours of turbulence intensity (%, read as e+01) on 2-D curved cavity sector rig, ATM2 operating condition. 136

Figure 63: Velocity vectors with temperature (K) on cavity fuel plane for 2-D curved cavity sector rig, ATM2 operating condition. Viewed from exhaust, cavity flow is clockwise, left to right. 137

Figure 64: Velocity vectors with temperature (K) on cavity-vane plane for 2-D curved sector rig , ATM2 operating condition. Cavity flow is out of page. 137

Figure 65: Contours of temperature (K) for 2-D planar cavity sector rig, ATM2 operating condition. 138

Figure 66: Contours of turbulence intensity (%, read as e+01) for 2-D planar cavity sector rig, ATM2 operating condition. 138

Figure 67: Velocity vectors with temperature (K) on cavity fuel plane for 2-D planar cavity sector rig, ATM2 operating condition. Viewed from exhaust, cavity flow is left to right. 139

Figure 68: Velocity vectors on cavity-vane plane for 2-D planar cavity sector rig, ATM2 operating condition. Cavity flow is out of page. 139

List of Tables

Page

Table 1: Numerical Model Configurations. 51

Table 2: Experimental Operating Conditions on Full UCC Test Model. 52

Table 3: Operating Conditions for CFD 3-D, 60-degree models..... 53

Table 4: Fuel Droplet Spray Model. 59

Table 5: Emissions and efficiency performance data for 3-D Experimental Configuration (1.875 inch cavity), comparing experimental data, coarse grid solution, and dense grid solution. 65

Table 6: Cavity flow parameters for experimental configuration, with mass weighted average velocities for U_θ plane. 72

Table 7: Exhaust temperature pattern and profile factor data for experimental configuration. 78

Table 8: Emissions and efficiency performance data for 3-D Baseline Configuration (1.5 inch cavity, 45^o inlets) compared with 3-D Experimental Configuration. 86

Table 9: Cavity flow parameters for 3-D baseline configuration with mass weighted average velocities for U_θ plane. 91

Table 10: Exhaust temperature pattern and profile factor data for 3-D baseline configuration. 100

Table 11: Emissions and efficiency performance data for 2-D planar baseline configuration (1.5 inch cavity), comparing to 3-D baseline configuration solution data. 103

Table 12: Cavity flow parameters for 2-D planar baseline configuration, with mass weighted average velocities for U_θ plane, comparing with 3-D baseline configuration solution data..... 106

Table 13: Exhaust temperature pattern factor data for 2-D planar baseline configuration, comparing with 3-D baseline configuration solution data..... 110

Table 14: Emissions and performance data for 2-D curved sector rig, comparing with 3-D baseline configuration data. 113

Table 15: Cavity flow parameters for 2-D curved sector rig, with average velocities for U_θ plane, compared with 3-D baseline configuration. 116

Table 16: Exhaust temperature pattern factor data for 2-D curved sector rig compared with 3-D baseline configuration. 121

Table 17: Emissions and efficiency performance data for 2-D planar sector rig, compared with 3-D baseline configuration. 123

Page

Table 18: Cavity flow parameters for 2-D planar sector rig, with average velocities for U_θ plane, comparing with 3-D baseline configuration..... 125

Table 19: Exhaust temperature pattern factor data for 2-D planar sector rig, comparing with 3-D baseline configuration..... 129

List of Symbols

Symbol	
$C_{12}H_{23}$	Primary hydrocarbon modeled for kerosene fuel
CO	Carbon Monoxide
CO_2	Carbon Dioxide
D	Diameter
f	Mixture fraction, cell based
$\overline{f}$	Mean mixture fraction
$\overline{f}^{'2}$	Mean mixture variance
F_D	Drag force for Discrete Phase Model fuel particle
g	Centrifugal force
g_o	Gravitational constant
G_b	Term for generation turbulence kinetic energy due to buoyancy for k-ε transport equations
G_k	Term for generation of turbulence kinetic energy due to mean velocity gradients for k-ε transport equations
H	Instantaneous enthalpy
$\overline{h}$	Convective heat transfer coefficient
k	Turbulent kinetic energy
k	Conductive heat transfer coefficient
LDV	Laser doppler velocimeter
$\dot{m}_{cav}$	Mass flow rate, cavity air inlets
$\dot{m}_{cavplane}$	Mass flow rate of cavity measured across cavity cross-section plane
$\dot{m}_{main}$	Mass flow rate, combustor inlet plane
MM	Molecular Mass
N_2	Nitrogen
NO_x	Oxides of Nitrogen
Nu_D	Nusselt number
O_2	Oxygen

Symbol

Q_b	Thermodynamic cycle heat addition at combustor
Q_{ab}	Thermodynamic cycle heat addition at afterburner
Q_{tb}	Thermodynamic cycle heat addition at power turbine
p_3	Combustor inlet pressure
p_4	Combustor outlet pressure
p_{abs}	Absolute pressure
p_{op}	Combustor operating pressure
Pr	Prandtl number
r	Air-to-fuel ratio mass basis
R	Cavity radius
Ra_D	Rayleigh number
R_ε	Renormalizing group term in ε transport equation
Re	Reynolds number
S_B	Bubble flame-speed
S_ε	User defined source term for ε transport equation
S_h	Source term for heat transfer with walls or dispersed phase
S_k	User defined source term for k transport equation
S_L	Laminar flame-speed
T-S	Temperature-Entropy
T_s	Surface temperature
T_∞	Free-stream temperature
T_{max}	Maximum temperature on exhaust outlet plane
T_{mr}	Maximum mean circumferential temperature on exhaust outlet plane
T_3	Combustor inlet temperature
T_4	Combustor outlet temperature
U_r	Radial velocity component
U_θ	Tangential velocity component
UHC	Unburned hydrocarbons

Symbol

V	Cavity volume
y*	Wall unit
y_υ	Viscous sub-layer thickness
Y_M	Term for contribution of the fluctuating dilation in compressible turbulence to the overall dissipation rate for k-ε transport equations
α_ε	Inverse effective Prandtl number, ε equation
α_k	Inverse effective Prandtl number, k equation
β	Shape function for assumed probability density function in non-premixed combustion species transport model based on mean mixture fraction and mixture fraction variance
Δs	Grid spacing
ε	Turbulent kinetic energy rate of dissipation
μ	Viscosity
μ_t	Effective turbulent viscosity
η_b	Combustion efficiency
φ_{cav}	Cavity equivalence ratio
φ_{ovr}	Overall equivalence ratio
ρ	Density

List of Abbreviations

Abbreviation	
AFSC	Accurate Flow Solver Computer Code
AFIT	Air Force Institute of Technology
AFRL	Air Force Research Laboratory
ATM1	First atmospheric pressure operating condition
ATM2	Second atmospheric pressure operating condition
CIAC	Cavity-in-a-cavity
CFD	Computational Fluid Dynamics
CLP	Combustor loading parameter
CTB	Continuous turbine burner
DPM	Discrete Phase Model
EI	Emissions Index
HMHP	High mass, high pressure experimental operating condition
ITB	Inter-turbine burner
LMLP	Low mass, low pressure experimental operating condition
LMMP	Low mass, medium pressure experimental operating condition
PDF	Assumed-shape probability density function
ppm	Parts per million
RFL	Rich flammability limit
RNG	Renormalization group theory
RVC	Radial Vane Cavity
TV	Trapped Vortex
TVC	Trapped Vortex Combustion
UCC	Ultra Compact Combustor
2-D	Two-dimensional
3-D	Three-dimensional

DESIGN AND NUMERICAL SIMULATION OF TWO-DIMENSIONAL ULTRA COMPACT COMBUSTOR MODEL SECTIONS FOR EXPERIMENTAL OBSERVATION OF CAVITY-VANE FLOW INTERACTIONS

I. Introduction and Overview

1.1 Research Perspective

The modern age of aircraft design demands the highest performance be attained while meeting the most stringent environmental demands, all achieved in a cost effective manner. For aircraft engine development, this translates into lighter, more powerful and efficient engines, with minimal environmental impact to meet current and future stringent emissions standards. Previous decades have seen remarkable improvement in performance from all aircraft engine components, to include inlets, compressors, combustors, and power turbines, yet the recent rate of improvement in performance has been decreasing as physical and material limits have been reached. Additionally, the overall form of the gas turbine engine has remained relatively constant.

Modern design techniques have also evolved and improved. Improved computer processing speed, combined with vastly increased theoretical knowledge and numerical methods, have resulted in computer modeling for most disciplines being the norm. In the areas of aeronautics, engine design, and combustion, Computational Fluid Dynamics

(CFD) and numerical chemical simulations are now primary tools used in the research and development process to accompany the traditional experimental methods in an overall design effort. While CFD and numerical methods do not as yet provide fully accurate solutions to all problems, they provide significant cost savings when solutions can be compared and validated against experimental results to provide an effective and practical design tool.

To focus on gas turbine engine combustors, modern engines all achieve over 99% combustion efficiency, but are often limited in providing more power by material and temperature limitations in the power turbine sections they drive. Modern combustors, utilizing the traditional axial flow pattern to provide the required fuel burning residence time and length prior to the power turbine section, contribute significantly to engine length and weight. The Ultra Compact Combustor (UCC) is a gas turbine engine combustor concept with potential to address many areas of performance improvement by using circumferential flow and centrifugal forces for combustion, thereby reducing the combustor's length and weight and increasing engine performance through increased thrust to weight ratio.

1.2 Ultra Compact Combustor Concept

The UCC is a recent concept developed by the US Air Force Research Laboratory (AFRL), Propulsion Directorate at Wright-Patterson AFB, Ohio to further advances in aircraft engine efficiency, weight decrease, and improved emissions as either a primary combustor or a secondary inter-turbine combustor. The UCC is based on two main principles, centrifugal-force effects to increase flame propagation rates (Lewis, 1973) and

Trapped Vortex Combustion (TVC) (Hsu et al, 1998; Roquemore et al, 2001), to form the primary combustion zone in a cavity flowing circumferentially around the main flow, illustrated in Figures 1 and 2. At the outer circumference of the cavity, atomized fuel is injected and angled air jet inlets accelerate the cavity flow, imparting a centrifugal-force to rapidly mix and burn the fuel-air mixture. The cavity is open inward to the main flow in the axial direction, where the TVC concept and buoyancy effects are utilized to transport the hot combustion products from the swirling cavity flow into the main flow. Additional transport is provided by an additional vortex and low pressure turbulent wake area created with a radial vane cavity (RVC) in the axial support vane in the main flow area. The RVC provides an intermediate combustion zone, while leading to the main flow dilution zone.

The full UCC is comprised of a cylindrical center-body, with six axial aerodynamic vanes to support the cavity and outer walls. Each vane has its RVC on the down-flow side, aligned in the radial direction with the overlying cavity. The cavity is fed by six fuel injectors at the outer circumference, directly over each vane, and a total of 24 angled air inlets, four equally spaced around each fuel injector. The full UCC can be divided into six equal wedge sections. Previous CFD studies have been conducted using this 60^{o} periodic sector model.

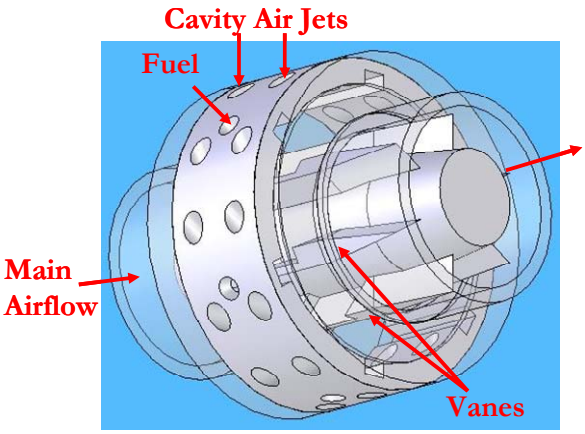

Figure 1: Ultra Compact Combustor Concept. (Greenwood, 2005:1-4)

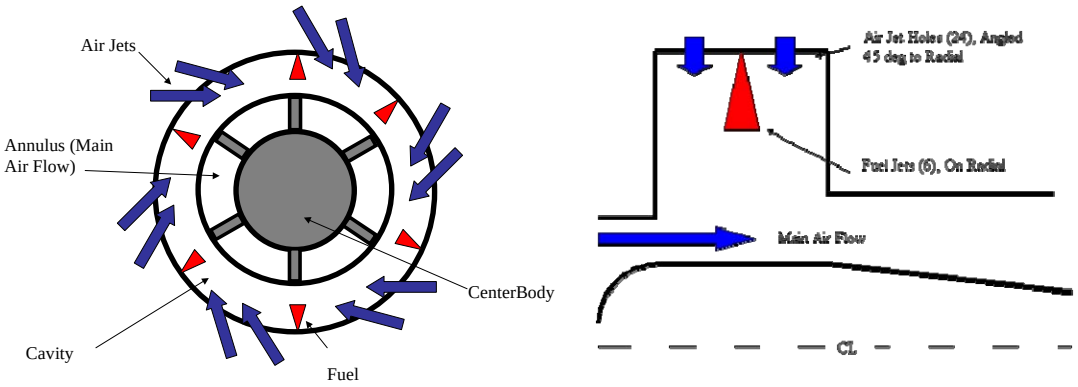

Figure 2: Ultra Compact Combustor Operational Concepts (Anthenien et al, 2001:6)

Various experimental and numerical simulations to date have demonstrated UCC combustion efficiency of up to 99%, with cavity velocities ranging from 10-45 m/s for g-loadings from 300-4000g's (Anthenien et al, 2001:2). It is estimated a UCC can reduce a jet engine combustor length by 33% while maintaining high efficiency.

This concept is foreseen to be used not only as a primary jet engine combustor, but also as a method to incorporate inter-turbine burning, or a reheat cycle, in the power

turbine section to improve overall cycle efficiency, decrease maximum temperatures, and ease material constraints (Sirignano and Liu, 1999, 2000).

1.3 Combustor Design Criteria

Designing and evaluating a combustor entails meeting certain requirements and standards for the proposed design to succeed. Lefebvre provides eleven gas turbine combustor requirements to evaluate the merits of a design (Lefebvre, 1983:4). Four of these will be the used as evaluation criteria during this research effort. High combustion efficiency, low pressure loss, outlet temperature distribution, and low emissions of unburned fuel and gaseous pollutant species will be analyzed to quantify the results, while flow visualization will also be used to qualify and analyze the designs. Additionally, modern and future emissions standards need to be met or addressed. The end goal is to produce a reliable combustor of low size and weight with operational flexibility to meet the remaining design requirements.

1.4 Thesis Research Outline

Current UCC research efforts are primarily focused on optimizing the outlet temperature distribution, with the main focus on understanding and controlling the interaction of the turbulent flow occurring between the cavity and main flow areas, with a particular emphasis on the axial aerodynamic vane and effects of the RVC in pulling the flow from the cavity. This thesis research topic is aimed directly at providing a better understanding of these phenomena.

Normally, modern experimental measurement techniques of hot wires or non-intrusive laser diagnostics are used to measure and analyze a complex flow. However, due to the high temperatures in a combustor, hot wires are not feasible. Additionally, due to the inherent 360 degree axi-symmetric nature of a full experimental model and the configuration of this combustor, laser diagnostic instruments cannot see below the inner radius of the cavity and into the area of interest. The goal of this research is to design one-sixth sector, two-dimensional (2-D, no circular or periodic flow around the full circumference), experimental models to replicate the flow characteristics of the full configuration, but utilizing flat quartz walls in the main flow area to enable laser diagnostic instruments optical access to analyze the interaction between the cavity and main flow through the RVC. Numerical simulation results are to be provided for comparison. Subsequent experimental testing is intended to be conducted in the Air Force Institute of Technology (AFIT) atmospheric pressure combustion laboratory.

Two models will be proposed and studied, one with a curved cavity leading to the intersection with the main flow to completely replicate the UCC combustion flow, and a second with a flat cavity leading to main flow intersection, eliminating the centrifugal and buoyancy forces in the combusting flow, leaving only cross flow trapped vortex interaction. This design process is based upon, and follows from, previous AFIT CFD research of the UCC (Greenwood, 2005; Anisko, 2006) utilizing *FLUENT* commercial CFD software to model and analyze various UCC configurations and operating conditions. Unfortunately, in the design process, discrepancies and shortcomings with previous CFD models were discovered. So, an additional part of this research became

improving and validating the 3-dimensional (3-D) axi-symmetric CFD model against experimental results and performing CFD simulations for the desired UCC configuration on this 3-D axi-symmetric model.

As such, this thesis will present design criteria, modeling conditions, results and analysis of the following: validation of an improved 3-D axi-symmetric CFD model by comparison of the experimental configuration data to actual experimental results, validation of a baseline 3-D axi-symmetric model as basis for comparison of subsequent models, CFD analysis of a 2-D flat cavity periodic model, design and CFD analysis of a 2-D flat cavity sector experimental test model, and design and CFD analysis of a curved cavity sector experimental test model.

II. Background and Theory

2.1 Literature Review

2.1.1 Conventional Combustor Layout. A conventional jet engine combustion chamber is laid out along the engines axial length, utilizing axial distance to provide chemical residence time for the combustion reaction. A typical combustor design is described in the *Gas Turbine Combustion* (Lefebvre, 1983:2-12), and summarized here.

After a diffuser to slow the incoming air velocity, an inner liner or combustion can, of several different possible configurations, is positioned in the flow within the air casing. The inner liner has many slots and holes through its surface, to allow air to enter at different points into the primary, intermediate, and dilution zones and to provide for liner cooling. Fuel is injected at the start of the primary zone, in an area protected from direct airflow.

The primary zone functions to anchor the flame and allow time, temperature, and turbulence to mix the fuel and air, to achieve near complete combustion. The intermediate zone next provides more air injection and an additional length to allow further residence time to complete the reaction of any unburned pockets of fuel-air mixture and as a region to recover dissociation losses with a slight temperature decrease. For high altitude and low pressure operations, it acts as a primary zone extension, allowing more residence time to completely burn the fuel at the slower reaction rate. Finally, the dilution zone mixes the remaining air, used for wall and liner cooling, with the combustion mixture to produce an outlet flow with a suitable mean temperature and

required temperature distribution into the power turbine section of the engine. Overall combustor length must be sufficient to meet requirements in all operational modes, and tends to increase for aircraft which predominately perform high altitude cruising.

2.1.2 Inter-Turbine-Burner and Continuous-Turbine-Burner Performance Increases. Sirignano and Liu have conducted numerous thermodynamic cycle analyses of various gas-turbine engine types to evaluate the cycle efficiency improvements of utilizing an inter-turbine-burner (ITB) or a continuous-turbine-burner (CTB) to provide an additional heat source in the power turbine section (Sirignano and Liu, 1999; Liu and Sirignano, 2000). The benefits of this concept include improved specific thrust, decreased thrust specific fuel consumption, and less reliance on afterburner sections for augmenting specific thrust.

Their research compared the cycle efficiency of several turbofan and turbojet engines (standard combustor and afterburner, as equipped) with the same engine incorporating ITB or CTB over an array of conditions. They found consistent improved cycle efficiency in all areas, and further discovered the engines with an ITB or CTB had optimal operating conditions at higher compression ratios than the baseline version. Figure 3 displays a general Temperature-Entropy (T-S) diagram to illustrate the thermodynamic cycle improvement, where Q_b, Q_{tb}, and Q_{ab} are the heat addition of combustor, turbine-burner, and afterburner, respectively. Note the shorter afterburner length with CTB used. Sirignano and Liu's findings are intended to spur further research in materials development, aerodynamic, and combustion research to develop turbine burning.

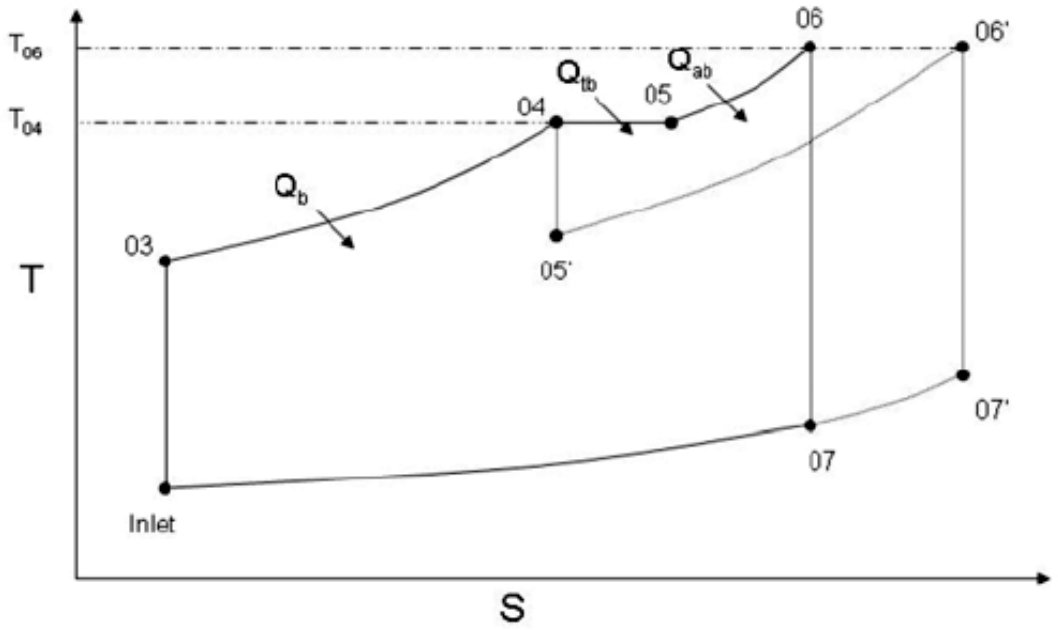

Figure 3: T-S diagram comparison of conventional combustor/afterburner engine (light dashed line) with addition of a turbine burner to engine (dark solid line), for improved cycle efficiency. Used without permission. (Sirignano and Liu, 1999:2)

2.1.3 Centrifugal Force Combustion. Lewis conducted research into centrifugal-force effects on flame-speeds in combustion to analyze the effects of swirl on combustion for improvement in conventional combustors and afterburners (Lewis, 1973). He used a rotating pipe combustor to experimentally measure observed flame-speeds under varying g-loads and equivalence ratios of propane-air and hydrogen-air mixtures. For a propane-air mixture, he found no effect under 200g's, a transition region up to 500g's, and a relation to the square root of the g-force, up to approximately 3500g's. For stoichiometric hydrogen-air mixture, no effect was found. But for a 0.6 equivalence ratio, the results were close to the propane relation. Lewis proposed a buoyant bubble

transport mechanism, wherein the density differences of hot and cold particles create a buoyant force which causes the hot particles to move faster than the turbulent flame-speeds, therein flame-speed is governed by buoyant velocity. Once the speed of the fuel-air mixture and combustion products in the tube was accounted for, he determined a flame-speed (buoyant, S_B) relation to be $S_B = 1.25\ (g)^{1/2}$.

He concluded that fire will propagate in a combustible fuel-air mixture at the fastest of the three flame-spreading mechanisms: laminar flame transport, turbulent flame transport, or buoyant bubble transport. He also found what appeared to an upper g-limit, above which combustion is extinguished, and proposed the relation $g=4500\ S_L$ (S_L, laminar flame-speed).

2.1.4 Trapped Vortex Combustion. The Trapped Vortex Combustion (TVC) is another innovative combustion concept that has been investigated by AFRL and industry partners (Hsu, Goss, and Roquemore, 1998; Roquemore et al, 2001). As shown in Figure 4, it utilizes a cavity in the wall of the main flow to create a trapped vortex, where it injects fuel and air into the cavity axially, resulting in increased fuel-air mixing and providing a stable flame area to improve combustion efficiency. Based on previous studies of non-combusting locked vortices (Little and Whipkey, 1979) in a similar type circumferential cavity, and through experimental trial-and-error, the TVC was optimized for varying flow conditions by adjusting the cavity size and cavity mass flow rate, to include a condition of a double vortex residing in the cavity. Cavity mass flow rates of 10-20% of main flow rate were found to be common.

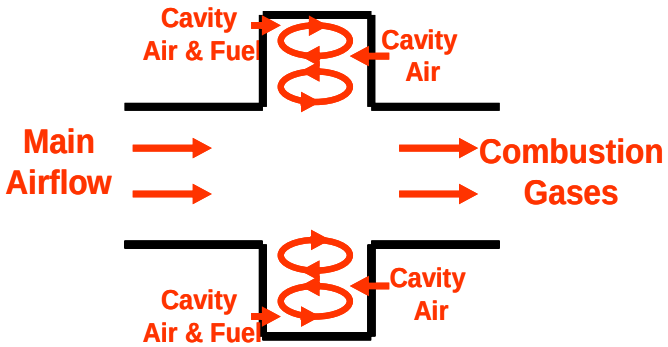

Figure 4: Trapped Vortex Combustion Concept, (Greenwood, 2005:1-2).

2.1.5 UCC Experimental Research. The UCC concept, as previously described, was conceived at the AFRL, Propulsion Directorate, based on the TVC concept, but adding the circumferential swirling flow to the cavity to burn and gain residence time in this direction, while taking advantage of a faster flame-spreading mode. It was also designed to be integral with axial stator vanes, demonstrating capability as an ITB. Initial testing on a 3-D experimental UCC rig at atmospheric pressure (Anthenien et al, 2001) demonstrated the viability of the concept, achieving over 99% combustion efficiencies, a loading of approximately 1,000g's in the cavity, 50% shorter than conventional combustor observed flame lengths, and operation over a variety of cavity equivalence ratios and combustor loadings. A general schematic of the experimental test rig is shown in Figure 5.

Experimental research is ongoing at AFRL, investigating various combustor configurations, operating conditions, and combustor loadings. Recent findings and studies include: an examination of fuel injector design, including injection angle and droplet size (Zelina et al, 2003); Laser Doppler Velocimeter (LDV) analysis of

circumferential and radial velocities in the cavity to validate centrifugal-force and buoyancy effects (Quaale et al, 2003); testing of various configurations at atmospheric and higher pressures, to include the introduction of the Radial Vane Cavity (RVC), examining operating ranges, emissions, and combustor lean blowout (Zelina, Sturgess, and Shouse, 2004); and high-pressure operating performance (Zelina, Shouse, and Neuroth, 2005). Experimental results used in this thesis where obtained directly from AFRL, Propulsion Directorate by Greenwood. They were selected to represent several varying operating conditions, to include fuel-rich burning for exhaust temperature distribution examination, and are from the 1.875-inch long cavity, 37 degrees from radial cavity air inlet configuration.

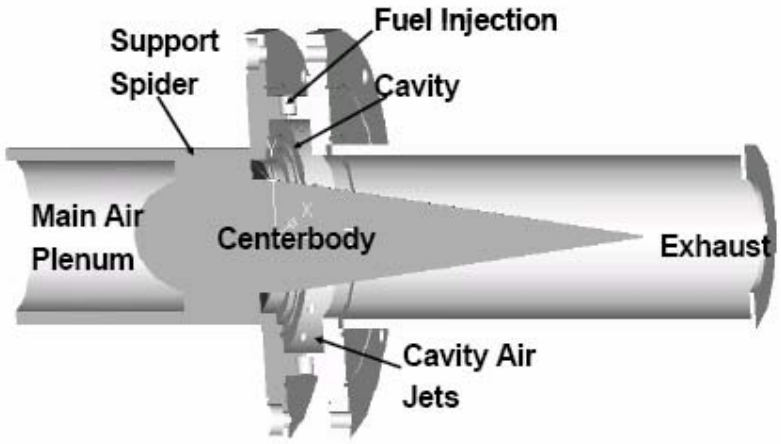

Figure 5: Original UCC experimental rig schematic, with support spider, no axial vane. Flow-path is left to right. (Zelina, Sturgess, and Shouse, 2004)

2.1.6 UCC CFD Research. A concurrent research effort utilizing CFD and numerical analysis is being conducted to guide and supplement the experimental development of the UCC. Two avenues of research are in work. The first, from The

Engineering Research and Analysis Company, utilizes *Accurate Flow Solver Computer Code* (AFSC), a two-phase model to simulate the fuel spray, evaporation, combustion, and species mechanisms. This is combined with the commercial CFD code *STAR-CD* to analyze the gas-phase flow with the combustor, and is solved on an approximately 2.5-million cell grid modeling a 60 degree sector axi-symmetric model. Varying cell sizes were used to resolve viscous boundary layers with smaller cells, and interior flow with larger cells. A first study analyzed atmospheric conditions with a lean mixture using angled fuel injection, fuel droplets of 20 μm diameter on a basic experimental configuration (Mawid et al, 2005). A second study utilizes the same operating conditions and configuration to analyze three RVC shapes (Mawid et al, 2006). These results indicated further configuration improvements are needed to optimize outflow temperature distribution away from the outer wall, among other performance measures.

A second line of CFD research has been conducted by the AFIT Department of Aeronautics and Astronautics utilizing the commercial CFD code *FLUENT*. *FLUENT* can simulate various combustion and species transport processes in conjunction with high accuracy flow solvers. Greenwood first developed the heat transfer and fuel injection models used in follow on research, in addition to performing configuration analysis to validate the CFD model with experimental results on a 60 degree sector model. He additionally evaluated the effect of decreasing the cavity axial length and separately increasing the cavity air-inlet diameter and main outflow area (Greenwood, 2005). Additional research was conducted by improving the numerical model to correct the periodic boundaries to allow fuel particles to cross (Anisko, 2006). Anisko's research

also further investigated cavity sizing, varying the RVC shape, and varying the cavity air-inlet angle. Both these studies were performed with coarse grids of approximately 300,000 to 500,000 cells utilizing wall functions, standard K-ε turbulence model, and second order, implicit, solvers for steady state solutions. This research also identified temperature distributions at the outflow plane with the maximum temperature bands near the outer radius.

2.2 Computational Fluid Dynamics

The CFD modeling used in this research is based upon and directly follows the research of Greenwood and Anisko, further refining and enhancing the modeling framework. The basis of the CFD model is use of a 3-D, double precision, segregated, implicit steady state solver, using second order upwind discretization. Improved turbulence modeling is analyzed by comparing the standard *k-ε* turbulence model from previous research the RNG *k-ε* model. Fuel injection and combustion are simulated using a discrete phase model for fuel droplet spray and evaporation into a non-premixed combustion model for reaction and species transport, to include 11 tracked species and turbulent diffusion flame modeling. Refer to Chapter 3, Section 3 for the methodology of how the models are configured.

2.2.1 CFD Software. Software used in this study includes *Solidworks 3.04* used to build the test rig structure database, *Gridgen v15* used to construct an unstructured grid within the configuration database, and *FLUENT 6.2* to solve the combusting flow and perform post-processing of results. Where applicable, specific theory discussion will center on *FLUENT* numerical methods.

2.2.2 Numerical Grid Considerations. The numerical grid is the basic block on which a numerical solution is formed, and how the grid effectively maps the solution space will have significant influence on the accuracy of the solution. Characteristics of an effective grid include a proper local density of points, with greater density providing higher accuracy in the solution at greater computational expense. Additional characteristics are smoothness of the point distribution, as larger variations can cause numerical diffusion or anti-diffusion, resulting in poor results, and the shape of the grid volumes appropriate to the local flow, as triangles and tetrahedrons should be as 'equiangular' as possible (Filipiak, 1996:6-7,23).

An unstructured grid, with tetrahedrons for 3-D meshes, is well suited to a configuration such as the UCC, as it fits well to various surfaces, is relatively easy to construct with automated software, and allows for smooth transitions among differing cell size/grid density. Grid spacing (Δs) is defined on connectors assembled over a database outline of the feature. A domain is a two-dimensional grid of a surface encompassed by connectors. A block is a three-dimensional grid encompassed by domains. The boundary decay factor is a critical element in using automated software to build domains and blocks to a user's specifications. Boundary decay controls the size proportion of cells relative from the exterior to the interior of the area or volume being built by the grid solver. In *Gridgen*, a boundary decay of '0' indicates no correlation between exterior and interior cell size, whereas a boundary decay of '1' dictates interior cells will be of identical size and dimensions as cells on the exterior of the domain or block, where any value between '0' and '1' may be used to direct the solver.

2.2.3 Turbulence Modeling. Greenwood and Anisko's preceding CFD research was conducted using the standard *k-ε* turbulence model in *FLUENT*. The standard *k-ε* model (*k*, turbulent kinetic energy and *ε*, turbulent kinetic energy rate of dissipation) was selected because it is a complete, two-equation model, provides good computing economy and solution accuracy for a wide range of turbulent flows, and includes a wall function capability. It is a semi-empirical model, and the model derivation of the *k* and *ε* equations is based on phenomenological considerations and empiricism (Fluent Inc, 2005:11-6).

Based on the research goal of providing an accurate numerical simulation of the flow for comparison with actual experimental results in the sector rigs under design, a more accurate turbulence model is desired. An improvement to the standard *k-ε* model, based on using a rigorous statistical technique known as renormalization group theory (RNG), is the RNG *k-ε* turbulence model. The RNG *k-ε* model provides higher accuracy and greater reliability for a wider class of flows. It contains an additional term in the ε equation to improve accuracy in rapidly strained flows. The effect of swirl is included to enhance accuracy. The RNG theory provides an analytical formula for turbulent Prandlt numbers, and has an option to use a differential formula for effective viscosity that accounts for low-Reynolds-number effects (Fluent Inc, 2005:11-7). The RNG *k-ε* model was evaluated in comparison with the standard *k-ε* model of previous studies and the improved results clearly merited its use as the turbulent model throughout this study.

The *FLUENT* RNG *k-ε* turbulence model derives the *k* and *ε* transport equations from the instantaneous Navier-Stokes equations, using the RNG mathematical technique.

These equations are similar to the standard *k-ε* model's form, and are shown in Equations 1 and 2 (Fluent Inc, 2005:11-17).

$$\frac{\partial}{\partial t}(\rho k)+\frac{\partial}{\partial x_i}(\rho k u_i)=\frac{\partial}{\partial x_j}\left(\alpha_k \mu_{eff}\frac{\partial k}{\partial x_j}\right)+G_k+G_b-\rho\varepsilon-Y_M+S_k \quad (1)$$

$$\frac{\partial}{\partial t}(\rho\varepsilon)+\frac{\partial}{\partial x_i}(\rho\varepsilon u_i)=\frac{\partial}{\partial x_j}\left(\alpha_\varepsilon \mu_{eff}\frac{\partial \varepsilon}{\partial x_i}\right)+C_{1\varepsilon}\frac{\varepsilon}{k}(G_k+C_{3\varepsilon}G_b)-C_{2\varepsilon}\rho\frac{\varepsilon^2}{k}-R_\varepsilon+S_\varepsilon \quad (2)$$

The analytical nature of the derivation creates a model with different constants and additional terms and functions, but several terms remain the same from the standard *k-ε* model, and are defined as follows: G_k is the generation of turbulence kinetic energy due to mean velocity gradients, G_b is the generation turbulence kinetic energy due to buoyancy, Y_M is the contribution of the fluctuating dilation in compressible turbulence to the overall dissipation rate, and S_k and S_ε are user defined source terms. Additionally, the effective viscosity is calculated in the form of the standard *k-ε* model (the option for differential formulation of viscosity for low-Reynolds number effects was not used, though it could have been) as $\mu_t=\rho C_\mu\left(k^2/\varepsilon\right)$ (Fluent Inc, 2005:11-17).

In the RNG *k-ε* model, the inverse effective Prandtl numbers, α_k and α_ε, are computed with the RNG theory derived formula of Equation 3:

$$\left|\frac{\alpha-1.3929}{\alpha_0-1.3929}\right|^{0.6321}\left|\frac{\alpha+2.3929}{\alpha_0+2.3929}\right|^{0.3679}=\frac{\mu_{mol}}{\mu_{eff}} \quad (3)$$

where α_0=1.0.

The significant difference in the RNG *k*-ε model is the additional term, R_ε, in the ε equation, as defined in Equation 4. This term improves the response and accuracy in rapidly strained flows.

$$R_\varepsilon = \frac{C_\mu \rho \eta^3 \left(1-\eta/\eta_0\right)}{1+\beta\eta^3}\frac{\varepsilon^2}{k} \tag{4}$$

where $\eta = Sk/\varepsilon$, $\eta_0 = 4.38$, and $\beta = 0.012$.

When this relation is used in the ε transport formulation, Equation 2, the third and fourth terms on the right-hand side can be combined and the ε equation rearranged as shown in Equation 5, and the effects of the R_ε can be seen (Fluent Inc, 2005:11-19,11-20).

$$\frac{\partial}{\partial t}\left(\rho\varepsilon\right) + \frac{\partial}{\partial x_i}\left(\rho\varepsilon u_i\right) = \frac{\partial}{\partial x_j}\left(\alpha_\varepsilon \mu_{eff}\frac{\partial}{\partial x_j}\right) + C_{1\varepsilon}\frac{\varepsilon}{k}\left(G_k + C_{3\varepsilon}G_b\right) - C_{2\varepsilon}^{*}\rho\frac{\varepsilon^2}{k} \tag{5}$$

where

$$C_{2\varepsilon}^{*} \equiv C_{2\varepsilon} + \frac{C_\mu \eta^3\left(1-\eta/\eta_0\right)}{1+\beta\eta^3} \tag{6}$$

The RNG derived model constants are $C_{1\varepsilon} = 1.42$, $C_{2\varepsilon} = 1.68$.

The R_ε term improves the response to rapidly strained flows by adjusting its contribution to the ε transport equation based on the magnitude of the strain rate. In areas where $\eta < \eta_0$, corresponding to weak to moderate strain, the R_ε term makes a positive contribution, with $C_{2\varepsilon}^{*}$ becoming larger than $C_{2\varepsilon}$. This gives results comparable to the

standard *k*-*ε* model. In areas of large strain, $\eta > \eta_0$, the R_ε term makes a negative contribution, and $C_{2\varepsilon}^*$ becomes smaller than $C_{2\varepsilon}$. This results in a smaller decrease in ε, retaining more ε to reduce the calculated value of *k*, and leads to a reduction in effective viscosity. Thus, in rapidly strained flows, this model is more responsive to the effects of rapid flow strain, and returns a lower turbulent viscosity than the standard *k*-*ε* model (Fluent Inc, 2005:11-19).

2.2.4 Wall Functions. An accurate solution for a wall-bounded, fully turbulent flow relies on a proper treatment and accurate reproduction of the near-wall flow. The near wall region is an area where solution variables can have large gradients, especially relating to velocity and temperature gradients in the momentum and thermal boundary layers, leading to the production of turbulent kinetic energy and vorticity into the core flow. Man-hours to implement and computational resource limitations make cause for simplification by use of wall-functions to connect the fully turbulent core and outer layers with the wall by use of specified relations, and are justified in this case as a matter of economy as an accurate solution of the near wall flow is not required. *FLUENT* provides two options for wall functions for use with the *k*-*ε* models, a standard wall function and a non-equilibrium wall function to sensitize to pressure gradients and apply a two-layer approach in computing turbulence kinetic energy in wall-neighboring cells.

FLUENT's standard wall function treatment uses a set of semi-empirical formulas and functions to link the solution variables at the near-wall cells with the wall quantities, to include laws-of-the-wall for mean velocity, temperature, and other scalars, in addition to computing near-wall turbulence values, such that a numerical grid with cell size and

spacing at the walls sufficient to resolve only into the intermediate or log-law region of the boundary layer is required. The logarithmic law for mean velocity is known to be valid for a wall unit (y^*) range of 30 to 300, where y^* is defined in Equation 7 (Fluent Inc, 2005:11-54).

$$y^* \equiv \frac{\rho C_\mu^{1/4} k_P^{1/4} y_P}{\mu} \tag{7}$$

In *FLUENT*, the logarithmic law is employed when $y^* > 11.225$. If the wall neighboring cell is such that $y^* < 11.225$, then a laminar stress-strain relationship is applied. In *FLUENT*, laws-of-the-wall for mean velocity and temperature are based on wall unit, y^*, not y^+, and it is recommended the wall-adjacent cells' center lie within the range of valid y^* (Fluent Inc, 2005:11-54).

The further refined non-equilibrium wall function treatment uses an enhanced mean velocity formulation to adjust a cells mean velocity based on pressure gradients related with its physical position in relation to the viscous sub-layer, as shown in Equations 8, 9, and 10 (Fluent Inc, 2005:11-58).

$$\frac{\tilde{U} C_\mu^{1/4} k^{1/2}}{\tau_w / \rho} = \frac{1}{\kappa} \ln\left(E \frac{\rho C_\mu^{1/4} k^{1/2} y}{\mu} \right) \tag{8}$$

where

$$\tilde{U} = U - \frac{1}{2} \frac{dp}{dx} \left[\frac{y_\upsilon}{\rho \kappa \sqrt{k}} \ln\left(\frac{y}{y_\upsilon} \right) + \frac{y - y_\upsilon}{\rho \kappa \sqrt{k}} + \frac{y_\upsilon^2}{\mu} \right] \tag{9}$$

and the physical viscous sub-layer thickness is computed with $y_\upsilon^* = 11.225$ in Equation 10.

$$y_\upsilon \equiv \frac{\mu y_\upsilon^*}{\rho C_\mu^{1/4} k_P^{1/2}} \tag{10}$$

Furthermore, the non-equilibrium wall function approach uses a two-layer based concept to compute the budget for turbulence kinetic energy at wall-neighboring cells to enable solving the *k* equation in these cells. This assumes they consist of the viscous sub-layer and fully turbulent layer, using the profile assumptions of Equation 11, and Equations 12 and 13 for cell-averaged *k* production ($\bar{G}_k$) and dissipation rate ($\bar{\varepsilon}$) (Fluent Inc, 2005:11-58)

$$\tau_t = \begin{cases} 0, & y < y_\upsilon \\ \tau_w, & y > y_\upsilon \end{cases} k = \begin{cases} \left(\frac{y}{y_\upsilon}\right)^2 k_P, & y < y_\upsilon \\ k_P, & y > y_\upsilon \end{cases} \varepsilon = \begin{cases} \frac{2\nu k}{y^2}, & y < y_\upsilon \\ \frac{k^{3/2}}{C_l y}, & y > y_\upsilon \end{cases} \tag{11}$$

$$\bar{G}_k \equiv \frac{1}{y_n}\int_0^{y_n} \tau_t \frac{\partial U}{\partial y} dy = \frac{1}{\kappa y_n} \frac{\tau_w^2}{\rho C_\mu^{1/4} k_P^{1/2}} \ln\left(\frac{y_n}{y_\upsilon}\right) \tag{12}$$

$$\bar{\varepsilon} \equiv \frac{1}{y_n}\int_0^{y_n} \varepsilon dy = \frac{1}{y_n}\left[\frac{2\nu}{y_\upsilon} + \frac{k_P^{1/2}}{C_l} \ln\left(\frac{y_n}{y_\upsilon}\right)\right] k_P \tag{13}$$

where y_n is the height of the cell (y_n=2y_P), used for quadrilateral and hexahedral shaped cells to compute a volume average approximated by depth average. In the case of tetrahedral grids, the appropriate volume average is used.

2.2.5 Non-premixed Combustion and Species Modeling. Non-premixed describes a combustion process where the fuel and oxidant enter the reaction space from separate sources, and are mixed within while reacting. *FLUENT* has a useful variety of combustion models to cover many uses. The non-premixed combustion model using chemical equilibrium for simulation of turbulent diffusion flames, combined with a discrete phase model for liquid fuel injection and evaporation, is well suited to the UCC combustion problem. This model includes intermediate (radical) species prediction, dissociation effects, and rigorous turbulence-chemistry coupling, in addition to being computationally efficient (Fluent Inc, 2005:15-2). The chemical equilibrium approach is able to be used in this research based on the premise of chemical time being much shorter than the mixing time and residence time over which system conditions change (Heywood, 1988:92). Chemical time can be calculated to be on the order of 50-100 μs for the modeled reactions, where residence time for cavity injected mass is on the order of 2-10 ms.

The non-premixed combustion model is a specific species transport model, based on an approach using simplifying assumptions to relate the instantaneous thermochemical state to the conserved scalar quantity mixture fraction, as defined in Equation 14 in terms of atomic mass fraction. The Favre mean (density-averaged) mixture fraction ($\overline{f}$) and mixture fraction variance ($\overline{f}^{'2}$) transport equations, Equations 15 and 16, are solved for the reacting fluid with the assumption of equal diffusivities for turbulent flow (turbulent convection much greater than molecular diffusion)(Fluent Inc, 2005:15-3,15-5).

$$f = \frac{Z_i - Z_{i,\,ox}}{Z_{i,\,fuel} - Z_{i,\,ox}} \tag{14}$$

$$\frac{\partial}{\partial t}\left(\rho \overline{f}\right) + \nabla \cdot \left(\rho \vec{\upsilon} \overline{f}\right) = \nabla \cdot \left(\frac{\mu_\tau}{\sigma_t} \nabla \overline{f}\right) + S_m + S_{user} \tag{15}$$

$$\frac{\partial}{\partial t}\left(\rho \overline{f}^{'2}\right) + \nabla \cdot \left(\rho \vec{\upsilon} \overline{f}^{'2}\right) = \nabla \cdot \left(\frac{\mu_t}{\sigma_t} \nabla \overline{f}^{'2}\right) + C_g \mu_t \left(\nabla \overline{f}\right)^2 - C_d \rho \frac{\varepsilon}{k} \overline{f}^{'2} + S_{user} \tag{16}$$

where S_m is a source term of mass transfer into gaseous phase from liquid fuel droplets, S_{user} is user defined source term, $f' = f - \overline{f}$, and constants $\sigma_t = 0.85$, $C_g = 2.86$, $C_d = 2.0$.

However, *f*, must also be determined by overall equivalence ratio, as shown in Equations 17 and 18, to accommodate changes in fuel/air ratio (*r* is the air-to-fuel ratio mass basis). Extending to a non-adiabatic system to model heat gain/loss with walls and fuel droplets, and using the chemical equilibrium assumption where all thermochemical scalars are related to mixture fraction, instantaneous species mass fraction, density, or temperature can be calculated as represented in Equation (18), where *H* is the instantaneous enthalpy (Fluent Inc, 2005:15-6, 15-7).

$$\phi = \frac{(fuel/air)_{actual}}{(fuel/air)_{stoichiometric}} \tag{17}$$

$$f = \frac{\phi}{\phi + r} \tag{18}$$

$$\phi_i = \phi_i\left(f, H\right) \tag{19}$$

These instantaneous scalars must now be related to their associated averaged values, for application to the equations governing the turbulent reacting flow, via the turbulence-chemistry interaction model. *FLUENT* uses an assumed-shape probability density function (PDF) approach for this and its closure model for non-premixed combustion, such that the mean species fraction, temperature, and density are functions of $\overline{f}$, $\overline{f}^{'2}$, and $\overline{H}$. The computational efficiency is achieved by pre-calculating 3-D look-up tables for the specified scalars, storing them to be retrieved and used in lieu of performing the calculations for each species, each cell, during the solving process.

Each joint PDF, $p(f, H)$ presents predicted values for temporal fluctuations of *f* in the turbulent flow. In the non-adiabatic model, simplification is achieved by assuming enthalpy fluctuations are independent of enthalpy level, defining the joint PDF as shown in Equation 20.

$$p(f, H) = p(f)\delta(\mathrm{H} - \overline{\mathrm{H}}) \tag{20}$$

The β-function PDF shape is calculated as a function of $\overline{f}$ and $\overline{f}^{'2}$ for each scalar. The look-up tables are set up such that contoured layers are stacked vertically, with the vertical scale representing the enthalpy value (magnitude of heat gain or loss). For a specific enthalpy value, the designated horizontal layer 3-D shape will deliver a value for the specified mean species or temperature scalar, as calculated by Equation 21, where the mean enthalpy transport equation is defined as Equation 22 (S_h is source term for heat transfer with walls or dispersed phase) or mean density by Equation 23 (Fluent Inc, 2005:15-8 – 15-19).

$$\overline{\phi}_i = \int_0^1 \phi_i\left(f, \bar{H}\right) p\left(f\right) df \tag{21}$$

$$\frac{\partial}{\partial t}\left(\rho \bar{H}\right) + \nabla \cdot \left(\rho \vec{v} \bar{H}\right) = \nabla \cdot \left(\frac{k_t}{c_p} \nabla \bar{H}\right) + S_h \tag{22}$$

$$\frac{1}{\overline{\rho}} = \int_0^1 \frac{p(f)}{\rho(f)} df \tag{23}$$

Since all PDF's are pre-calculated, desired species to be included/excluded are designated, together with boundary mass or mole fraction values for fuel and oxidizer, at problem set-up, and the PDF tables are calculated based on a defined operating pressure for the entire problem. Additionally, a rich flammability limit option is available to suspend the equilibrium chemistry calculation in areas/cells where the specified value is exceeded, the composition is then computed based on mixing, not burning, at the rich limit (Fluent Inc, 2005:15-39).

The *FLUENT* discrete phase model (DPM) used for liquid fuel spray injection tracks spherical droplets using stochastic tracking methods and modeling of heat transfer for droplet heating/cooling, vaporization, and boiling. The discrete phase is coupled with the continuous phase solution, such that each phase impacts the other, but is computed separately. For the steady state solution procedures, frequency of DPM updates per continuous phase iterations is user defined. The steady state solution procedure is to first solve the continuous phase flow field, then add the DPM model and solve the coupled flow.

Particle trajectories are predicted by integrating the force balance on the particle, in a Lagrangian reference frame, to include particle inertia and effects of forces acting on

the particle, as shown in Equation 24 for the Cartesian coordinate x-direction (Fluent Inc, 2005:23-5).

$$\frac{du_p}{dt} = F_D\left(u - u_p\right) + \frac{g_x\left(\rho_p - \rho\right)}{\rho_p} + F_x \tag{24}$$

where F_x is an additional acceleration term, $F_D\left(u - u_p\right)$ is the drag force per unit particle mass and

$$F_D = \frac{18\mu}{\rho_p d_p^2}\frac{C_D \mathrm{Re}}{24} \tag{25}$$

$$\mathrm{Re} \equiv \frac{\rho d_p \left|u_p - u\right|}{\mu} \tag{26}$$

The stochastic tracking approach, using the Discrete Random Walk model, predicts the turbulent dispersion of the particles by integrating the trajectory equations for each particle, using instantaneous fluid velocity, $\bar{u} + u'(t)$, where the fluctuating component is a function of time, and a "number of tries" specifies a number of representative particle tracks to average over, such that the random value of fluctuations is kept constant over an interval of time given by the characteristic lifetime of flow eddies to account for the random effects of turbulence on the particle (Fluent Inc, 2005:23-12).

2.2.6 NO_X Modeling. As a method to increase computing efficiency and improve NO_X prediction accuracy, *FLUENT* intentionally excludes these calculations from the species transport model, but calculates the NO_X transport equations separately and does not compute actual quantities until post-processing, basing them on the

combustion solution. Thermal and prompt NO modeling will be used in estimating NO_X emissions, with fuel NO and N_2O intermediate considered not significant, thus only the single NO transport equation is required. Thermal NO is the resultant in the post-flame gases of the oxidation of atmospheric nitrogen, is highly temperature dependent, and is the primary contributor to NO_X emissions. Prompt NO originates in high-speed reactions at the flame front, is prevalent in rich flames, and is dependent on hydrocarbon byproducts and overall equivalence ratio (Lefebrve, 1983:469; Fluent Inc, 2005:20-2 – 20-11).

Thermal NO formation is governed by the extended Zeldovich mechanism of highly temperature-dependent chemical reactions, the principal of which are displayed as Equations 27 and 28, with a third reaction mechanism known to contribute particularly at near stoichiometric and fuel-rich mixtures in Equation 29.

$$O + N_2 \rightleftharpoons N + NO \tag{27}$$

$$N + O_2 \rightleftharpoons O + NO \tag{28}$$

$$N + OH \rightleftharpoons H + NO \tag{29}$$

The thermal NO formation rate becomes dependent on the reaction rates of these chemical reactions and the concentration of O, H and OH radicals and the stable species (O_2, N_2). Using known reaction rate constants from established experimental data, determining the O radical concentration by decoupling from the combustion reaction mechanism and assuming equilibrium of the combustion reactions, the overall thermal NO rate and mass fraction are determined. OH radical formation and the third Zeldovich

reaction mechanism can be excluded for lean fuel conditions in most cases (Fluent Inc, 2005:20-4 – 20-6).

Prompt NO formation involves a complex set of reaction mechanisms with many intermediate combusting species. However, the primary reaction sets involve CH and CH_2 reactions with N_2 to initiate a series to produce NO. As such, the rate of prompt NO formation can be modeled, adjusted with experimental data, based on the reaction rate of the initial reactions controlling the series, where Equation 30, for CH is the primary reaction in determining prompt NO formation (Fluent Inc, 2005:20-9).

$$CH + N_2 \rightleftharpoons HCN + N \tag{30}$$

2.2.7 FLUENT Post-processing. The use of averaged values at specified planes of the combustor to quantify performance, such as the exhaust outlet plane or an arbitrary plane to analyze cavity flow parameters, is critical in the design and evaluation process. Two methods are used by *FLUENT* to perform these surface integrations, mass-weighted and area-weighted averaging. Mass-weighted averaging divides the sum of the product of the field variable chosen and the absolute value of the dot product of the facet area and momentum vectors by the sum of the absolute value of the dot product of the facet area and momentum vectors, as shown in Equation 31. Mass-weighted averages are used for all surface integral post-processing calculations. Mass flow rates are computed by summing the product of density with the dot product of the facet area vector and the facet velocity vector, as shown in Equation 32 (Fluent Inc, 2005:30-11, 30-12).

$$\frac{\int \phi\rho\left|\vec{\upsilon}\cdot d\vec{A}\right|}{\int \rho\left|\vec{\upsilon}\cdot d\vec{A}\right|} = \frac{\sum_{i=1}^{n}\phi_i\rho_i\left|\vec{\upsilon}_i\cdot\vec{A}_i\right|}{\sum_{i=1}^{n}\rho_i\left|\vec{\upsilon}_i\cdot\vec{A}_i\right|} \tag{31}$$

$$\int \rho\vec{\upsilon}\cdot d\vec{A} = \sum_{i=1}^{n}\rho_i\vec{\upsilon}_i\cdot\vec{A}_i \tag{32}$$

2.3 Heat Transfer

Accurate modeling of the heat transfer characteristics of the UCC is important in obtaining an accurate CFD solution, due to the unique nature of the combustion cavity residing on the outer surface of the engine where it is in contact with ambient air, and the large internal surface area, with walls also adjacent to ambient air. The UCC will be modeled as a stainless steel body, following its experimental test rig construction, using convective and radiation processes for modeling. Axial vanes and the internal center-body will be modeled as adiabatic due to full model symmetry. The outer walls of the main flow and front/rear walls of the cavity will be modeled as mixed convective and radiation due to external exposure to ambient conditions. Finally the outer circumference of the cavity, adjoining the cavity air plenum, will be modeled as convective only.

For the wall boundary conditions in *FLUENT*, the radiation emissivity and convective heat transfer coefficient, $\bar{h}$, for each surface requires calculation. The emissivity value of 0.85, estimated from emissivity reference data for AISI 347, stably oxidized stainless steel (Incropera and Dewitt, 2002:929) is taken for all walls modeled as radiating. To determine $\bar{h}$ for the various walls, the UCC can be modeled as a long cylinder in free convection, as discussed in *Fundamentals of Heat and Mass Transfer*

(Incropera and Dewitt, 2002:554-555). Equation 33 is used to solve for $\bar{h}$ as a function of Nusselt number (Nu_D), the dimensionless temperature gradient at surface, valid over a wide Rayleigh number (Ra_D) range, which relates the relative magnitude of buoyancy and viscous forces in the fluid, defined in Equation 34,

$$\overline{Nu_D} = \frac{\bar{h}D}{k} = \left\{ 0.60 + \frac{0.387 Ra_D^{1/6}}{\left[1 + \left(0.559/\mathrm{Pr}\right)^{9/16}\right]^{8/27}} \right\}^2 \tag{33}$$

$$Ra_D = \frac{g\beta\left(T_S - T_\infty\right)D^3}{\nu\alpha} \tag{34}$$

where k is the conductive heat transfer coefficient, Pr is the Prandtl number and is taken as Pr=0.7 for ambient air, g is the acceleration due to gravity, ν is the kinematic velocity, β is volumetric thermal expansion coefficient, α is thermal diffusivity, and T_s and T_∞ are surface and free-stream temperature.

2.4 Combustor Performance Criteria

2.4.1 Combustor Loading Parameter. A variation of the Longwell Loading Parameter, referred to as Combustor Loading Parameter (CLP), is used to quantify and enable comparison of different combustor operating conditions, as defined in Equation 35, where the UCC cavity is considered the combustor, $\dot{m}_{cav}$ is cavity air and fuel mass flow rate in lb_m/sec, V is cavity volume in ft^3, P is absolute pressure in atmospheres, and T_3 is absolute temperature in K.

$$CLP = \frac{\dot{m}_{cav}}{V \cdot P^{1.75} \cdot e^{T3/300}} \tag{35}$$

2.4.2 Pressure Loss. Dimensionless pressure-loss is an important factor in evaluating combustor performance and is a measure of the flow efficiency, as managing pressure losses is not only a combustor performance requirement, but also a critical design factor for the entire engine. Overall pressure loss is calculated by Equation 36 and is presented as a percentage. It primarily measures the 'cold' pressure losses related to turbulence and friction of the fluid flow through the combustor. 'Hot' losses, those related to the pressure drop due to combustion are also roughly included (Lefebvre, 1983:108).

$$\frac{dP}{P} = 100 * \frac{P_3 - P_4}{P_3} \tag{36}$$

where P_3 is inlet absolute pressure and P_4 is outlet absolute pressure.

2.4.3 Emissions. Pollutant species of interest at the combustor exhaust plane include CO, CO_2, NO_x, and unburned hydrocarbons (UHC), while the exhaust level of O_2 is of interest in evaluating combustion efficiency. These emissions are generally measured on a particulate level, or by species mole fraction, and are reported in the form of part-per-million (ppm) for CO, NO_x, UHC or percentage of total for CO_2, O_2.

The combustion modeling in *FLUENT*, as already described, uses two separate computational processes to model the liquid and gaseous fuel phases, and thus separate post-processing of these phases is required at the combustor outlet. The gaseous phase component of the exhaust UHC is evaluated as the other gaseous species, resulting in a

simple mole fraction. Only $C_{12}H_{23}$ is measured, as the only significant UHC remaining as a result of the equilibrium reaction model. The liquid fuel contained in the DPM also requires measurement, and its quantification requires minor computation, as *FLUENT* only provides a DPM concentration measure to quantify the liquid fuel content. The mole fraction of the liquid phase can be calculated by the ratio of the fluid concentration (ρ_{HC}) over the hydrocarbon's molecular mass (MM_{HC}) to the sum of this figure added with the average exhaust density (ρ_{exh}) over the average exhaust molecular mass (MM_{exh}). This mole fraction of the liquid fuel level is combined with that of the gaseous phase to provide the total level of UHC's, as shown in Equation 37 (Greenwood, 2005:3-4).

$$ppm_{UHC} = ppm_{vapor} + \frac{\frac{\rho_{HC}}{MM_{HC}}}{\frac{\rho_{HC}}{MM_{HC}} + \frac{\rho_{exh}}{MM_{exh}}} \tag{37}$$

2.4.4 Combustion Efficiency. The efficiency of a combustor is a measure of the amount of energy released from the actual combustion in relation to the total amount of energy released in a perfect, complete reaction, and is a primary indicator of performance. Experimentally it is difficult to directly measure the total energy, so a measure of incomplete reaction components, CO and UHC's, are used to calculate the efficiency decrease by use of an industry standard formulation (*Society of Automotive Engineers*, 1996). Equation 38 is the measure of combustor efficiency (η_b), where the Emissions Index (EI) is defined in Equation 39 for use with CO and UHC emission's quantities and H_C is approximately 43,500 kJ/kg for kerosene fuel.

$$\eta_b = 100\left[1.00 - 10100\frac{EI_{CO}}{H_C} - \frac{EI_{C_{12}H_{23}}}{1000}\right] \tag{38}$$

$$EI = \frac{g_{poll}}{kg_{fuel}} \tag{39}$$

2.4.5 Outlet Temperature Distribution. The temperature distribution at the outlet of a combustor leading into an engine's turbine is critical in enabling efficient energy extraction by power turbines and for turbine material, durability, and lifetime factors. Quantitative measures to evaluate the distribution of the combustor outlet/turbine inlet temperature (T_4) to the mass-weighted mean T_4 are pattern and profile factors (Lefebrve, 1983:142).

The pattern profile factor relates the maximum spot temperature to the mean temperature at the combustor exit as defined by

$$\text{Pattern Factor} = \frac{T_{\max} - T_4}{T_4 - T_3} \tag{40}$$

where T_{max} is the maximum recorded temperature, T_3 is the mean inlet temperature, and T_4 is the mean outlet temperature. Pattern factor is important in material considerations for turbine stator/guide vanes.

The profile factor relates the maximum average radial temperature to the mean temperature at the combustor exit as defined by

$$\text{Profile Factor} = \frac{T_{mr} - T_4}{T_4 - T_3} \tag{41}$$

where T_{mr} is the maximum circumferential mean temperature obtained from averages of temperature by radial height. Profile factor is important in material considerations for the rotating turbine blades.

A uniform temperature distribution at the combustor exit is considered ideal, with the pattern and profile factors equal to zero. Therefore, design optimization involves reducing the maximum temperatures found on the outlet. Further qualification of the outlet temperature distribution can be conducted with use of CFD flow visualization and data plots.

2.4.6 Cavity G-loading. Centrifugal-force effects are a primary design characteristic of the UCC, so evaluating the g-loadings produced in the cavity is a performance criterion for use in analyzing performance and comparing configurations and operating conditions. The g-loadings can be calculated from known circumferential velocity (U_θ) at a given radius (R) by Equation 42, where g_o is the gravitational constant.

$$g = \frac{U_\theta^2}{g_o R} \tag{42}$$

2.5 Design Considerations for an Experimental Combustor Sector Rig

2.5.1 UCC Flow Area of Interest. As ongoing research results are indicating further optimization of the combustor's outflow temperature distribution is needed, a better understanding of the flow dynamics creating the outflow profile is desired. This requires a full understanding of the turbulent flow patterns and combustion effects in the area of interaction between the circumferential cavity flow and the axial main flow, to specifically include the RVC effects. As previously stated, on a full 360 degree UCC test

rig, it is not possible to use LDV to measure the flow characteristics in this area. Therefore, the down-flow side of the axial vane, with the RVC, and its wake region in the main flow channel become the area of interest for study. This can be studied with a 2-D sector rig to recreate the flow, such that LDV techniques may be used to analyze the combusting flow in an experimental model. The circumferential flow conditions over the top of the axial vane in the cavity need to be reproduced, in addition to replicating the main flow approaching the area along the axial vane.

2.5.2 Recreating 360 degree UCC Cavity Flow Characteristics. Several factors need to be accounted for in reproducing a re-circulating, combusting flow involving the UCC's configuration. Examination of existing UCC CFD solutions reveals the cavity entrains two to three times the cavity inlet mass flow rate, arriving at a state of mass/density flux equilibrium. This entrainment is a result of both main flow entrainment and cavity injected mass retention. Therefore the first factor in recreating the 3-D cavity flow is providing extra mass flow through the cavity over the vane area.

An additional factor, complementary to the mass entrainment, is a result of the placement of the fuel injection directly over the axial vane. Clearly, a model with only one fuel injection point directly over the RVC to be examined will not suffice to produce the desired combusting flow. Therefore, in order to produce a cavity flow reproducing some of the re-circulating mass entrainment and combustion process, the cavity portion of the sector rig should be the equivalent of at least two 60 degree segments of the full configuration (including an additional fuel injection point), with this cavity length occurring prior to the intersection with the main flow channel and RVC. A further issue

to consider is local φ_{cav} at the first fuel injection point to provide for proper combustion at the start of the non-re-circulating cavity. This issue can be resolved with the addition of an extra pair of cavity air inlets in the circumferential direction at the start of the cavity, with the result being a proper φ_{cav} at the first fuel injection point and increased mass flow to account for cavity re-circulating flow. The non-recirculating cavity now consists of 10 cavity air inlets and two fuel injection points. Figure 6 illustrates these design concepts on a schematic of the 2-D curved cavity sector rig.

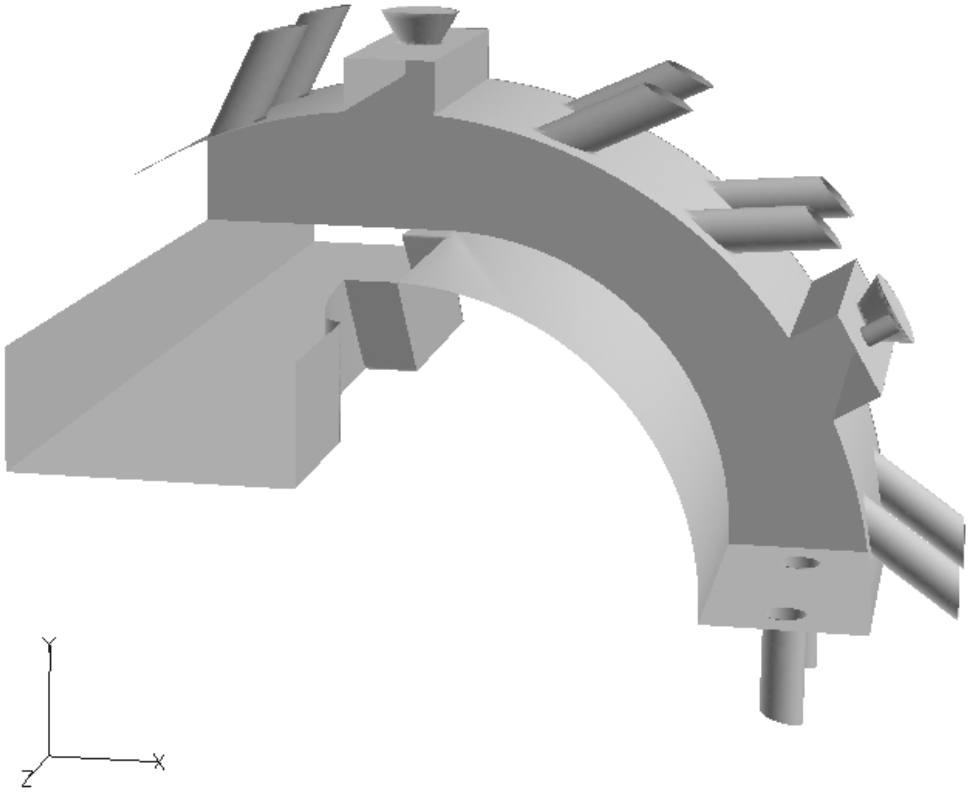

Figure 6: Curved sector rig schematic illustrating concept of extended cavity length to reproduce re-circulating cavity mass flow and combustion processes.

2.5.3 Laser Diagnostic Considerations. A flat clear quartz wall is desired to allow the laser to view the flow at the RVC. On the 3-D axi-symmetric 60 degree sector model, the periodic side walls are not parallel with the axial vane, creating an undesirable alignment. Creating the main flow channel to have a flat crystal quartz wall parallel to a single axial vane would create the best alignment to optimize the performance of the laser diagnostics. An additional flat quartz wall on the bottom of the main flow channel would also allow for side scatter LDV measurements, in addition to the back scatter method provided with only a single wall. The clear conclusion from these factors is a need to square the main flow area, or eliminate the 3-D axi-symmetric periodicity.

In addition to squaring the main flow area and providing a flat quartz wall on one side, the design can be simplified by imbedding the axial vane in the non-viewing wall and essentially shifting the 60-degree section by 30-degrees to cause the 4 sided cavity flow to first intersect the main flow directly over the axial vane imbedded in the wall. The now rectangular main flow area can easily be dimensioned to replicate the cross-sectional area of the 3-D model, while maintaining the same axial vane height, and this is again illustrated in Figure 6.

III. Methodology

3.1 Design and Evaluation Process Outline

With the overall goal of this research being the design of 2-D sector rigs to accurately reproduce the flow conditions in a full experimental model, the design and evaluation process chosen is one which uses deliberate steps in the configuration design process, validating the results of the previous step. Specifically, the CFD models are to be first validated on the experimental data's configuration, the 1.875-inch (47.6 mm) long cavity with 37 degree cavity air inlets, using the 60 degree 3-D axi-symmetric, periodic CFD test model, as previous CFD studies have used.

Next, this CFD model is applied to the desired UCC configuration. For this research the baseline configuration is the 1.5-inch (38.1 mm) short cavity with 45 degree cavity air inlets, on the 60 degree 3-D axi-symmetric, periodic CFD model. Results are compared with the experimental configuration CFD results, thus forming the baseline model. Additionally, all atmospheric test condition simulations will be solved on this baseline 3-D model for comparison and validation of the sector rig configurations.

The next step was the implementation of the 2-D effect by creating a flat, planar cavity model, with cavity periodic boundaries to model re-circulating cavity flow, interacting across a rectangular main flow channel, with the axial RVC vane imbedded in the side walls. Again, the results are compared against experimental and 3-D CFD model results. The intent of this design step is to determine the suitability of the main flow channel shape and form, in addition to evaluating how the cavity flow will perform in a

4-sided channel. This configuration also provides the scientific insight into the behavior when the centrifugal-force effects on combustion are removed from the process.

The final step is the design and evaluation of the flat cavity and curved cavity sector rigs. These configurations are evaluated at an experimentally validated operating condition, to provide for a straight-forward performance comparison with the baseline 3-D CFD model, then also evaluated at several atmospheric pressure test conditions, compared again with the same conditions on the 3-D baseline model. This provides a CFD data set for comparison when the sector rigs are tested experimentally.

3.2 Models and CFD Grid Development

3.2.1 Configuration Model Design. Each UCC physical configuration model for this research is initially designed and built using *Solidworks* software. The benefits of designing in *Solidworks* include the ease of 3-D visualization, the ease of setting consistent dimensions, and the building block approach, providing for simplicity of trial-and-error model design, the ability to use components in multiple models, and simple conversion from a model constructed with CFD grid generation factors considered into a physical model suitable for experimental testing (i.e. adding air plenum chambers, pressure and temperature ports, etc.).

The 3-D axi-symmetric 1.875-inch cavity experimental and 1.5 -inch cavity baseline models were designed as shown in Figure 7, with the experimental model *Gridgen* basic structure database from Anisko used, and the 1.5-in cavity baseline model built in *Solidworks* to incorporate the desired cavity and air inlet angles. The 1.5-inch

cavity and 45 degree inlet selection as the baseline for this research is based on previous CFD analysis as a potential optimum design parameter, as well as the existence of on-going experimental research at AFRL Propulsion Directorate on this configuration. An important consideration in building the axi-symmetric models is maintaining all parts with the common centerline and consistent radial and angular dimensions, to enable the creation of an accurate rotational periodic boundary in the grid.

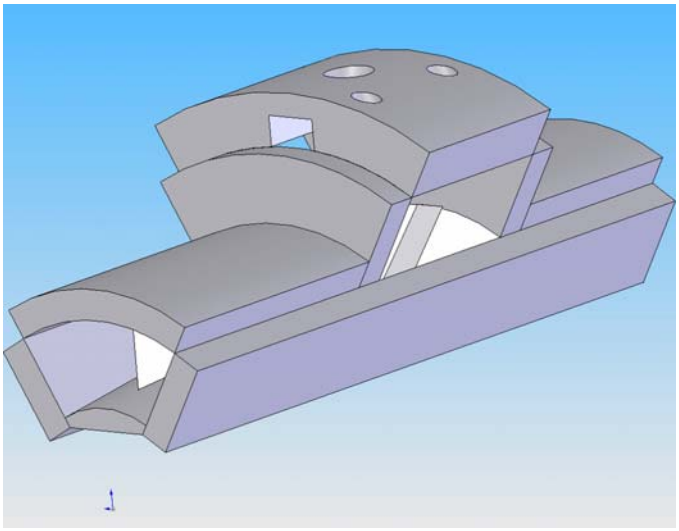

Figure 7: UCC 1.5-inch short cavity baseline model in *Solidworks*.

Dimensions of the 3-D models include: main flow inner radius of 0.975 in (23.8 mm), axial vane height of 0.5375 in (13.65 mm), cavity inner radius of 1.5125 in (38.4 mm), cavity height of 0.8025 in (20.4 mm), cavity outer radius of 2.315 in (58.8 mm), and cavity air inlet radius of 0.105 in (2.7 mm). A cavity in a cavity (CIAC) is placed axially in the cavity outer wall, with dimensions of 0.25 in (6.4 mm) by 0.43 in (10.9 mm), at the fuel injection point to enhance mixing and stability of the flame at the

injection point. Centered axially in the CIAC is a fuel injection cone extending outward further into the cavity wall, with an initial radius of 0.08 in (2.0 mm). Fuel injection will occur at the top of the CIAC in the center of the injection cone base. Finally, a slight inward expansion of the main flow approaching the exit, to simulate the decreasing radius curvature of the cone shaped center-body of the experimental model, is accomplished with a small angle slope on the inner circumference beginning just prior to the trailing edge of the axial vane and terminating with an inner radius reduced to 0.82 in (20.8 mm).

The 2-D flat cavity periodic model was next designed as an intermediate step to test and evaluate several configuration implementations, to include the main flow channel rectangular shaping, imbedding the axial vane with the side walls, flow through a four sided cavity, and the aforementioned removal of the centrifugal-force effects. Figure 8 displays the general layout of the 2-D flat, periodic model.

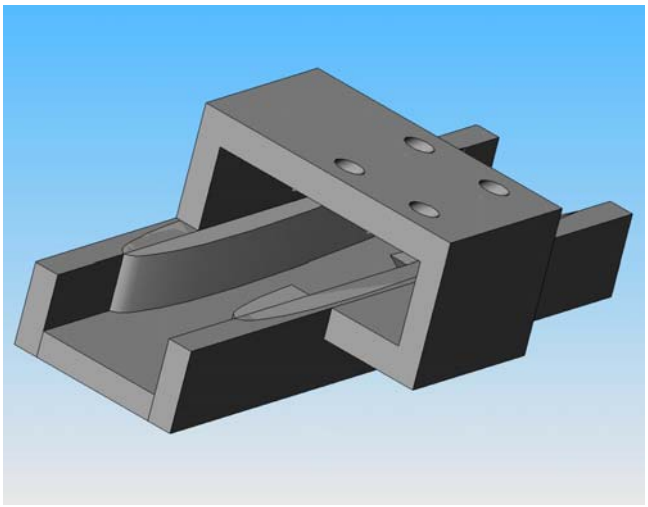

Figure 8: Basic design of 2-D 1.5-inch flat cavity, periodic UCC model with inlet, outlet, and cavity walls excluded.

A suitable width for the main channel was determined to be 1.25 in (31.75 mm), combined with maintaining the axial vane height at 0.5375 in, to closely approximate the inlet area of the 3-D models. An area expansion for the exhaust end is not utilized in this model. In reproducing the cavity, the height of the cavity was retained at the cavity radius of 0.8 in, and the length of the cavity was set at 2.25 in (57.2 mm) to reasonably approximate the cavity volume of the 3-D model, but also allow some distance to accommodate longer flame lengths. The cavity air inlet pairs were spaced around the fuel injection point, directly over the axial vane with the RVC, with enough space to allow another fuel and air inlet set be placed with equal spacing over the following vane. Due to the flattening of the cavity outer radius, the air inlets become closer together in this configuration. A CIAC was not included in this early, intermediate model.

The flat and curved cavity 2-D sector rigs were designed based on the evaluation of the 2-D flat periodic model and a series of several test and evaluation cycles. These models are depicted in Figures 9 and 10 as their *Solidworks* rendering appropriate for CFD grid generation. The resultant configuration designs include the same rectangular main flow channel, except without an imbedded axial vane in the far wall, where the quartz crystal wall will be, or the exhaust area expansion. This leaves only the axial vane half, with the RVC, at the main flow and cavity flow intersection line and keeps the main flow cross sectional area and overall volume roughly consistent with the 3-D models.

The cavity for both the flat and curved cavity is designed to deliver the mass flow rate and approximate velocity magnitude across the axial cavity plane over the vane RCV as found in the 2-D or 3-D baseline models, respectively, by doubling the cavity to a one-

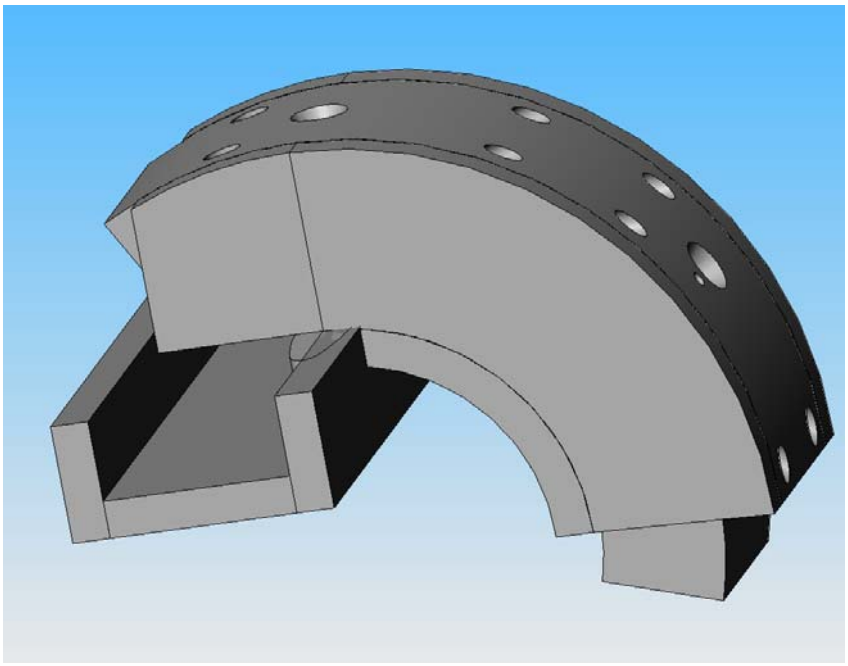

Figure 9: General design of UCC curved cavity sector rig, shown excluding main flow top walls.

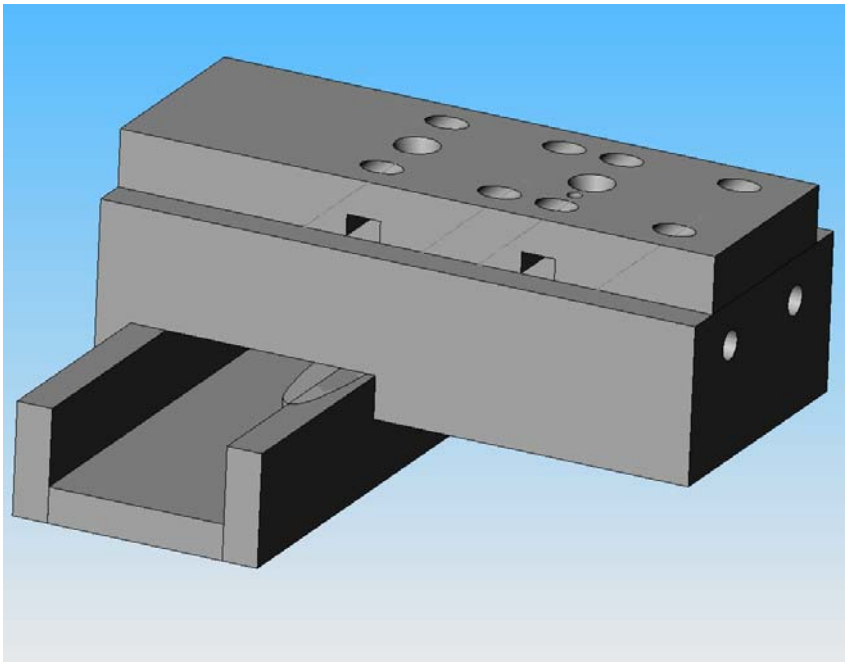

Figure 10: General design of UCC flat sector rig, shown excluding main flow top walls.

third, or 120 degree, section. At the beginning of the cavity, an end plug with two circumferentially aligned air inlets is installed, preceding the accompanying air inlet pairs on either side of the now first fuel injection point, thus providing enough air to meet the desired local φ_{cav} for this fuel injection point. The last pair of air inlets, following the second fuel injection point and over the main flow area, are retained for completeness of reproduction of the cavity and main flow interaction, in spite of their resultant air injection mostly traveling directly out the newly created cavity exhaust port for this non-periodic model. The total number of cavity air inlets for each sector rig is therefore 10, or 5 pairs.

Entrainment of the main flow into the cavity flow, and consequent increase in the flow out the cavity exhaust and decrease in the main flow exhaust was found to be an area of concern. While this is expected, based on the research of the TVC and previous UCC research, the creation of this non-periodic, non-re-circulating model does not offer a means to recover this loss. Reduction of the entrainment loss can possibly be attained by a reduction in the cavity exhaust area. On the curved cavity sector rig, this was accomplished with a reduction in the entrainment loss by extending the cavity top radius curvature completely over the main flow until intersection with the far wall plane, and retaining the wall height, producing a cavity exhaust height reduction from 0.8025 in to approximately 0.55 in. In light of the focus of the design of the sector rigs to examine the cavity-vane interactions, the mass loss from the main exhaust is not critical, but recognized as part of the flow characteristic to which this study is directed.

The two sector rigs included CIACs at each fuel injection point for flame stabilization. Additionally, with the experimental testing in mind, a small (0.05 in radius) ignition 'torch' inlet port was included in the CIAC adjacent to the first fuel injection point. This torch is to ensure prompt initial ignition and to prevent flame-out during testing, it will be modeled as a very small mass flow at 1500 K.

3.2.2 Grid Construction Techniques. The designed combustor configuration from *Solidworks* is next imported to *Gridgen* for use as the database for the numerical grid construction. Using *Gridgen*, for each combustor configuration, the numerical grid was constructed by first sanitizing the structure database of unnecessary or redundant segments. Then connectors are built upon the database segments to form the numerical outline, applying the desired grid spacing (Δs) at this point to the connectors. Next, unstructured, triangle cell domains were automatically constructed on each boundary surface using a domain boundary decay factor of 0.75. Finally, the interior, unstructured tetrahedral cell grid structure was generated using *Gridgen's* unstructured grid solver with a block boundary decay factor of 0.95, in all cases. To enhance the effectiveness of the grid solver and the high boundary decay factor, the interior was broken into two or three (flat and curved sector rigs only) blocks by interior domains.

For models requiring them, periodic surfaces were created during the domain construction step and set as either rotational (3-D axi-symmetric models) or translational (2-D flat model). General boundary conditions on all surfaces were defined prior to export of the grid to *FLUENT*.

3.2.3 Coarse versus Dense Grid. In modeling a fully turbulent, complex and dynamic flow as found within the UCC, the resolution of the turbulence models and overall solution is directly related to the density and resolution provided by the numerical grid. In the UCC flow, there are flow features ranging across many magnitudes of turbulent length scales throughout the interior of the combustor. As such, a high grid density is desired throughout the entire combustor volume to enable an accurate solution of the flow features. In choosing to utilize wall functions for the near wall treatment, cell sizing, and consequently spacing, at the exterior walls is dictated by the wall coordinate minimum value and optimal range for the wall functions. Additionally, in choosing a simplified cell solving method for grid blocks of building from the surface wall domains, as opposed to creating more complex inner cell partitions to highly influence local cell density and distribution (man-hour intensive and difficult to repeat on various configurations), the interior cell sizing becomes dependent on the size of the cells adjacent to the wall and the boundary decay factor used to generate the interior cell structure. Therefore, a balance was made with control of cell sizing throughout the grid with grid generation time, resulting in cell sizing being determined by setting grid spacing on the external surfaces to attempt to satisfy the wall function treatment, then tightly controlling cell size growth with boundary decay factors.

In reviewing and analyzing the models and actual datasets of the preceding CFD studies (Greenwood, 2005; Anisko, 2006) the resolution and accuracy provided by these coarse grids was found to be an area for possible improvement. While Anisko set his grid spacing in the cavity area of his coarse grids at 0.07 in., with the intent to allow the

wall bounding cell's y* to remain above the recommended y*>11.225 cut-off for the wall functions, large areas of the cavity grid still fell below y* of 11.225. This grid spacing created large cells, which combined with what appears to be the use of *Gridgen's* default boundary decay factor of 0.5, produced extremely large cell sizes in the cavity interior. As part of his CFD model validation process, he also created a denser grid, of approximately 1.12 million cells by decreasing cell spacing on the wall surface boundaries, but again the boundary decay factor created similarly large interior cells, and did not contribute to any appreciable improvement in the solution. Figure 11 depicts the cell sizing of Anisko's coarse grid on the 1.875 inch cavity experimental configuration.

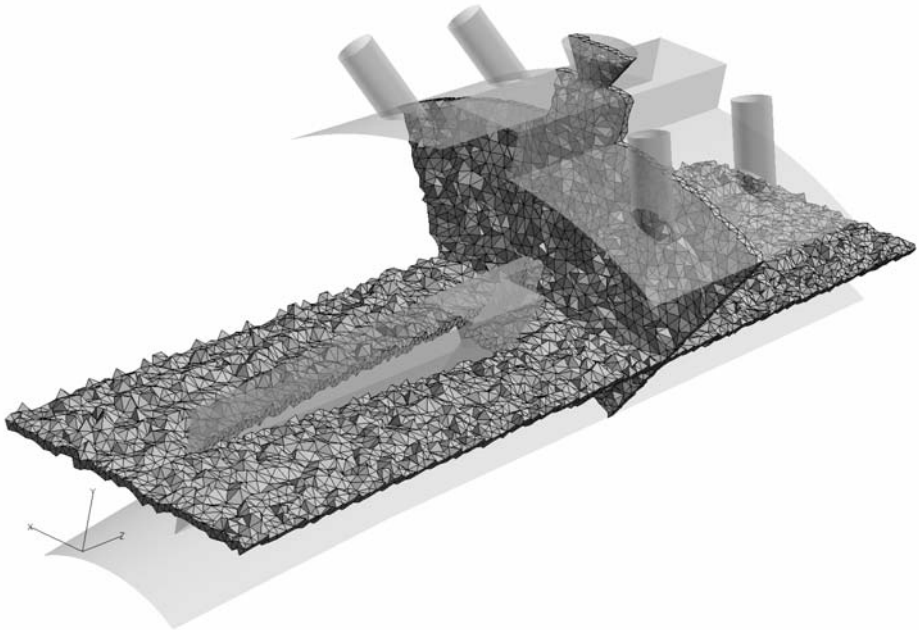

Figure 11: Coarse grid of 1.875 inch cavity UCC configuration from Anisko's research.

In improving the grid density to create a grid a reasonable accuracy, but without extremely high computational requirements, a baseline Δs=0.03 inches was used, increasing to 0.04 at the mass flow inlet, 0.035 in the cavity, and 0.02 at the cavity to exit wall corner. Combined with the aforementioned boundary decay control, this resulted in a grid of approximately 2.5 million cells for the long cavity model, a reasonable number for computational purposes, and as seen in Figure 12, it provides significant cell density with excellent smoothness for increased solution resolution throughout the combustor.

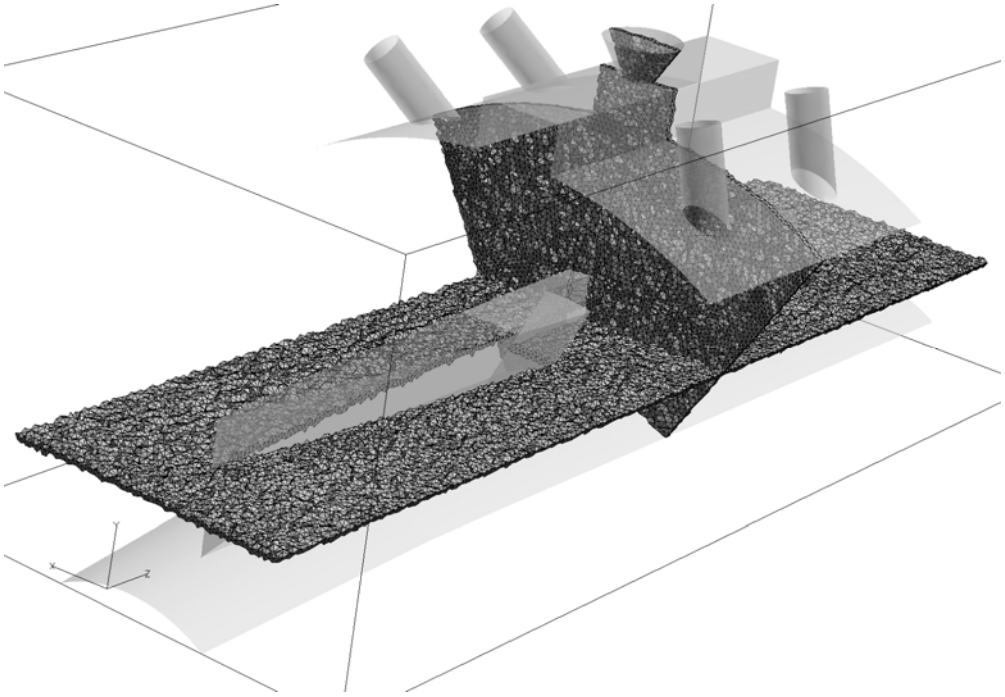

Figure 12: Improved dense grid of 1.875 inch cavity UCC configuration.

Preliminary solution results were examined to check the cell spacing parameters on the wall boundaries by use of y^* contours to ensure satisfactory spacing for the wall functions. As shown in Figure 13, the cell spacing is quiet satisfactory in the main flow

areas, but in the cavity area, the cell spacing is too small, with much of the cavity at or below the y^*=11.225 mark set to maintain the log-law relation. When Anisko's coarse grid was examined on the same conditions, with double the cell spacing in the cavity, the y^*contours in the cavity were very similar. Not surprising, as a equilateral tetrahedron's center point height is approximately 20% the value of a side, so a large cell size increase only results in a small increase in distance of the cell center from the wall.

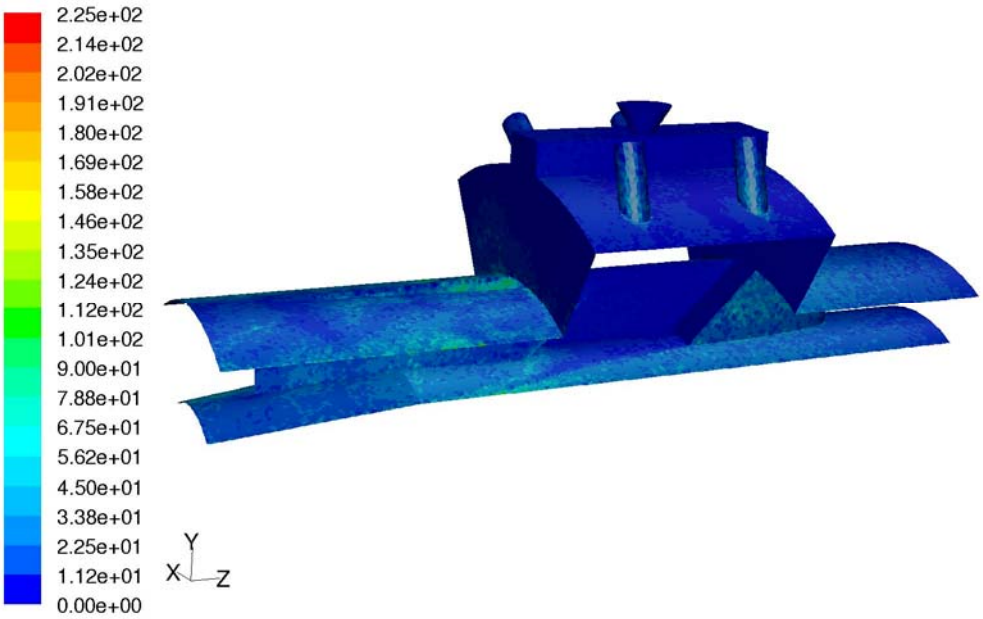

Figure 13: Wall y* contours of UCC long cavity configuration at LMLP operating condition. Note darkest blue areas are y*<11.225.

A review of Equation 7 to understand the calculation of y^* shows it to be directly proportional to density, where within the cavity area of the UCC are found significantly hotter temperatures. Additionally, the cavity is an area of slower velocities, particularly along the front and back vertical walls, and finally the cavity is an area very adverse to maintaining a boundary layer, with impinging jets imparting a radial inward velocity component, adverse pressure gradients, and buoyancy forces acting to separate the flow from the wall surfaces. As such, the validity of the y^* results in the cavity area is suspected to be inaccurate due to the flow complexities. With the desire of maintaining a dense grid within the entire cavity area, it is elected to maintain this grid spacing and accept the shortcoming of the wall functions reverting to the laminar stress-strain relationship at the near-wall cells in the cavity area.

3.2.4 Summary of Configurations and Numerical Models. The five configurations designed for CFD testing and analyses are displayed in Table 1. All configurations have a 0.5375-in. (13.7 mm) axial vane height and cavity air inlet diameter of 0.21-in (5.33 mm). Numerical grids were constructed using near identical cell spacing variations throughout the grid, as previously identified.

Table 1: Numerical Model Configurations.

Configuration	Cavity Length-in (mm)	Cavity Inlet Angle (deg)	# of Cavity Inlets	# of Cells
"Experimental"	1.875 (47.6)	37	4	2,525,958
3-D Baseline	1.5 (38.1)	45	4	2,270,650
2-D Flat Baseline	1.5 (38.1)	45	4	2,117,707
Curved Cavity Sector Rig	1.5 (38.1)	45	10	2,551,973
Flat Cavity Sector Rig	1.5 (38.1)	45	10	2,640,312

3.3 Numerical Methods

3.3.1 Experimental and Numerical Operating Conditions. Experimental results for several operating conditions run on the 1.875-inch cavity configuration by AFRL Propulsion Directorate were obtained and reduced by Greenwood, to use as a baseline for research and validation of the CFD model, and subsequently used by Anisko's continuing research for same. Three of these five operating conditions will be used for validation in this study. The experimental loading conditions used to define the CFD model's operating boundary conditions are displayed in Table 2, where LMLP defines the low mass/low pressure case, LMMP defines the low mass/medium pressure case, and HMHP defines the high mass/high pressure case.

Table 2: Experimental Operating Conditions on Full UCC Test Model.

Operating Condition	$\dot{m}_{main}$ $\frac{lb_m}{\min}$ $\left(\frac{kg}{\min}\right)$	$\dot{m}_{cav}$ $\frac{lb_m}{\min}$ $\left(\frac{kg}{\min}\right)$	P_3 (psia)	dP/P (%)	T (K)	$\varphi_{overall}$	φ_{cav}	CLP
Case 1 (LMLP)	29.1 (13.2)	6.4 (2.9)	41.2	5.0	528	0.294	1.620	0.300
Case 2 (LMMP)	29.7 (13.5)	6.2 (2.8)	49.4	3.3	541	0.289	1.677	0.204
Case 3 (HMHP)	65.0 (29.5)	6.2 (5.8)	59.2	8.3	550	0.147	0.899	0.281

Table 3 displays the variable operating conditions used in this research, based on the one-sixth, 60-degree model of the full UCC. Cavity air mass flow rate is indicated for total cavity rate (4 cavity inlets on 3-D model), and is adjusted to reflect 10 inlets for sector rig models. Fuel mass flow rate is also indicated for 3-D models, with only per fuel injector, and is doubled for the sector rigs containing two fuel injectors. The three experimental data operating conditions (LMLP, LMMP, HMHP) are to be analyzed on the 3-D axi-symmetric experimental and short cavity baseline models, as well as the 2-D

flat periodic model. The experimental LMLP condition and two atmospheric pressure conditions, ATM1 and ATM2, not based on any experimental data but derived from the LM condition as 50% and 40% mass flow rates, will be used to analyze both sector rigs for comparison with the 3-D baseline model. While the sector rigs will not be experimentally tested at the higher pressure condition (LMLP), this operating condition is used in their evaluation based on its basis from actual experimental data.

Table 3: Operating Conditions for CFD 3-D, 60-degree models.

Operating Condition	$\dot{m}_{main}$ $\frac{lb_m}{\min}$ $\left(\frac{kg}{\min}\right)$	$\dot{m}_{cav}$ $\frac{lb_m}{\min}$ $\left(\frac{kg}{\min}\right)$	$\dot{m}_{fuel}$ $\frac{lb_m}{\min}$ $\left(\frac{kg}{\min}\right)$	P_{op} *(psia)*	P_4 *(psia)*	T_3 *(K)*
LMLP	4.844 (2.197)	1.072 (0.486)	0.1178 (0.0534)	40.5	39.7	532
LMMP	4.951 (2.246)	1.032 (0.468)	0.1187 (0.0538)	48.6	47.8	541
HMHP	10.833 (4.914)	2.12 (0.962)	0.1304 (0.0591)	57.4	55.4	553
ATM1	2.422 (1.099)	0.536 (0.243)	0.0589 (0.0267)	14.7	13.9	532
ATM2	1.938 (0.879)	0.429 (0.195)	0.0471 (0.0214)	14.7	13.9	532

3.3.2 Boundary Conditions. In *FLUENT*, the numerical grid is defined with the following boundary condition types to simulate the experimental models: solid walls modeling convection and radiation heat transfer, mass-flow inlets for main and cavity air inlets, pressure outlets for main and cavity outlets (cavity outlet on sector rigs only).

For the DPM liquid fuel stream, the combustor walls are modeled as 'wall-jet', for a non-elastic particle reflection on the surface. The heat transfer characteristics used are as initially formulated and calculated by Greenwood. As previously stated, a radiation emissivity of 0.85 is used on all mixed (convection and radiation) surfaces. The convective heat transfer coefficient, $\bar{h}$, is calculated using Equations 33 and 34 for each specific surface. The combustor main center-body and axial vane are modeled as

adiabatic based on symmetry. The cavity top surface is modeled as convective only, with T_s=1100 K and the adjoining free-stream area the cavity air plenum at T_∞=500 K, for $\bar{h}$=8.1 W/m^{2}K. The front and rear cavity flanges, or radial walls, were similarly modeled for $\bar{h}$, and radiation included for mixed treatment. The inlet and outlet walls are modeled mixed and calculated for T_s of 500 K and 1100 K, respectively, and T_∞=300 K, for $\bar{h}$ values of 10.2 W/m^{2}K and 12.1 W/m^{2}K (Greenwood, 2005:2-8,3-8). Extending the heat transfer model to the 2-D models with additional wall surfaces, the cavity floor was assumed part of the cavity and the flat bottom, sides, and axial vanes of the rectangular main flow area was assumed as the vane center-body.

Mass-flow-inlets are used for the cavity and main air inlets, allowing control of mass flow to accurately match the experimental conditions. Total temperature is input to match experimental inlet temperature. Pressure becomes solution dependent for this type of inlet. Mean mixture fraction is left at zero. Inlet turbulence parameters were set at 3.0% intensity, with a length scale derived from the appropriate hydraulic diameter. The DPM boundary condition was set to escape for inlets.

Pressure-outlets are used for the exhaust exit(s) of the models. *FLUENT* relates pressure by the relation

$$p_{abs} = p_{op} + p_{gauge} \tag{43}$$

where the operating pressure, p_{op}, is specified in the combustion species transport PDF. It should be approximately the mean absolute pressure of the overall simulation, it is the pressure used to pre-calculate the PDF, and it is the pressure for all chemistry

calculations (without compressibility effects option). Gauge, or static pressure, p_{gauge}, is how boundary condition pressures are defined, as relative to the already specified p_{op} (Fluent Inc, 2005:8-64).

Therefore, the pressure for the entire flow field is calculated upstream from the exhaust, and to match an experimental inlet pressure, a little trial and error with the boundary condition and the solution is used to reach a reasonable accommodation of the inlet pressure and operating pressure for the desired operating condition. For this research, once a p_4 and p_{op} was established on the experimental configuration for each operating condition, it was used identically for subsequent configurations. Backflow parameters for the outlets were set at ambient temperature and turbulence intensity 3.0% and appropriate hydraulic diameter for length scale. Pressure-outlets were set as escape boundaries for the DPM model.

Of note, the setting of the pressure-outlet boundary condition was in error for the research models of Greenwood and Anisko. For comparison data presented herein from Anisko's research, the results are obtained by re-solving the coarse grid models for a solution with corrected pressure boundary conditions.

3.3.3 Periodic Boundaries. For the 3-D axi-symmetric models, a 60-degree rotationally periodic boundary condition was set for each side of the wedge, including the cavity and main flow sides. Care was taken in the design and grid generation process's to ensure exact angular relations where maintained. The 2-D flat periodic model used a translational periodic boundary for the cavity flow only. For *FLUENT* periodic boundary controls, no mass flow or pressure gradient was set.

Since *FLUENT* has some rigid, but confusing rules on DPM use and periodic boundaries, the periodic boundaries were checked on each configuration model to ensure the continuous flow and DPM particle tracks crossed the periodic boundaries correctly. The final dense 2-D flat periodic model did encounter some difficulties with the DPM particles crossing the periodic boundary. For reasons unknown, some particles would cross the translational periodic boundary, while others would not. For the 2-D flat periodic model on the LMLP and LMMP conditions, approximately 5 percent of fuel particles aborted prior to reaching a definitive fate, whereas for the HMHP case, over 30 percent aborted.

3.3.4 Turbulence Modeling. Previous UCC CFD studies have used the standard k-ε turbulence model. However, with the significantly denser grid constructed for the models, and in the interest of producing a simulation reflective of actual experimental physical results, the RNG k-ε turbulence model is to evaluated in the validation phase against the standard k-ε turbulence model on the experimental configuration at the LMLP operating condition. Based on this evaluation, the RNG k-ε turbulence model is then used for the remainder of the study, with the inclusion of the non-equilibrium wall functions. Differential viscosity formulation, RNG swirl dominated flow modification (highly swirled flow, swirl constant increased), and viscous heating options were not selected in the interest of making incremental changes to the previous CFD model.

3.3.5 Combustion and Species Transport Modeling. The *FLUENT* non-premixed combustion model for reaction and species transport modeling is set to solve on a chemical equilibrium basis, using 11 chemical species. The experimental configuration

is run on JP-8 jet fuel, which is kerosene based. Therefore, kerosene, with the primary hydrocarbon $C_{12}H_{23}$, is selected as the fuel species. The remaining species include air, as N_2 and O_2 at 79% and 21%, for the oxidizer, N_2, H_2, C(solid), CO, CO_2, CH_4, OH, and H_2O(liquid). The rich flammability limit, RFL, is set to 0.293 fuel-air ratio. Once the operating pressure is set for the desired operating condition, the PDF tables are then pre-calculated by *FLUENT*.

3.3.6 Fuel Injection. The DPM fuel injection profile initially was to follow the distribution pattern investigated and developed by Greenwood, for a mean droplet diameter of 55 μm ,varied by +/- 5 μm and 15 μm, and using cones with half angles from 30-40 degrees, at a velocity of 30.5 m/s (Greenwood, 2005:3-1, 4-25, 4-26). However, preliminary analysis of the experimental configuration results, also compared with Anisko's results on the coarser grid, revealed the combustion efficiency was almost entirely dependent on UHCs of the liquid phase from fuel particles escaping through the exhaust prior to full evaporation. Visual analysis of the particle tracks revealed approximately 50% of the 70 μm stream particles escaped prior to evaporation. It was found the majority of these were particles injected on the upwind side of the fuel injection cone, resulting in an immediate downward trajectory that placed them in the main flow upwind of the axial vane. This is a large cool area of flow along the side of the vane, and thus these particles do not having any increased temperature benefit to improve evaporation. The 60 μm particle tracks faired only slightly better. Figure 14 displays twenty percent of the particle tracks for the 70 μm injection colored by diameter, for comparison with Figure 15 of the 50 μm injection of same injection parameters, both

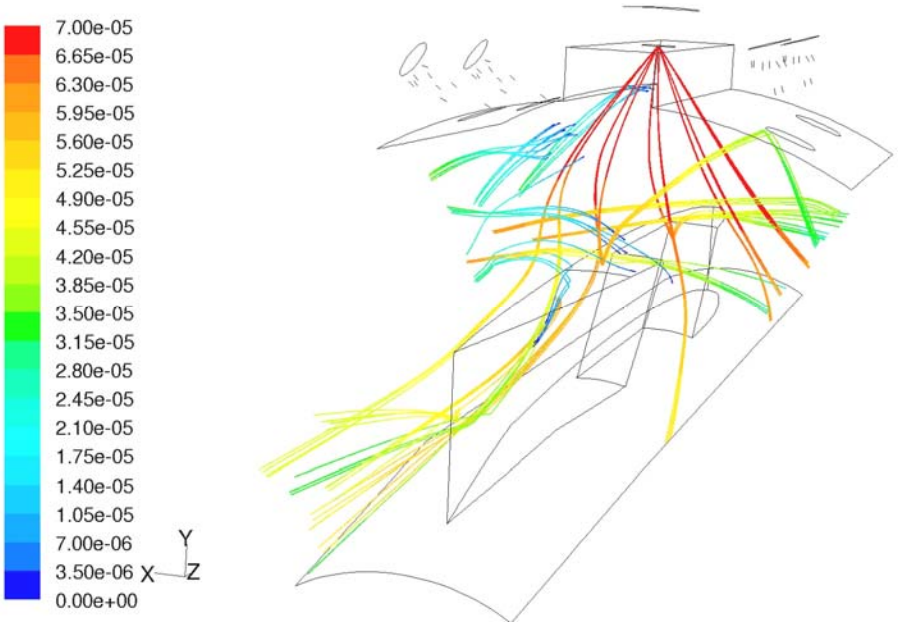

Figure 14: Fuel particle tracks of 70 μm mean diameter injection in experimental configuration, LMLP condition solution, colored by mean diameter (m).

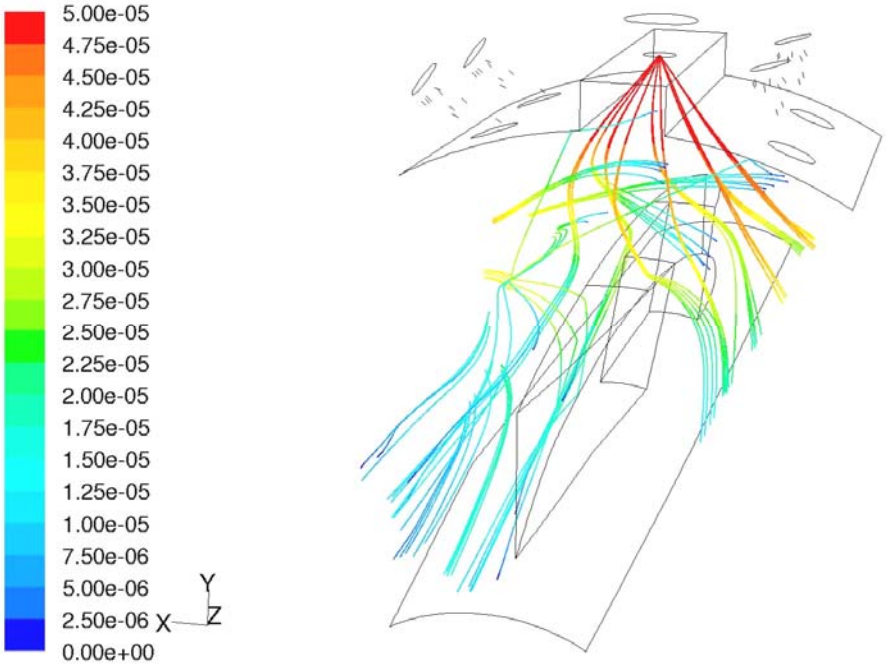

Figure 15: Fuel particle tracks of 50 μm mean diameter injection in experimental configuration, LMLP condition solution, colored by mean diameter (m).

for the experimental configuration LMLP condition. Note the reduced particle diameter at the exhaust plane for the smaller droplets.

A reduction in the mean fuel drop diameter was deemed necessary to allow for better evaporation, combustion, and hopefully a more accurate solution for examination. Additionally, it was desired to not add particles of a smaller diameter than already used, so a mean diameter of 45 μm was selected, but with the diameter variance reduced to a maximum of +/-5 μm. The fuel injection spray parameters used for all models are shown in Table 4.

Table 4: Fuel Droplet Spray Model.

Injection	Cone Half Angle	Droplet Diameter (μm)	Percent Fuel Flow
0	40	40	10
1	30	42.5	25
2	35	45	30
3	32	47.5	25
4	38	50	10

The Discrete Phase Model set up for *FLUENT* was completed by setting the stochastic tracking parameters with the maximum number of steps to 15 million, with a step length factor of 5, to accommodate the 2.5 million cell grid. The DPM was set to interact with the continuous phase at a rate of one DPM iteration per twenty continuous phase iterations. The DPM under-relaxation factor was reduced from 0.5 to 0.45 to enhance stability.

3.3.7 Pollutant Modeling. The NO_x modeling was set up to for prompt and thermal NO_x data. Thermal NO_x is set to model based on temperature, and Prompt NO_x

is set to model based on $C_{12}H_{23}$ as the combusting hydrocarbon at an overall equivalence ratio of 0.29.

3.3.8 Solver and Solution Procedure. *FLUENT* was set as a 3-D, double precision, segregated, implicit steady state solver, and using 2nd order upwind discretization for all equations. Slight reductions in default under-relaxation factors were used for density, body forces, energy, and temperature.

The general solution procedure for all configuration and case runs was to initialize the solution field from an average of all fields following set-up. Next, as recommended by *FLUENT,* an approximate continuous phase only (DPM fuel off) solution was achieved by solving for 3,000 iterations. At this point, the DPM fuel injection was activated and the iterations continued, running out to a range of 8,000 to 15,000 total iterations, depending on the case. All cases were run on eight parallel processors to speed the computational time.

3.3.6 Solution Convergence Criteria. Various methods and practices exist for judging solution convergence. One is to evaluate the reduction in the magnitude toward zero of the residual factors, with a general practice (and *FLUENT* default) as the measure of reaching 1e-06 for the energy equation, and 1e-03 for all others. Complex, turbulent flows, however, often do not reach these criteria, as was the case for this problem. Further analysis of the residual trends, such as whether the solution stabilizes, and examination of performance measures for the problem can then be used to judge if the solution is converged, or accurate to the level desired (Fluent Inc, 2005:26-128, 26-129).

3.4 Combustor Configuration Performance Evaluation and Comparison

3.4.1 Qualitative Measures of Performance Comparison. Each combustor configuration will be examined using flow visualization to evaluate velocity, temperature, and turbulence intensity characteristics of the flow field in particular, and pressure, density, and species levels in general.

For simplicity, specific flow field planes are used for visualization and quantitative measures of properties, as shown in Figure 16. These planes are common to all configurations. The 'cavity fuel' plane provides characteristics of the cavity circumferential flow in the cavity center, without excessive washout by the outboard cavity inlet flows. The 'cavity-vane' axial plane is on the axial vane centerline, with the lower vane area 0.05 inch from the RVC wall, and provides a cross section of the cavity flow at the fuel injection point and the RVC flow dynamics. This plane is reduced to the 'cavity cross-section' plane (includes CIAC) by removing the area in RVC below the cavity. The 'U_θ' plane is a further reduction of the 'cavity cross-section' plane, eliminating the CIAC to provide accurate cavity velocity evaluation. The 'half vane' plane provides main channel flow visualization at one-half axial vane height. The 'outlet' plane consists of the exhaust boundary plane to evaluate the exhaust parameters.

3.4.2 Quantitative Measures of Performance Comparison. Accurate performance measures are critical in evaluating the combustor's performance and comparing the various configurations. Various measures will be used to analyze specific performance and relative performance with respect to the configuration design process.

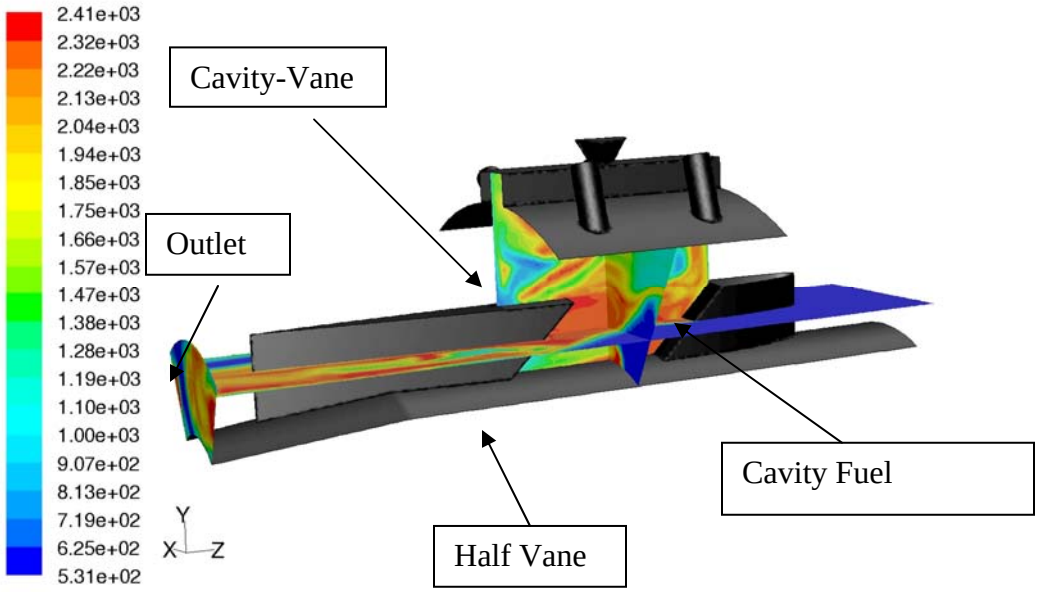

Figure 16: Location of visualization and evaluation planes on 3-D experimental configuration, LMLP condition, with contours of temperature (K) shown. Combustor flow is right to left.

Combustor emissions (CO, CO_2, O_2, UHC, NO_x), efficiency (η_b), temperature distribution, and pressure loss will be evaluated at the outlet. Mass flow comparisons will be made at the cavity cross-section plane and outlet. Overall flow velocities will be examined at the outlet, cavity velocities and g-loads will be evaluated on the U_θ plane.

IV. Results and Discussion

4.1 3-D Experimental Configuration, Improved CFD Model Evaluation and Comparison with Experimental and Coarse Grid CFD Data

The first step of the design process was completed with the implementation of the numerical grid density improvements and CFD modeling changes in the problem set-up for *FLUENT*, and applied to the experimental configuration (1.875 in long cavity with 37^o cavity air inlets). The standard k-ε turbulence model with standard wall functions on the improved grid solution was performed for the LMLP case only, while the RNG k-ε turbulence model with non-equilibrium wall functions was performed on the LMLP, LMMP, and HMHP cases. The results of these solutions will be compared with the available experimental data and the results of Anisko's coarse grid solution (standard k-ε turbulence model, standard wall functions, 55 μm mean droplet diameter, cases re-run for solution with correct pressure boundary condition treatment). Flow visualization evaluation will be shown for the LMLP case.

To briefly discuss judgment of solution convergence, for the standard k-ε turbulence model, experimental configuration, LMLP condition, the residual levels were close to the quantitative measure of convergence, within an order of magnitude of convergence, but stabilized and not indicating further decrease after 8,000 to 10,000 iterations. Performance measures did not vary significantly over subsequent iterations.

The experimental configuration, RNG k-ε turbulence model, LMLP condition was extensively examined at various points in the iterative process, out to 15,000 iterations, to

evaluate the behavior, stability and accuracy of the solution. Residual levels for continuity, energy, and ε were increased over those found on the standard *k-ε* turbulence model solution by approximately an order of magnitude, remaining in the range of 1e-01 for continuity and ε, and the range of 1e-03 for energy, with no definitive trends to indicate further decrease would occur. An area of residual increase occurred in the 12,000 to 13,000 iteration range, resulting in a measured performance decrease in combustion efficiency from significantly increased CO emissions (1,500-2,000 ppm increased to 4,000-5,000 ppm). By 14,000 to 15,000 iterations, the residuals and performance levels returned to the pre-instability levels. Thus, it was determined 10,000 to 11,000 iterations is generally sufficient for a consistent solution on the RNG *k-ε* turbulence models, checking to ensure a range of residual increase has not begun.

The significant increase in CO emissions and resultant decrease in efficiency, combined with observed statistically significant variations in all performance measures across the iteration points examined and the high residual levels, indicates the RNG *k-ε* turbulence model is causing the solution to act in an unsteady or transient manner across series of iterations. This is caused by the high responsiveness of the model combined with the truly unsteady nature of the UCC's highly turbulent flow characteristics. Therefore, the solutions evaluated and presented here for the RNG *k-ε* turbulence models are to be considered a snapshot of the unsteady, turbulent flow, with performance measures carrying a reasonable amount of error.

4.1.1 Performance and Emissions Data Evaluation. Table 5 displays the emissions and performance data for the experimental configuration, where the LMLP

condition is evaluated at 12,000 iterations (s *k-ε*) and 15,000 iterations (RNG *k-ε*), the LMMP condition is evaluated at 10,000 iterations, and the HMHP condition is evaluated at 11,000 iterations. In calculating the emissions data (all configurations and conditions), it was observed the $C_{12}H_{23}$ species mole fraction, defining evaporated unburned UHC particles, was extremely small and insignificant to the combined UHC level. This is attributed to the chemical equilibrium reaction modeling, whereby the evaporated fuel is quickly reacted, and represents an elevated level of performance over what would occur in actual experimental performance. Further evidence of this can be seen in the elevated CO and CO_2 levels and the reduced O_2 level on the LMLP and HMHP conditions.

Table 5: Emissions and efficiency performance data for 3-D Experimental Configuration (1.875 inch cavity), comparing experimental data, coarse grid solution, and dense grid solution.

Op Cond	Model	CO(ppm)	CO_2 (%)	O_2 (%)	NO_x (ppm)	UHC (ppm)	η_b (%)	dP/P (%)
LMLP	Expr	1089	3.2	16.4	37.3	45.3	97.5	5.00
	3-D Coarse	1377.10	3.69	14.99	38.76	118.27	94.90	3.762
	3-D sk-ε	1993.74	3.79	14.81	47.23	5.69	97.53	3.743
	3-D RNGk-ε	1511.64	3.86	14.73	25.40	30.90	97.33	4.051
LMMP	Expr	1264	3.7	15.7	48.2	28.2	97.7	3.30
	3-D Coarse	1423.25	3.74	14.91	54.86	78.86	95.95	2.744
	3-D RNGk-ε	2330.65	3.37	15.42	50.87	5.67	97.13	2.500
HMHP	Expr	478	1.60	18.70	15.60	15.60	98.00	8.300
	3-D Coarse	287.19	1.78	18.16	15.93	43.28	96.49	6.389
	3-D RNGk-ε	147.98	1.84	18.08	26.31	2.88	99.50	5.964

Evaluation of the LMLP data shows improved combustion efficiency in relation to the coarse model, much more closely replicating the experimental data, for both the dense standard *k-ε* and RNG *k-ε* turbulence model solutions. This is a result of decreased UHC levels and is in spite of increased CO levels as compared to the experimental data. The dense standard *k-ε* solution has elevated CO levels and decreased UHC as compared

with the dense RNG k-ε solution, indicating improved fuel droplet evaporation but less effective mixing and reacting in the standard k-ε solution. The LMMP data displays a similar trend, and the HMHP data indicates improved performance in all measures. Pressure loss data indicates better efficiency over the experimental data and roughly equal to or improved when compared with the coarse model. Interestingly, the pressure loss data for the dense standard k-ε model closely matches the coarse model data, and is also lower than the RNG k-ε model for the LMLP condition.

4.1.2 Overall Solution Visualization. Before a detailed analysis of specific areas in the flow solution, an overview of the entire combustor flow to understand its characteristics and complexities is appropriate. Figure 16 illustrates the temperature profile of the combustor displayed as contours on the four primary planes of interest, and is complimented by Figure 17, where velocity vectors indicate flow details, colored by temperature viewed on the same planes.

The temperature contours show, for this cavity fuel rich burning condition, where the basic combustion zones are occurring. In this case, it is evident the hot reaction is continuing from the cavity primary zone, through the RVC intermediate zone, and into the dilution zone of the main flow channel, with areas of burning, indicated by high temperature, reaching the outlet plane. CO emissions can increase in areas of high temperature burning, and an examination of the CO species contours indicated CO is produced along the residual higher temperature burning trails wake leading down the axial vane to the outlet. Also evident is an area of burning on the upwind side of the axial vane, indicating an area of hot combustion products pulled into the main flow by the

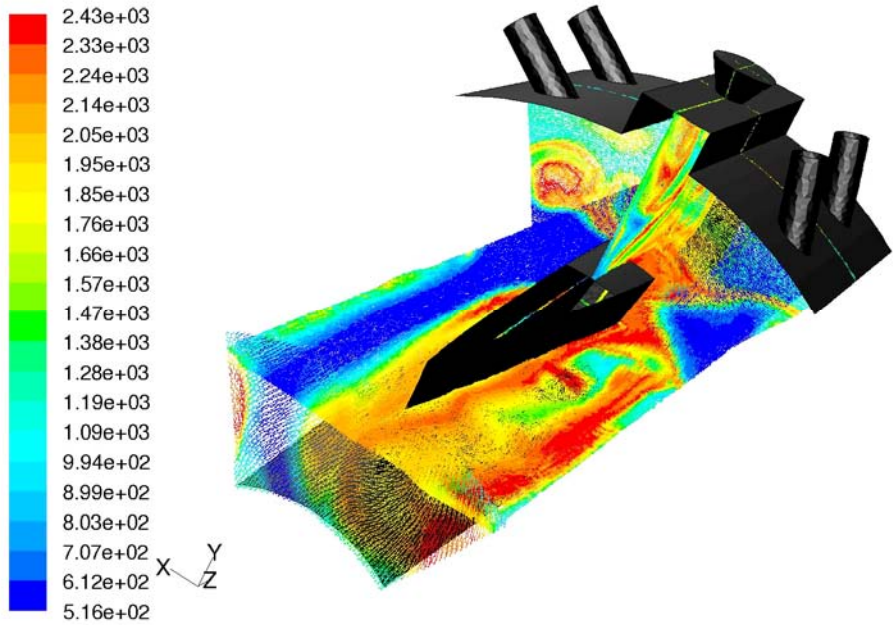

Figure 17: Velocity vectors colored by temperature (K) for the experimental configuration, LMLP condition, RNG *k-ε* turbulence model, viewed facing exhaust outlet.

accelerating flow along the upwind side of the axial vane. In the cavity fuel plane, or cavity centerline, the temperature pockets of hot and cold areas are evident, corresponding with the buoyancy forces that move colder bubbles outward and hotter bubbles inward. Examination of the mean mixture fraction contours showed most cold areas in the cavity are areas of unburned fuel mixture, unless the colder air was entrained from the zero mean fraction main channel flow.

Lastly, two areas of swirling, vortex structures are evident in the interaction and mixing between the cavity and main flow. One formed directly into the RVC, and the second just past the periodic boundary and midway point between the axial vanes. These vortex structures are the mixing element moving the cavity flow into the main flow, when they correspond to a pocket of hot combustion products they serve to transport the hot,

buoyant areas out of the cavity. The second of the vortices actually exchanges mass in both directions, as it also entrains a portion of cold main channel flow up into the cavity.

Figures 18 and 19 introduce the velocity and turbulence intensity contours to further illustrate the large scale, complex flow characteristics of the UCC. The velocity and turbulence intensity contours show the varying velocities and swirling in the cavity across both the cavity-vane plane and the cavity fuel plane. The interaction of the cavity flow into the main channel can again be seen in the turbulence intensity contours as large vortex structures on the cavity fuel plane, corresponding with the velocity vectors of Figure 17. This interaction continues in the form of high turbulence intensity and accelerating velocity (also due to the inter-vane passage constriction) proceeding down the main channel after the cavity. It is also evident the areas of high turbulence intensity in the main channel toward the exhaust are the extended turbulent shed vortices carrying the hot gases from the cavity as generated by the RVC. Areas of relatively low turbulence intensity main channel flow correspond to colder gases that did not mix with the cavity flow.

While not shown, visualization and analysis of the LMMP condition, also fuel rich in the cavity, displays similar contours for temperature, velocity, and turbulence intensity. Additionally, the HMHP condition, with a slightly lean fuel-air ratio in the cavity, is indicative of the desired rich-burn, quench, lean-burn mode of reaction for more complete burning in the cavity, due to both the lean mixture and increased evaporation at high pressure, with only minor residual burning occurring down the main channel flow.

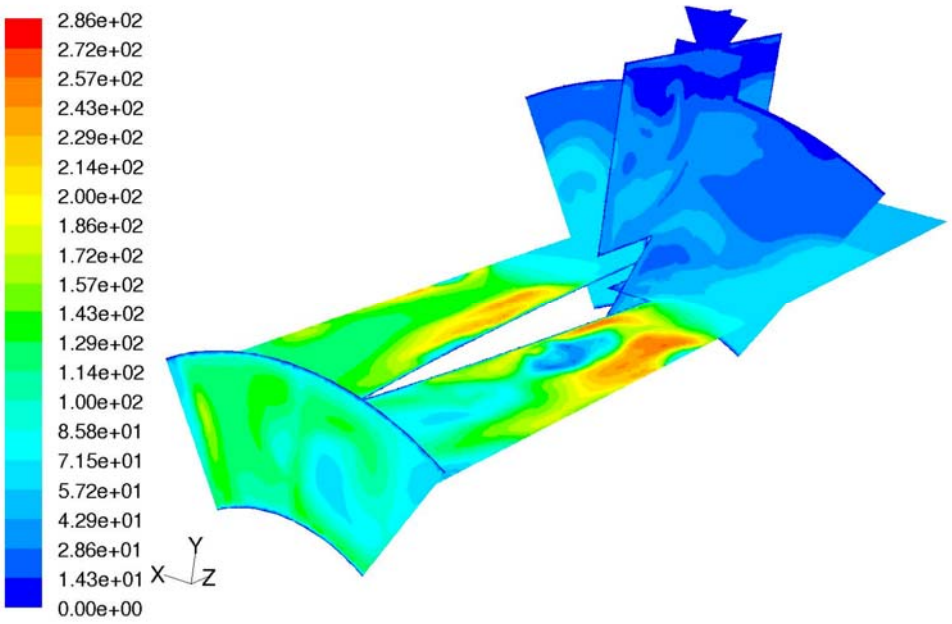

Figure 18: Contours of velocity magnitude (m/s) on experimental configuration, LMLP condition, RNG *k-ε* turbulence model.

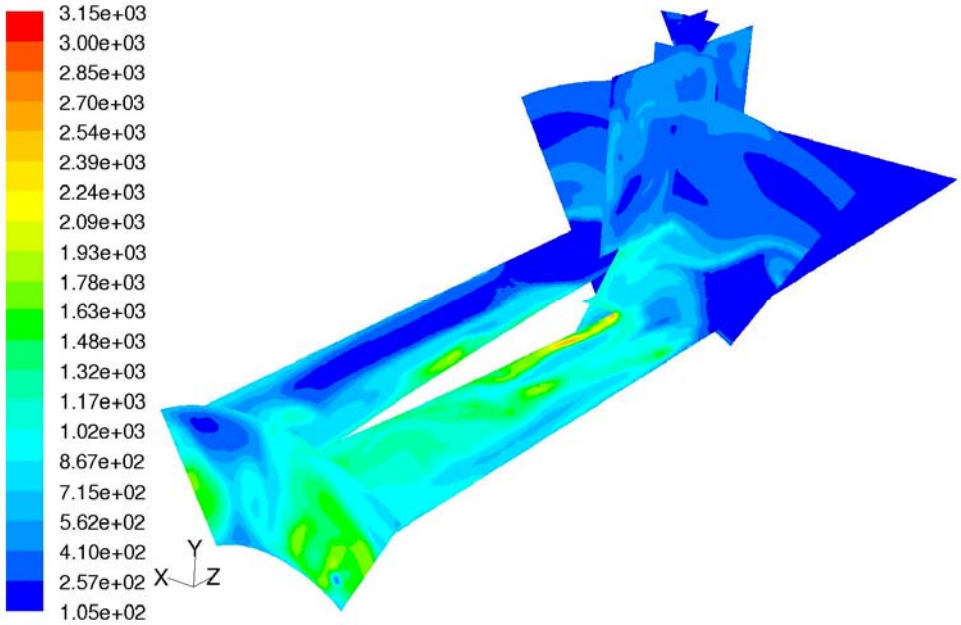

Figure 19: Contours of turbulence intensity (%, read as e+01) on experimental configuration, LMLP condition, RNG *k-ε* turbulence model.

The HMHP condition does portray similar velocity and turbulence intensity patterns throughout, specifically including the cavity-vane and main flow interaction.

Next, an overview of the standard *k*-*ε* turbulence model, LMLP condition, is accomplished with Figures 20 and 21 to examine the overall flow with velocity vectors colored for temperature and turbulence intensity contours. The standard *k*-*ε* model displays several differences when compared with the RNG *k*-*ε* model. While the performance data, as already reviewed, indicates very similar overall performance, the visualization here indicates a difference in how it is achieved. The standard *k*-*ε* solution does not have the clarity of flow detail of velocity or temperature contours as achieved by the RNG *k*-*ε* model solution, and the temperature and turbulence intensity gradient changes are not as distinct. Further, where the RNG *k*-*ε* model depicted clear vortex

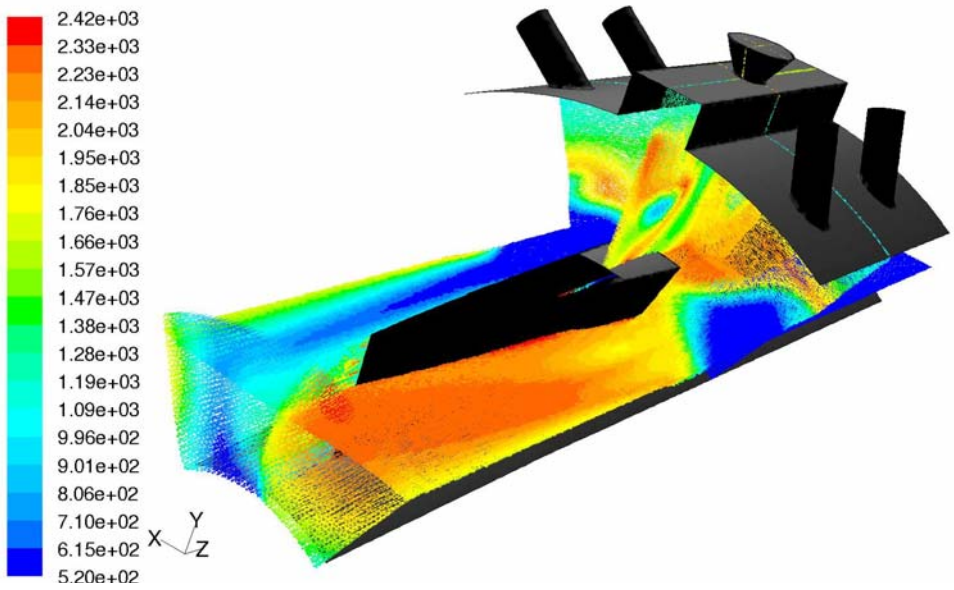

Figure 20: Velocity vectors colored by temperature (K) for the experimental configuration, LMLP condition, standard *k*-*ε* turbulence model.

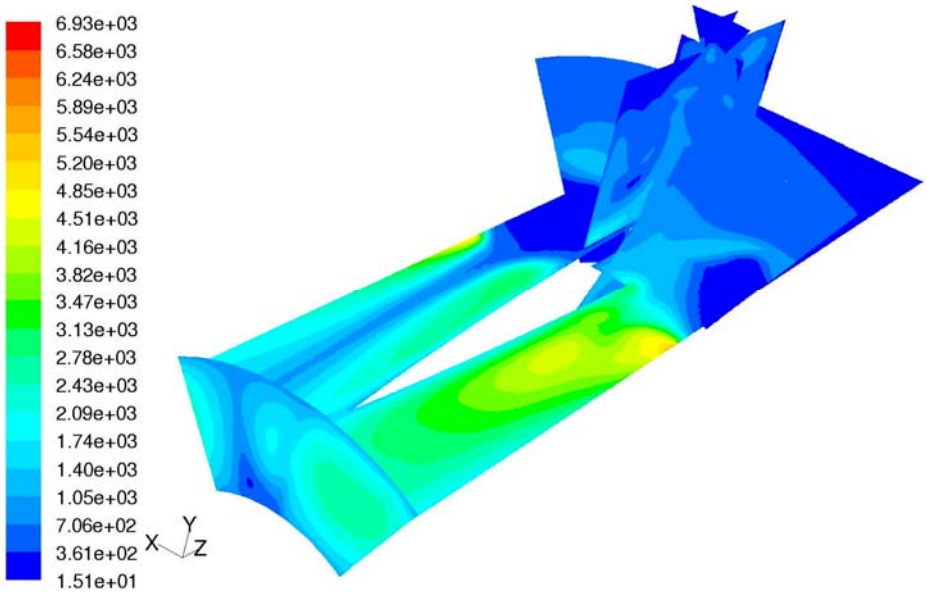

Figure 21: Contours of turbulence intensity (%, read as e+01) on experimental configuration, LMLP condition, standard *k-ε* turbulence model.

structures extending the length of the outflow, the turbulence intensity contours for the standard *k-ε* solution dissipate rapidly. Significant differences in the cavity mixing are also evident, to be discussed in the next section. Of course, these differences are anticipated, as the RNG *k-ε* turbulence model contains improvements to include the effects of swirl on the flow and the additional term in the turbulence dissipation rate equation to improve accuracy in highly strained flow.

4.1.3 Cavity Flow, G-loading, and Cavity-vane Interaction Evaluation. Of primary interest in designing and evaluating the UCC, the cavity flow and its interaction with the main flow is the major area of interest for this study, and is also another critical area to evaluate the quality of the CFD model. As discussed, the successful design of a non-recirculating sector rig is contingent upon recreating the cavity flow across the top of

the axial vane, to produce an accurate interaction between the main and cavity flows. Both qualitative and quantitative measures are used here to first analyze the characteristics on the 3-D experimental configuration model.

Table 6 indicates the flow parameters for the experimental configuration cavity, where CLP is calculated from Equation 35, mass flow is indicated for cavity air inlets and mass flow crossing the cavity cross-section plane (includes CIAC), and velocities are mass weighted averages for tangential and radial components computed on the U_θ plane (excludes CIAC). The data quantifies the mass entrainment in the cavity, with a range of entrainment from two to three times the air injection rate. This also produces effective tangential velocities for g-loading, and the radial velocities indicate there is good mass exchange into the main flow via buoyancy effects or radial velocities imparted by the angled air inlets.

Table 6: Cavity flow parameters for experimental configuration, with mass weighted average velocities for U_θ plane.

Op Cond	CLP	$\dot{m}_{cav}$ $\frac{lbm}{\min}\left(\frac{kg}{\min}\right)$	$\dot{m}_{cavplane}$ $\frac{lbm}{\min}\left(\frac{kg}{\min}\right)$	U_θ (m/s)	U_r (m/s)
LMLP-RNGk-ε	0.296	1.072 (0.486)	2.601 (1.180)	34.62	-7.62
LMLP-sk-ε	0.298	1.072 (0.486)	2.572 (1.167)	35.80	-7.22
LMMP	0.206	1.032 (0.468)	2.323 (1.054)	26.43	-5.63
HMHP	0.281	2.120 (0.962)	6.631 (3.008)	46.39	-9.37

An examination of the cavity fuel plane, shown in Figure 22 for the experimental configuration LMLP condition for both turbulence models displaying velocity vectors and temperature contours, shows the mixing and buoyancy effects of the centrifugal-force combustion. Both models provide excellent temperature profiles of the cavity, with the RNG *k-ε* model providing more detailed mixing effects. Also, the two vortex structures

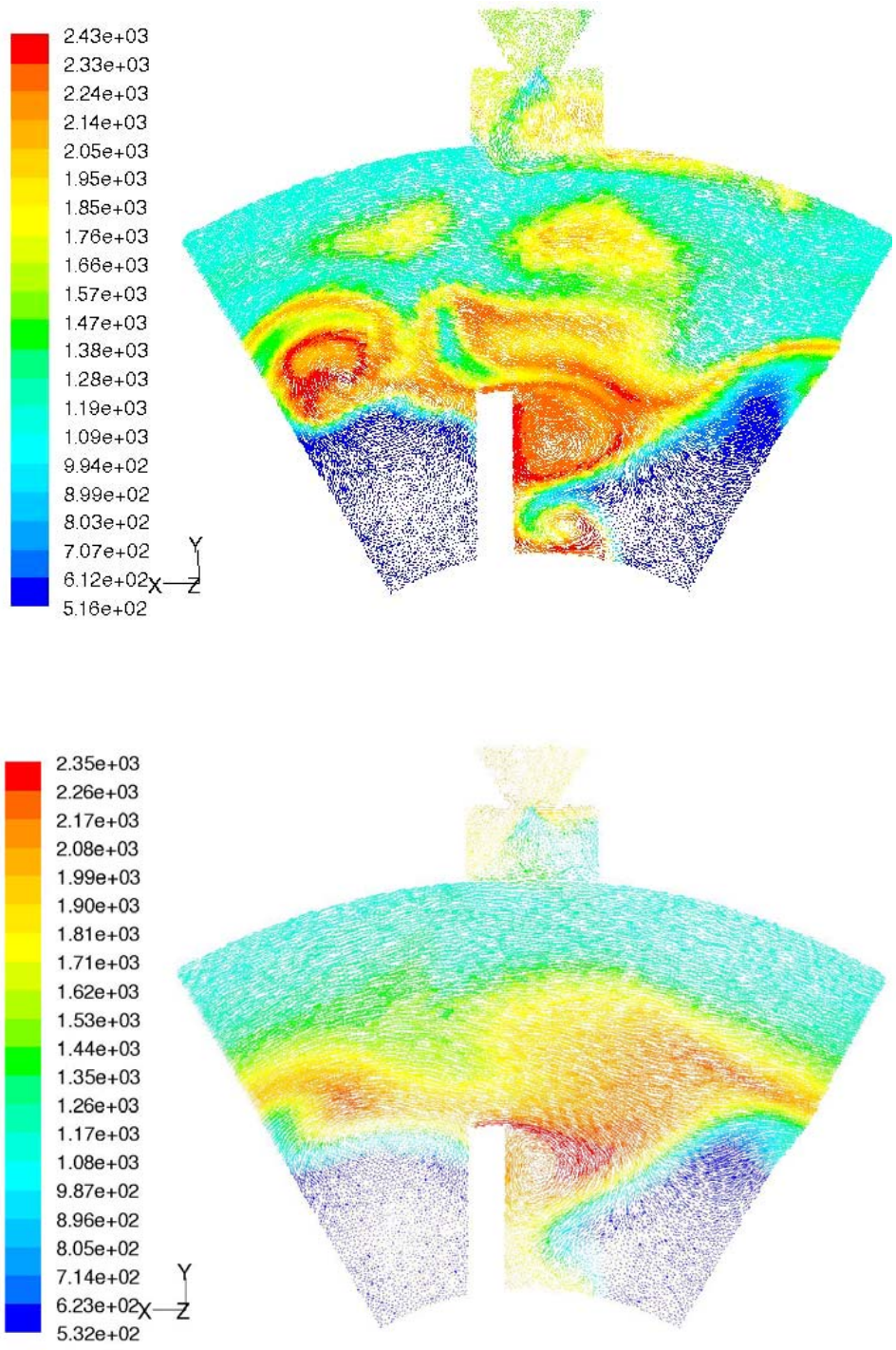

Figure 22: Cavity fuel plane velocity vectors colored by temperature (K) for experimental configuration, LMLP, RNG k-ε model (top) and standard k-ε (bottom), viewed from exhaust with swirl clockwise.

are evident in both models on this plane, at the same locations previously noted. However, the RNG *k*-*ε* model clearly has a much more developed vortex structure. Also evident on this cavity fuel plane view is the main flow entrainment into the cavity from the second vortex, in the area approaching the right periodic boundary and continuing into the vortex once through the periodic boundary.

Next, Figure 23 depicts the tangential velocity contours on the U_θ plane, to visualize the data from Table 6, again for both turbulence models. Both cutaways show similar overall velocity variations, the RNG *k*-*ε* model's contours provide more detail, especially in the high velocity spots where the air inlet jet flow is evident on this plane. From investigation of the air inlet axial planes, it was also found the RNG *k*-*ε* model had more gradual dissipation of the air inlet jets.

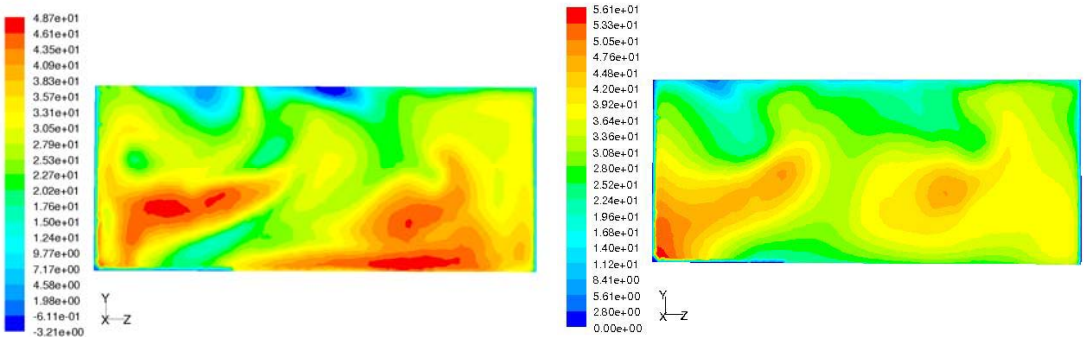

Figure 23: Tangential velocity (m/s) contours on U_θ plane, experimental configuration, LMLP, RNG *k*-*ε* (left) and standard *k*-*ε* (right) turbulence models. Cavity flow is out of page.

Observing the tangential velocity variations across the cavity cross section, a further investigation into this important parameter relating to centrifugal force combustion is needed. Therefore, radial-averaged tangential velocities were computed in

FLUENT post-processing for 50 bands over the U_θ plane, then the g-loadings at the corresponding radii were computed using Equation 42, with the results plotted in Figures 24 and 25 for all experimental configuration operating conditions.

These plots give a different perspective to the dynamics of the cavity flow. Using only the mass weighted average for the entire U_θ plane results in an optimistic appraisal of the cavity g-loading as a whole, whereas this method of evaluating the data shows a broad range of g-loads occurs, somewhat smoothly spread to increase inward. It is observed the tangential velocity and g-load peaks near the inner radius correspond with the radius where the air inlet extended jet flow intersects the U_θ plane, with a pocket of cold, low mixture fraction air. It is also observed the profile for the standard *k-ε* turbulence model has a broader curvature at this point, indicative of the greater diffusion rate of the inlet jet into the cavity flow. It also has slightly higher tangential velocity across the cavity radius, except for near the axial vane RVC where this turbulence model suffers in simulating the swirling vortex produced at this flow interaction area. The second, smaller peak on the RNG *k-ε* model conditions at the lowest radius corresponds to a tangential acceleration imparted by the RVC vortex, then the decelerating tail at the bottom of the curve is the rapid downward turn of the flow into the swirling vortex, as the U_θ plane's lower boundary borders the RVC.

Finally, Figure 26 gives a view on the axial cavity-vane plane of the interaction between the cavity and main flow into the RVC. This perspective, with velocity vectors colored with temperature contours, clearly illustrates the desired mass transport effect of the RVC on the hot combustion products from the cavity, filling the RVC. This view

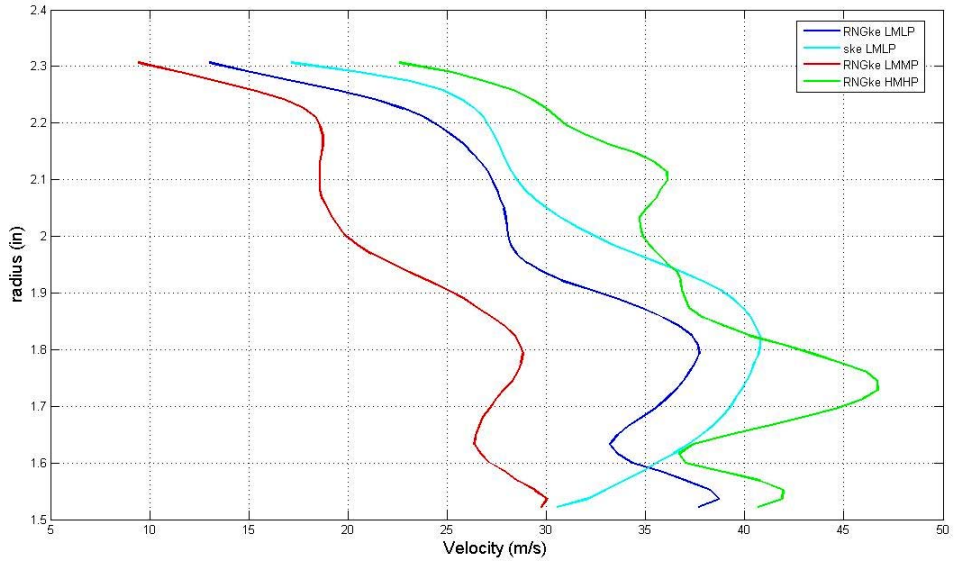

Figure 24: Circumferential averaged tangential velocities plotted by radius on U_θ plane for experimental configuration.

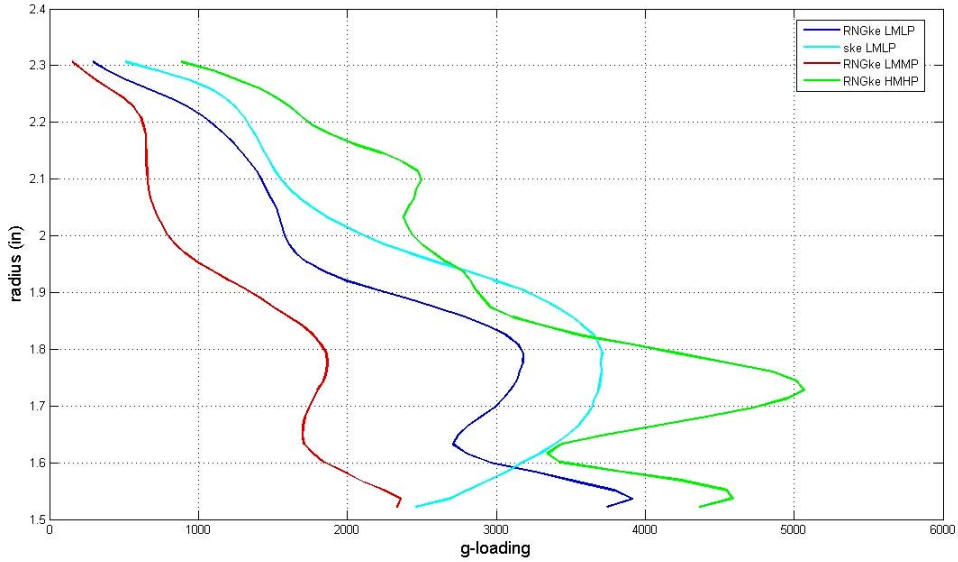

Figure 25: Circumferential averaged g-loading plotted by radius on U_θ plane for experimental configuration.

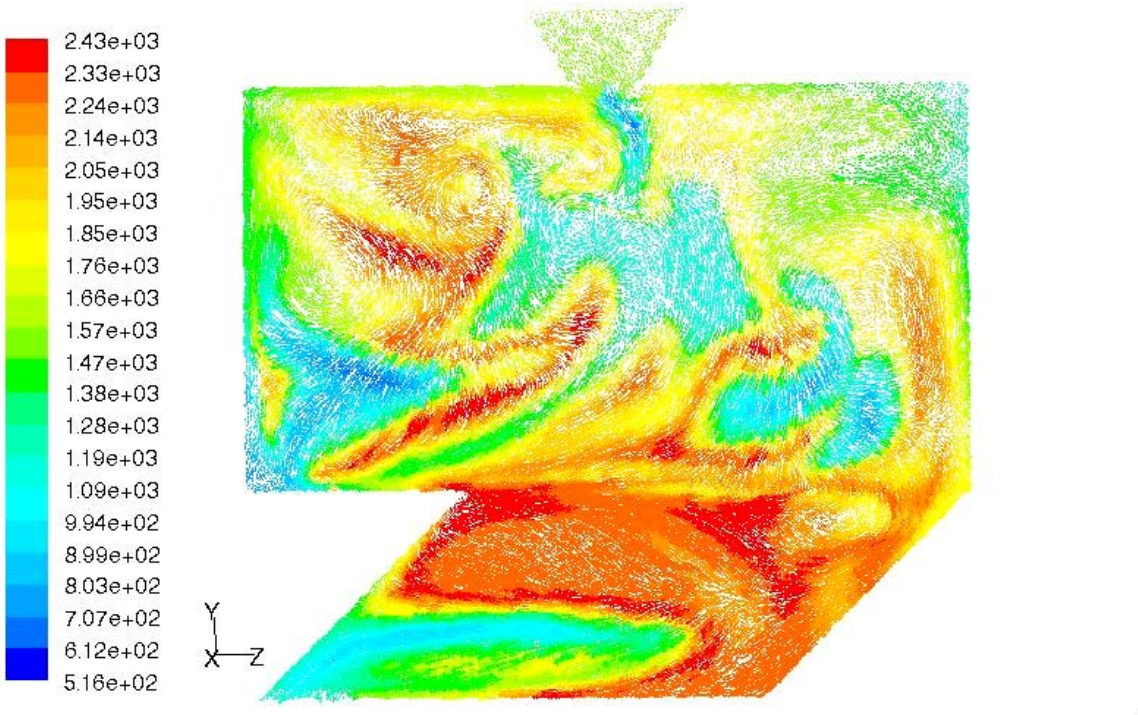

Figure 26: Velocity vectors colored by temperature (K) for cavity-vane plane on experimental configuration, LMLP, RNG *k-ε* model. Cavity flow (upper half) is out of page, main flow across RVC (lower half) is right to left.

also provides further evidence of the buoyancy and turbulent mixing effects, as cold areas of flow emanating from the cavity air inlet jets are seen to interact and mix with the hotter areas of the flow. Also found on this cavity-vane plane cutaway, using zooming to focus on specific areas, is a very weak trapped vortex (TV) flow around the outer areas of circumference of the cavity. The TV effect is very weak and intermittent, as the cavity flow is dominated by the high velocity air jets producing the tangential velocity to swirl the flow outward in this view.

4.1.4 Exhaust Temperature Distribution Evaluation. Examining the critical combustor design requirement of exhaust temperature distribution will also provide insight into the performance of the configuration and the CFD model. Table 7 presents

the temperature profile data for the outlet plane, where T_4 is the mass weighted average of the outlet plane, and T_{mr} is the maximum circumferential radial average temperature, computed using 100 radial bands in *FLUENT* post-processing. Pattern and profile factor are calculated using Equations 40 and 41. The data does not initially provide a positive trend for the new model, as the pattern and profile factors are equivalent or worse than the coarse grid data. But, pattern and profile factor are based on measures of the maximum temperature, and do not quantify where it occurs. Therefore, further evaluation examining the full outlet temperature profile will provide a better analysis of the performance of the combustor and the model.

Table 7: Exhaust temperature pattern and profile factor data for experimental configuration.

Op Cond	Model	T_{4avg} (K)	T_{mr} (K)	Pattern Factor	Profile Factor
LMLP	Expr	1254			
	3-D Coarse	1152.71	1687.40	1.930	0.859
	3-D Expr sk-ε	1166.53	1628.78	1.871	0.728
	3-D Expr RNGk-ε	1178.67	1813.26	1.889	0.981
LMMP	Expr	1256			
	3-D Coarse	1167.136	1705.90	1.902	0.859
	3-D Expr RNGk-ε	1112.75	1865.88	2.286	1.317
HMHP	Expr	931			
	3-D Coarse	871.46	1191.30	1.932	0.995
	3-D Expr RNGk-ε	869.03	1183.20	2.221	0.993

Figure 27 compares the outlet plane temperature contours for the two turbulence models on the LMLP condition. Here the two turbulence models provide significantly different results. The RNG *k-ε* turbulence model depicts the several areas of hotter gases, with the largest and hottest centered at approximately the two-thirds radius point and located near the center of the inter-vane passage. A second one is on the outer wall border, indicating flow emanating from the RVC, and this area is also affected by heat

transfer from the wall. Temperature details are consistent with mixing in a vortex structure. The standard *k-ε* model depicts a single hot area extending downward from the outer wall on the RVC side of the axial vane, also corresponding to the observed main channel flow, and bounded on the centerline by the axial vane. This temperature profile is in agreement with the previous observations for this configuration of the standard *k-ε* turbulence model, showing rapid dissipation of the turbulent intensity and vortex structures, resulting in less effective mixing.

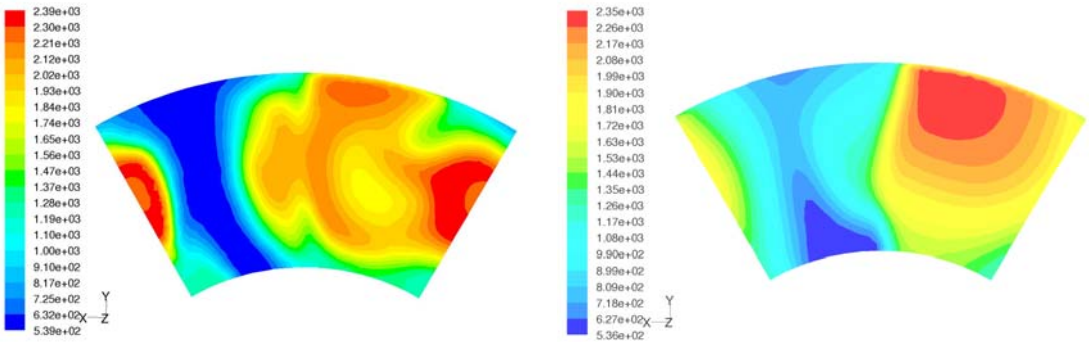

Figure 27: Temperature (K) contours for outlet plane on experimental configuration, LMLP, RNG k-ε (left) and standard k-ε (right) turbulence models. Outlet plane viewed from behind combustor, cavity swirl is clockwise.

Figure 28 quantifies the outlet temperature contour information by plotting the circumferential radial averaged temperature by normalized radius for the outlet plane, for each operating condition, turbulence model. All cases indicate the peak of the radial averaged profile near the two-thirds radius, where peaking above the mid-height is desirable in modern gas-turbine engines (Lefebvre, 1983:142). Of note is the very smooth profile for the standard *k-ε* LMLP case, again indicating dissipation and

dispersion of the turbulence effects and temperature mixing, and contains the highest temperature of these cases at the upper radius of the outlet plane.

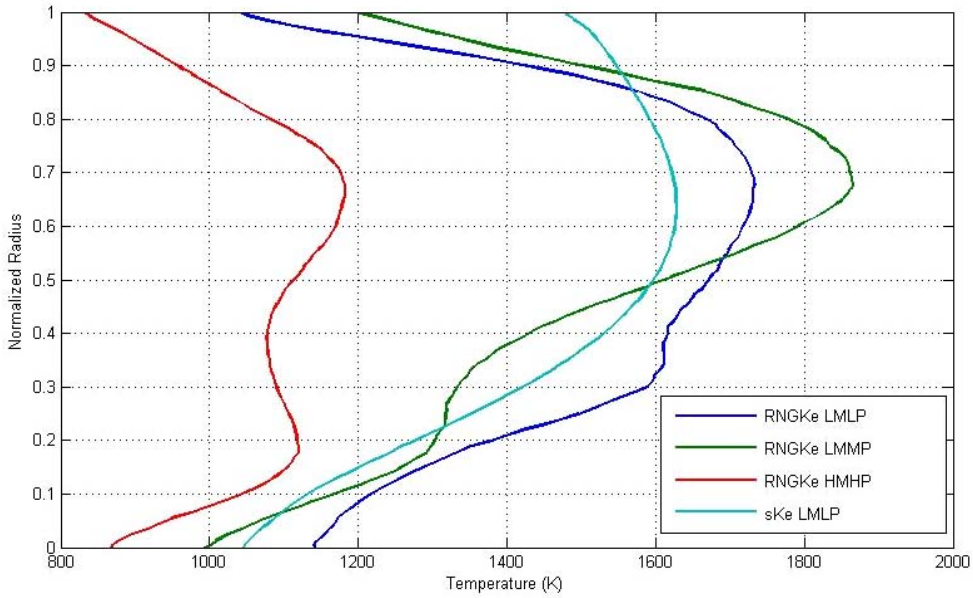

Figure 28: Circumferential averaged temperature plotted by normalized radius for outlet plane of experimental configuration.

The RNG *k-ε* model profiles display steeper profiles to the peaks, temperature variations in localized radii, and reduced temperatures at both the upper and lower radii limits. Additionally, the HMHP condition produces significantly lower outlet plane temperatures, as a result of the previously observed lean cavity mixture producing less overall energy, but more complete combustion for a higher efficiency.

4.1.5 Standard k-ε and RNG k-ε Model Comparison. In evaluating the RNG *k-ε* model LMLP condition solution at intervals over the course of extended iterations to a 15,000 iteration total, it was observed to be somewhat unstable. Or, a more accurate

statement would be, it was incapable of approaching what is typically considered a converged solution, instead proceeding in more of a transient manner over the course of successive iterations. The inherent complexities of the UCC flow and the RNG k-ε turbulence modeling sensitivity resulted in orders of magnitude higher residuals for the continuity, turbulence kinetic energy dissipation rate, and energy equations. Also, larger scale periods of minor increase in the solution residual levels were encountered, over what was observed for the standard k-ε model. Further, in evaluating all performance measures at each thousand iteration mark from 9,000 to 15,000 iterations for the RNG K-ε model, the solutions viewed together resembled more of an unsteady, time accurate series portrayal of the UCC, as the flow solution had large variations in some performance measures and visualized flow characteristics. The most significant variation occurred in CO emissions, with up to three times greater than the mean level at two points, with the resultant decrease in combustion efficiency. The cavity temperature profiles depicting the buoyancy pockets changed each interval, and main channel flow and outlet plane temperature profiles showed variances in the vortex shape and placement extending down the combustor exhaust.

It is recognized with the preceding evaluation comparing both turbulence models for the experimental configuration, while the standard k-ε turbulence model can produce equivalent quantitative performance marks and is better suited to a steady state solution, the increased detail in the micro-scale flow characteristics of the RNG k-ε turbulence model is desired to more accurately model the flow for the future experimental testing. Therefore, the RNG k-ε turbulence model was chosen to use in the remainder of this

study to provide accurate, detailed flow predictions, and is also recommended for use in developing an unsteady, time accurate solution for the UCC. Because of the inherent transient nature and fluctuations in the solution and performance measures at varying iteration intervals, reflecting the true nature of a turbulent flow, each 'solution' evaluated is considered a momentary state of the flow in its unsteady fluctuations.

4.1.6 Dense Grid Effects. To complete the evaluation of how the improved grid affected the solution for the model, a look at the coarse grid flow visualization and outlet temperature distribution is required. Figures 29 and 30 display the cavity fuel plane, velocity vectors with temperature, and outlet plane, temperature contours, for the coarse grid, LMLP condition, standard k-ε turbulence model from Anisko's research. These can be compared with Figures 22 and 27, respectively, from the dense grid solutions. The cavity fuel plane temperature profile is not as stratified as in the dense model, with the hot area extending to a greater radius. Further, the lack of detail from the large cavity cell size is evident in both the temperature contours and the velocity vectors, though the characteristic swirl into the RVC is evident. The half vane plane cutaways (not shown) for temperature, velocity, and turbulence intensity are similar in to the standard k-ε dense grid. The outlet plane temperature contours display the same pattern as the dense standard k-ε model, except the hot area pattern is closer to the outer wall and the cross section is not as wide.

Reviewing the radial average outlet temperature profile plot for the coarse grid LMLP condition in Figure 31 shows a profile where the average merely increases with

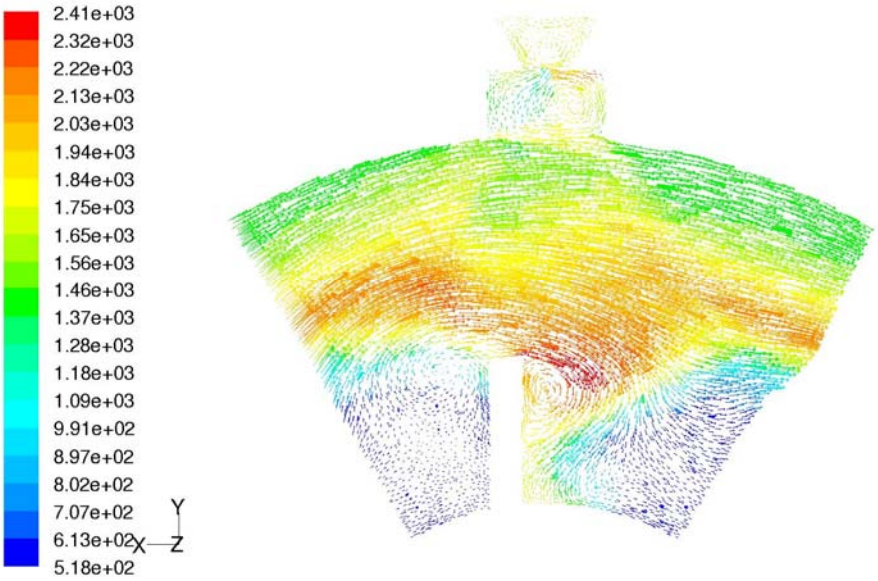

Figure 29: Velocity vectors colored by temperature (K) on fuel plane for experimental configuration, LMLP, coarse grid and model, adapted from Anisko's research with permission. Viewed from combustor exhaust, cavity swirl is clockwise.

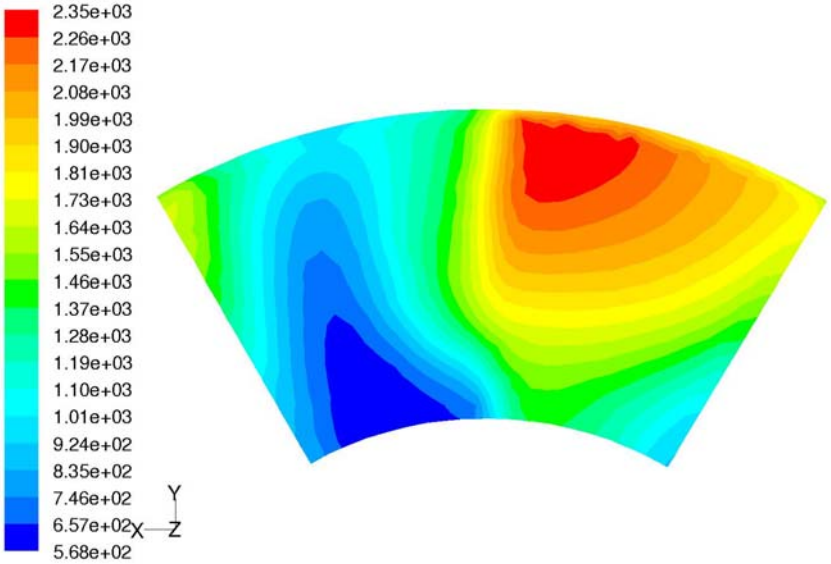

Figure 30: Temperature (K) contours for outlet plane on experimental configuration, LMLP, coarse grid and model, adapted from Anisko's research with permission. Viewed from rear of combustor, swirl is clockwise.

radius, until the maximum temperature is reached at the maximum radius coincident with the combustor outer wall. This is significantly different than the RNG *k-ε* profile with a sharp peak at two-thirds normalized radius, and several variances, and the standard *k-ε* where the profile is smooth, but the maximum temperature peak still occurs at approximately two-thirds the radius.

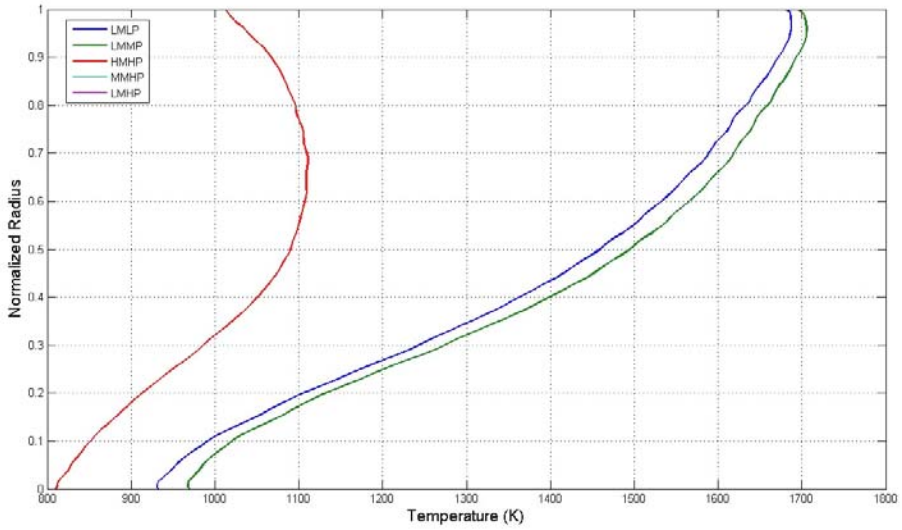

Figure 31: Circumferential radial averages of temperature plotted by normalized radius for outlet plane of experimental configuration, LMLP condition, coarse grid and model, adapted from Anisko's research with permission.

This comparison with the coarse grid concludes with the finding that the new dense grid significantly improves the detail and accuracy of the solution, as first evidenced by the increased resolution and evidence of buoyancy effects on the temperature and velocity gradients examined on the cavity fuel plane. Secondly, the stark difference revealed by the outlet temperature profile plots suggests the coarse grid is

not effective in transporting the species or modeling the turbulent mixing sufficiently enough in the large cells to move the hot combustion products down significantly from the outer wall into the center of the main flow channel to the exhaust outlet plane. Of course, these findings are not surprising, given the known complexity of the turbulent flow and the inherently short length scales used to measure and quantify, providing example of the principle of grid construction of such density to meet the desired flow accuracy.

4.1.7 Validity of Improved CFD Model. This evaluation of the improved CFD modeling of the UCC problem on the experimental configuration demonstrates greater agreement of performance data related to experimental results, and much improved resolution of the flow characteristics and details, especially with the RNG k-ε turbulence modeling. While further enhancements can likely be made to further improve the solution, it is determined the dense grid and CFD modeling with the RNG k-ε turbulence modeling, non-equilibrium wall functions, and reduced fuel droplet diameter provides a tool of sufficient accuracy to model and evaluate configuration designs and ultimately provide predictions of detail and data for a baseline to facilitate the experimental testing and understanding of the cavity-vane interactions of the UCC.

4.2 3-D Short Baseline Axi-symmetric Model

The second step of the design process is to apply the now established CFD model to the 3-D baseline configuration for numerical solution. The baseline configuration solutions are evaluated in comparison with the experimental configuration for validation before proceeding on the design process. The 3-D baseline configuration, shortening the

cavity axial length to 1.5 inches (38.1 mm) and adjusting the cavity air inlets to 45^o from radial, was simulated on the LMLP, LMMP, and HMHP conditions for comparison with the 3-D experimental configuration. Further tests at atmospheric conditions, ATM1 and ATM2, are also simulated and evaluated for use as baseline comparison cases for the atmospheric sector rigs. The solutions were evaluated at 13,000 iterations for the LMLP and LMMP conditions, 11,000 iterations for the remainder of the conditions.

4.2.1 Performance and Emissions Data Evaluation. Table 8 displays the emissions and performance data for the 3-D baseline configuration in comparison with the 3-D experimental configuration. The LMLP and LMMP cases are evaluated at 13,000 iterations, while the remainder is evaluated at 11,000 iterations. Therefore, as previously discussed regarding convergence and solution acceptability with the experimental configuration, the solution and data for each case is considered a momentary point in the overall unsteady, fluctuating solution.

Table 8: Emissions and efficiency performance data for 3-D Baseline Configuration (1.5 inch cavity, 45^o inlets) compared with 3-D Experimental Configuration.

Op Cond	Model	CO(ppm)	CO_2 (%)	O_2 (%)	NO_x (ppm)	UHC (ppm)	η_b (%)	dP/P (%)
LMLP	3-D Expr.	1511.64	3.86	14.73	25.40	30.90	97.33	4.05
	3-D Baseline	2861.84	3.72	14.82	27.92	15.87	96.22	4.57
LMMP	3-D Expr.	2330.65	3.37	15.42	50.87	5.67	97.13	2.50
	3-D Baseline	2040.90	3.31	15.55	43.48	1.29	97.60	2.23
HMHP	3-D Expr.	147.98	1.84	18.08	26.31	2.88	99.50	5.96
	3-D Baseline	166.61	1.84	18.08	20.27	0.05	99.62	6.09
ATM1	3-D Baseline	1498.03	3.28	15.66	6.85	19.06	97.71	7.86
ATM2	3-D Baseline	2793.39	3.29	15.50	9.45	13.12	94.49	4.35

The only trend evident in the emissions and performance data comparison with the experimental model is a decrease in the UHC emissions. This increase in the fuel

droplet evaporation from the experimental configuration was found to be attributable to both the reduced cavity length, in bringing the inlet jet flow closer to the fuel injection axial position, and cavity inlet angle change increasing the tangential velocity in the cavity, to cause the larger fuel droplets injected in the 'upwind' portion of the spray cone to either be captured into the cavity flow or impact the axial vane and evaporate. In the experimental configuration, these 'upwind' larger droplets had descended into the cooler main flow and escaped largely un-evaporated. The small amount of un-evaporated fuel droplets now escaping originate on the aft portion of the injection cone, fall into the hot portion of the main flow, and continue to evaporate as they follow the outer areas of the hot mixing zone in the main channel flow.

Overall, the combustor efficiency and pressure loss data for the three experimental data conditions do not indicate any significant issues with the baseline configuration. The two atmospheric pressure conditions indicate encouraging results considering the decreased fuel evaporation rate accompanying the reduction in operating pressure and mass flow. The high pressure loss figure for the ATM1 condition is attributed to high loading and velocities resulting in increased cold losses in the form of drag.

4.2.2 Overall Solution Visualization. A visual overview of the 3-D baseline configuration solution, LMLP condition, indicates the macro-scale characteristics of the UCC flow remain essentially unchanged for this configuration. Figure 32 displays the temperature contour overview, where the two vortex structures of the cavity to main flow interaction are visible, including the same area of hot burning gases on the upwind side of

the axial vane (not visible on figure, behind the vane). The shorter cavity, in this snapshot solution, indicates a different pattern of temperature areas in the cavity, including a large area of cooler burning in the central radius area. Evident on the outflow plane, bottom right corner, is a cold spot resulting from an area of reversed flow across the pressure outlet boundary, indicative of a low pressure center of a swirling vortex. The pressure outlet backflow was modeled as 300 K, 3 % turbulent intensity, length scale based on hydraulic diameter to simulate ambient laboratory conditions.

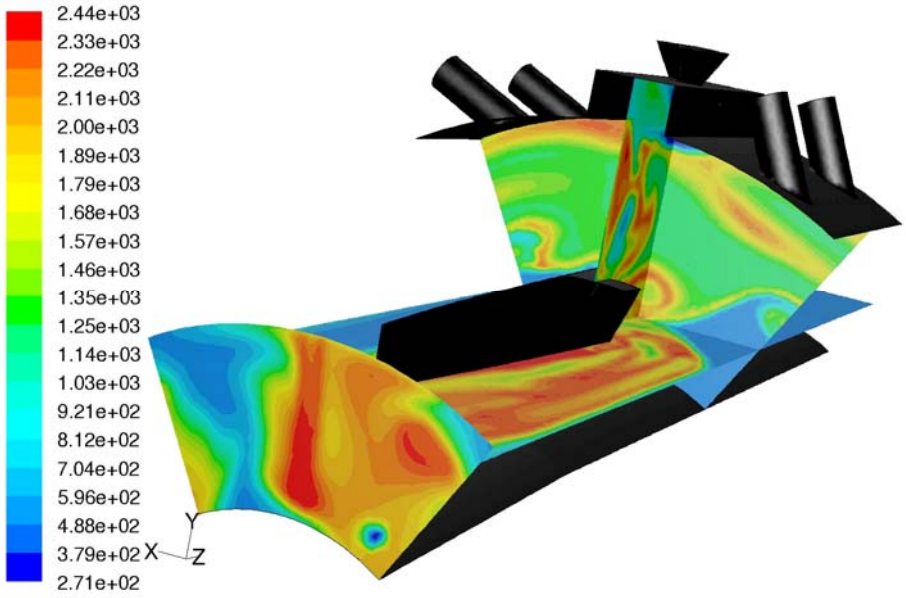

Figure 32: Contours of temperature (K) for the 3-D baseline configuration, LMLP condition, viewed from exhaust outlet, main mass flow right to left, out of page.

Figures 33 and 34 display the overviews for contours of velocity magnitude and turbulent intensity, with small variations from the experimental configuration solution cutaways in most areas, attributable to the turbulence permutations, except at the exhaust

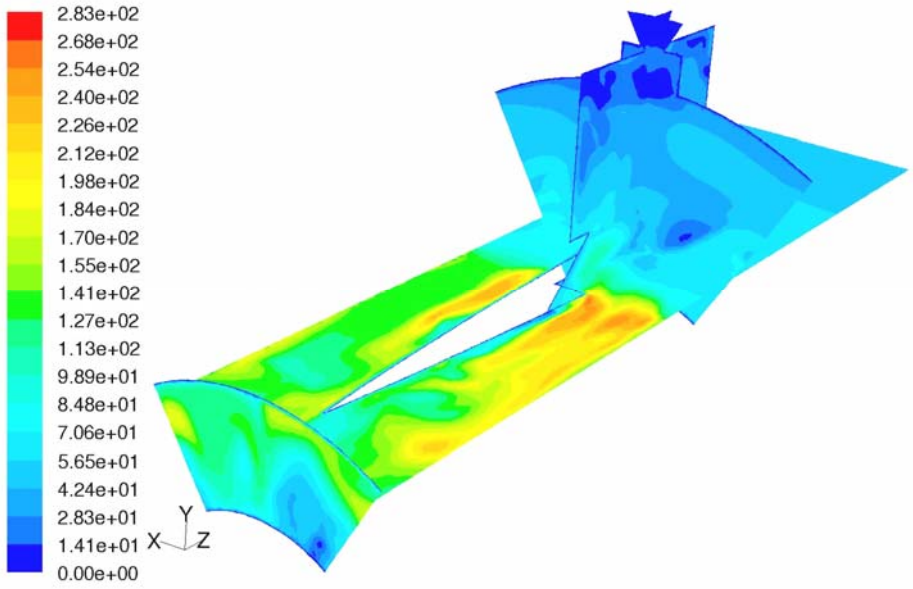

Figure 33: Contours of velocity magnitude (m/s) on 3-D baseline configuration, LMLP condition.

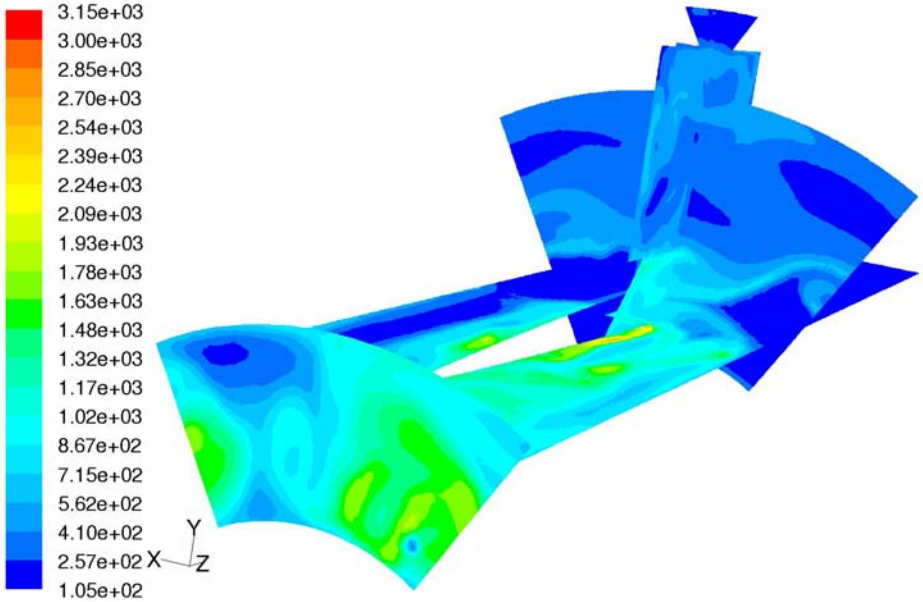

Figure 34: Contours of turbulence intensity (%, read as e+01) on 3-D baseline configuration, LMLP condition.

area just after the cavity interaction, where the velocity and intensity are slightly higher for the 3-D baseline configuration. This is due to the decreased cavity volume exhausting the same mass flow into the main channel flow, resulting in further localized turbulence increases.

The two remaining experimental operating condition and the two atmospheric operating condition cases also display the established macro characteristics of the flow. The HMHP condition on the baseline configuration contains more residual burning in the dilution zone of the main channel flow than the experimental configuration did, indicating a decrease in the completeness of combustion in the cavity. The atmospheric condition cases exhibit slightly less turbulence intensity in the high turbulence area just after the cavity interaction, with the ATM2 condition more significantly so. Select flow visualization cutaways for the ATM2 condition are contained in Appendix A.

4.2.3 Cavity Flow, G-loading, and Cavity-vane Interaction Evaluation. To focus again on the area of interest for this research, the analysis and evaluation of the cavity flow and cavity-vane interaction for this configuration is of importance in the next design steps. Table 9 provides the flow parameters for the 3-D baseline configuration. The expected increases in cavity cross-section plane mass flow and average tangential velocities are evident, due to both the decreased volume and cross-sectional area for the same mass flow and to the air inlet angle change to increase the average tangential velocity component. The entrained mass flow for the LMLP and LMMP cases increased to approximately 3.5 times the injected air mass, with approximately 20% - 30% tangential velocity increase. Interestingly, the one exception to this is the HMHP

condition where the cavity cross-section plane mass flow actually decreased slightly, but still with a 25% increase in average tangential velocity. This will be examined further once the entire cavity flow profile is evaluated.

Table 9: Cavity flow parameters for 3-D baseline configuration with mass weighted average velocities for U_θ plane.

Op Cond	Model	CLP	$\dot{m}_{cav}$ $\frac{lbm}{\min}$ $\left(\frac{kg}{\min}\right)$	$\dot{m}_{cavplane}$ $\frac{lbm}{\min}\left(\frac{kg}{\min}\right)$	U_θ (m/s)	U_r (m/s)
LMLP	3-D Expr.	0.296	1.072 (0.486)	2.601 (1.180)	34.62	-7.62
	3-D Baseline	0.366	1.072 (0.486)	3.549 (1.610)	40.40	-7.75
LMMP	3-D Expr.	0.206	1.032 (0.468)	2.323 (1.054)	26.43	-5.63
	3-D Baseline	0.259	1.032 (0.468)	3.691 (1.674)	34.01	-6.37
HMHP	3-D Expr.	0.281	2.120 (0.962)	6.631 (3.008)	46.39	-9.37
	3-D Baseline	0.351	2.120 (0.962)	5.949 (2.698)	60.76	-9.42
ATM1	3-D Baseline	1.081	0.536 (0.243)	1.883 (0.854)	58.67	-8.44
ATM2	3-D Baseline	0.924	0.429 (0.195)	1.780 (0.807)	48.71	-5.30

The atmospheric pressure conditions exhibit behavior consistent with their higher CLP and similar to the HMHP condition, in that the cavity averaged tangential velocity is higher and mass flow entrainment is at approximately three times the air mass injection rate. ATM2 appears to be suitable for experimental testing based on its predicted cavity tangential velocity.

The cavity-fuel plane cutaway for the 3-D baseline configuration LMLP condition, as shown in Figure 35, shows a different formation of hotter and cooler gas pockets interacting in the cavity. As seen in the flow overview, the two swirling vortex structures pulling the cavity flow down into the RVC and the main channel flow are clear and well developed, interchanging the passing mass in the inner cavity radius regardless of its temperature. It is also interesting to note a hot region is present encompassing the outer radius of the cavity in this specific flow fluctuation. This band, as will be seen

next, is in an area of slower velocity and g-loading, so the buoyancy effects are decreased, slowing the mixing, but not stopping it, as the area to the upper right contains a cold bubble nearly surrounded by hotter gas. Additionally, axial flow through the CIAC introduces colder air into the outer circumference.

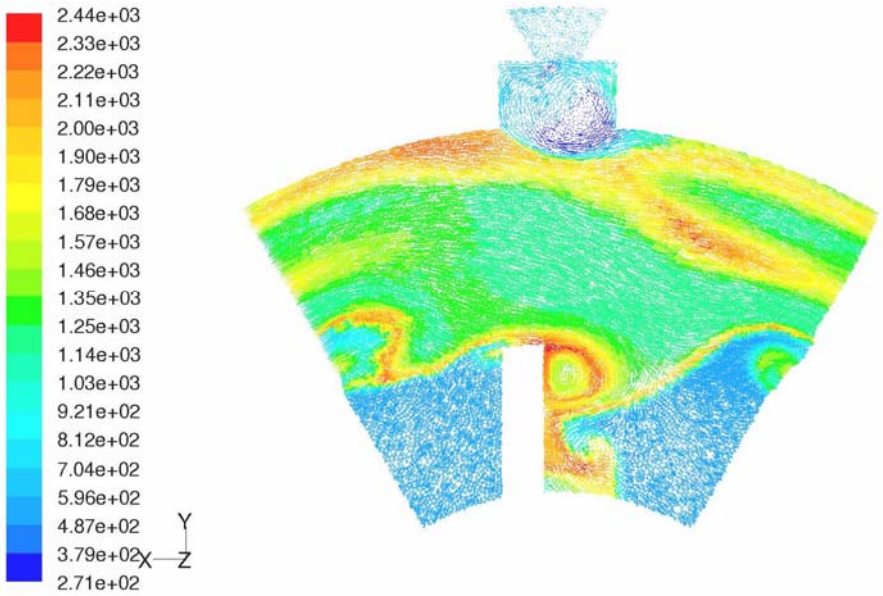

Figure 35: Cavity fuel plane velocity vectors colored by temperature (K) for 3-D baseline configuration, LMLP condition, viewed from exhaust with swirl clockwise.

To further analyze the LMLP cavity flow, Figure 36 displays the cutaways of velocity vectors with temperature for the axial planes coincident with the forward and aft cavity air inlets, to depict the air inlet interaction with the cavity flow and the differences in the temperature gradients across the axial length of the cavity. The first point to note is the fact the cavity air inlet jets extend to at least the cavity cross-section plane over the axial vane and on the CIAC centerline, transporting colder, zero mixture fraction air to

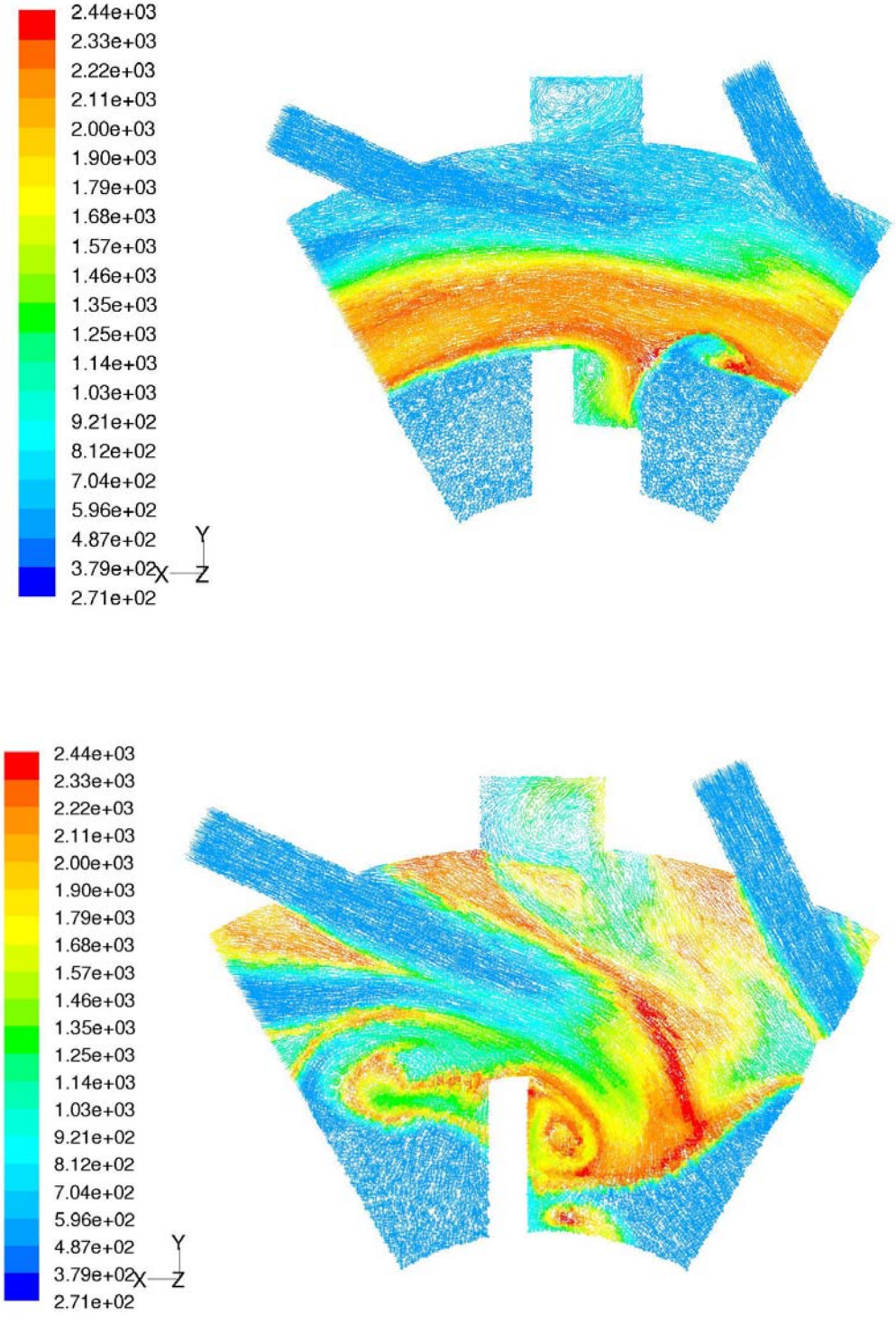

Figure 36: Cavity plane velocity vectors colored by temperature (K) for axial planes coincident with forward cavity air inlets (top) and aft cavity air inlets (bottom) for 3-D baseline configuration, LMLP condition, viewed from exhaust with swirl clockwise.

inner radii. With the cavity angle increased from 37^{o} from the radial to 45^{o} for the baseline configuration, it was observed the area of impingement onto the cavity cross-section plane is of slightly greater radius here.

On the forward plane, the clearly stratified temperature envelope conforms to the centrifugal-force effects theory for buoyancy effects, but its presence is also partly due to the trapped vortex concept. The forward face of the cavity experiences the downward flow of the weakly present TV as the main flow crossing below provides a low pressure suction effect. Also, this position forward of the fuel injection does not provide any combustible matter in the outer cavity radii, only the cold air diffused from the air inlets. Only at lower radii has the fuel spray spread and evaporated to extend to this plane, hence the lower radius where combustion is occurring. Additionally on the forward cavity plane, the beginnings of the RVC generated vortex structure can seen, while the second vortex structure in mid-main channel has not developed yet.

For the aft plane, there is dynamic mixing of hot and cold gases due to the influence of the cavity air inlet jets. The large hot area in the right mid-radius area is moving downward, pulled by the now larger RVC vortex and the now accelerating main channel flow, transferring hot gases down into the main flow. This is countered on the left side (as shown) of the axial vane where the second vortex structure is pulling large amounts of cold main channel flow air up into the cavity with its outer layers, and the inner layer has entrained some hot gases, which can be seen being pulled toward the surface of the axial vane, corresponding to the area aft of the max vane thickness where flow acceleration is occurring. The hot combustion areas along the outer radius around

the cavity air inlets are from the combustion centered on the fuel spray moving aft in the cavity at the lower velocities present at the outward radii. These pockets, on this aft plane cutaway, are noted to have velocity vectors pointing downward, pulled by the inlet jets. These hot areas along the cavity walls are the source of the difficulties in achieving an appropriate cell size and y* value for the wall function near wall treatment in the cavity.

General behavior of this nature was observed with all experimental and atmospheric cases, with the cavity fuel plane providing differing temperature and velocity patterns due to its relative independence of the cavity air inlets and dependence on the combustion reaction, buoyancy effects, and turbulent mixing.

Figures 37 and 38 display cavity U_θ plane circumferentially averaged tangential velocities and calculated g-loadings plotted by radius. Compared with the experimental configuration plots from Figures 24 and 25, the curves for both are now smooth, shifted to a higher velocity range, and lack the pronounced inlet jet peak. This is due to the overall cavity velocity increase from the axial length reduction coupled with constant mass flow, such that the flow surrounding the extend inlet jets is closer to the jets velocity. The LMMP and ATM1 conditions show slight bulges, at a higher radius than previously, where the jet meets this plane. Of course, with the increased tangential velocities comes increased g-loading, and with the highest velocities at the shortest radii, very high g-loads are produced on the HMHP, ATM1, and ATM2 conditions just above the axial vane.

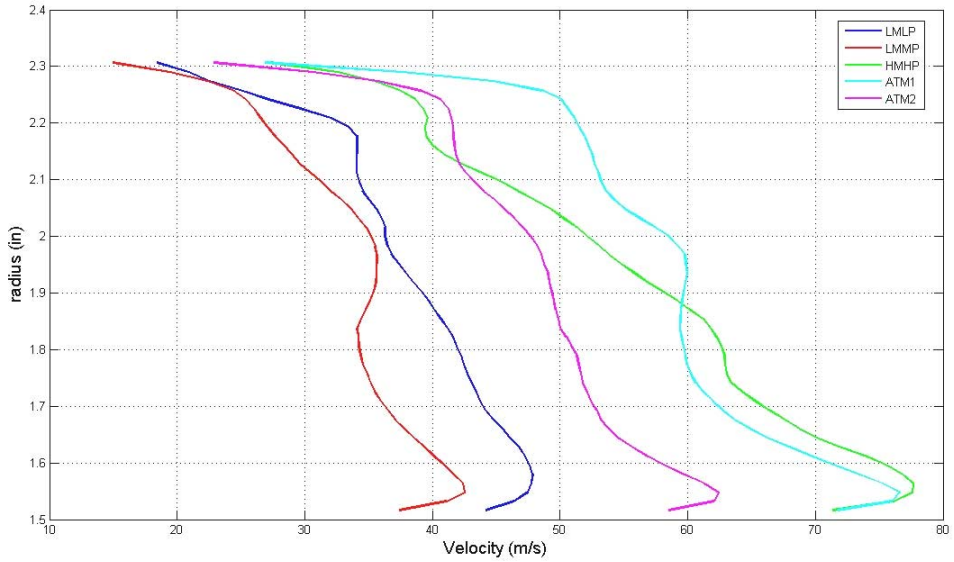

Figure 37: Circumferential averaged tangential velocities plotted by radius on U_θ plane for baseline configuration.

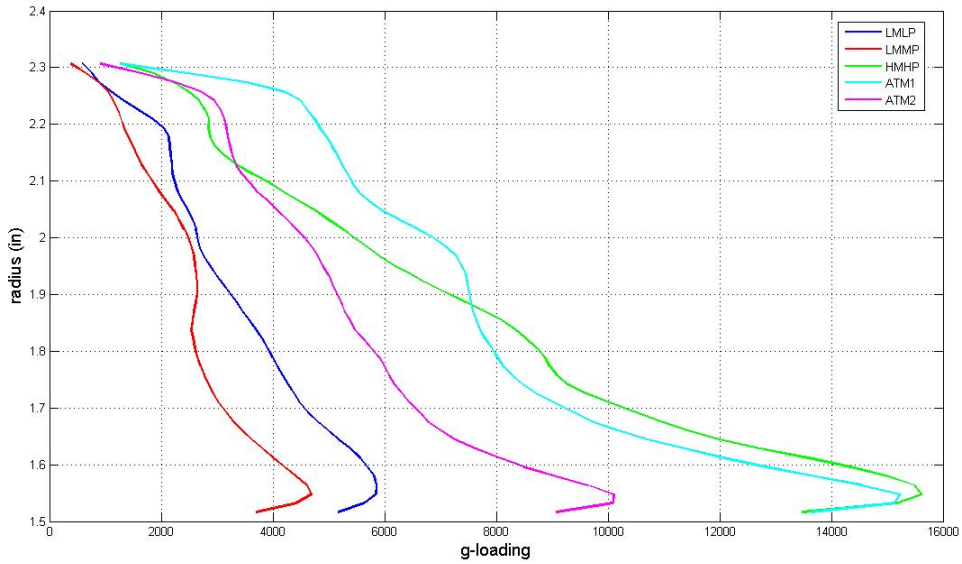

Figure 38: Circumferential averaged g-loading plotted by radius on U_θ plane for 3-D baseline configuration.

Figure 39 now gives a cross-sectional view of the cavity flow on the cavity-vane plane, displaying velocity vectors with temperature, confirming the axial cavity fuel and air inlet plane analysis. Note the forward (right as shown) cavity air inlet jet intersects this plane at a higher radius than the aft inlet jet. Also, when combined with the axial plane cutaways, 3-D temperature bubbles are varying in the axial direction are evident. Unfortunately, when compared with the 3-D experimental configuration cavity-vane plane, Figure 26, a definitive conclusion on the effects of the shortened cavity is difficult. While the shortened cavity length compresses the flow combustion patterns closer together, the shortened cavity flow state as shown does not contain any hot gases in the CIAC, where there was some burning occurring on the longer cavity. Also there is an area of burning along the aft wall (left side, as shown), in a localized swirling flow, where this swirling feature was evident in the longer cavity, but more separated from wall and swirling mixed hot and cold gases, for that flow state. In both instances, excellent transport of hot combustion products into the RVC is noted, with the shorter cavity appearing to have a slightly cooler profile on this plane.

Now, to return to the question of the HMHP cavity cross-sectional plane mass flow decrease, Figure 40 depicts its cavity fuel and cavity-vane planes with velocity vectors colored for temperature to provide a final piece of information regarding its behavior. The large hot combusting areas in the CIAC and fuel injection housing cone are in an area of slow velocity, but included in the plane to measure the cavity plane mass flow rate, so their low density and slow velocity decreases the mass flow across the

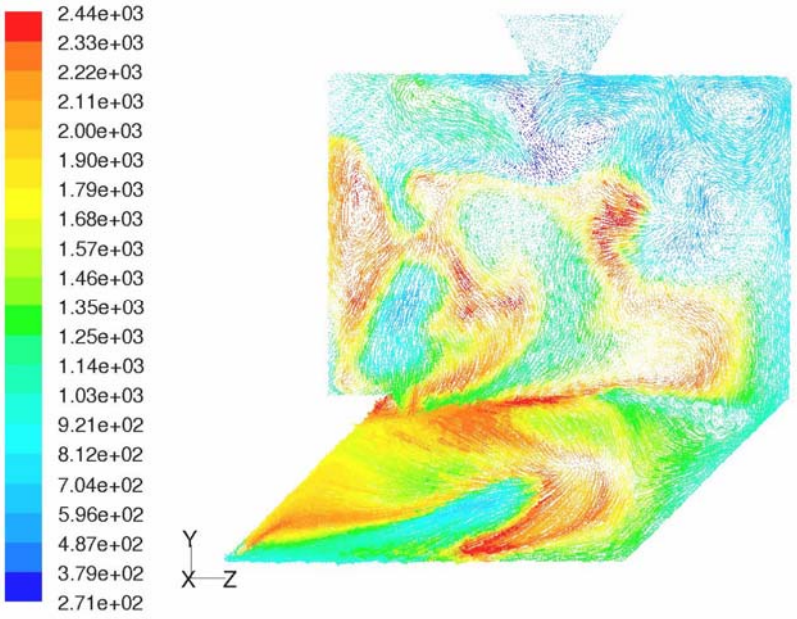

Figure 39: Velocity vectors colored by temperature (K) for cavity-vane plane on 3-D baseline configuration, LMLP condition.

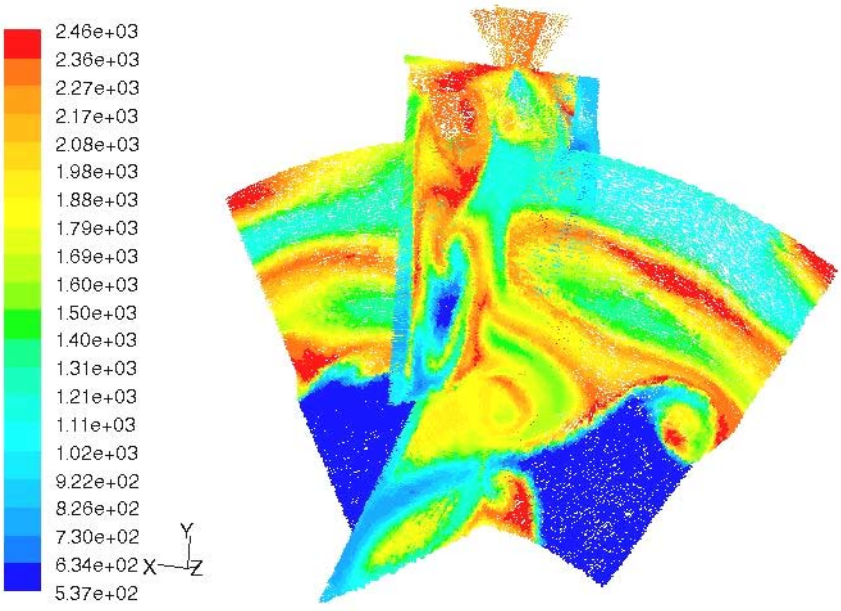

Figure 40: 3-D baseline configuration, HMHP condition, cavity fuel and cavity-vane planes velocity vectors with temperature (K). Flow swirls from clockwise on cavity fuel plane.

plane. However, this cannot be the sole explanation for a 0.7 lb/min mass flow rate decrease as compared with the longer cavity configuration.

Note the large hot area surrounding a colder area on the right half of the cavity fuel plane. This pocket encloses the colder area while crossing the periodic boundary, then opens again at the end approaching the centerline (behind cavity-vane plane). Another large cold bubble is evident in the center of the cavity-vane plane and extending along the outer radius of the cavity fuel plane. These two large pockets are created by the rapid evaporation of the fuel spray in this high mass and high pressure condition and are approaching the rich flammability limit while awaiting further mixing and subsequent burning.

It is suspected the cavity flow and combustion process is becoming more unstable and transient for this operating condition and configuration, resulting in periods of increasing and decreasing combustion levels and mass transfer rates with the main flow, including a higher release of unburned fuel into the main channel flow. Therefore, the cavity cross-section plane mass flow rate, and many other performance measures, fluctuates in response to the unsteady dynamics. For this lean mixture operating condition, overall efficiency is not affected due to the ability to complete the burning in the main channel flow.

4.2.4 Exhaust Temperature Distribution Evaluation. The last area to evaluate on the 3-D baseline configuration is the exhaust temperature distribution. Table 10 displays the pattern and profile factor data, as compared with the 3-D experimental configuration. Again, mixed results over the three experimental test conditions are noted,

with all performing worse by the pattern and profile factor measures except the LMMP condition, which showed improvement in its T_{mr} and profile factor measures. The atmospheric test conditions demonstrate good performance for these measures, relative to the other conditions by not having excessive maximum temperature spots.

Table 10: Exhaust temperature pattern and profile factor data for 3-D baseline configuration.

Op Cond	Model	T_{4avg} (K)	T_{mr} (K)	Pattern Factor	Profile Factor
LMLP	3-D Expr.	1178.67	1813.26	1.884	0.981
	3-D Baseline	1151.96	1769.95	2.059	0.997
LMMP	3-D Expr.	1112.75	1865.88	2.286	1.317
	3-D Baseline	1085.92	1577.84	2.501	0.902
HMHP	3-D Expr.	869.03	1183.20	2.221	0.993
	3-D Baseline	873.69	1286.45	3.610	1.286
ATM1	3-D Baseline	1064.43	1549.22	2.377	0.910
ATM2	3-D Baseline	1073.25	1594.40	2.344	0.962

The outlet plane temperature contour for the LMLP condition is viewed from Figure 32, and leads to the conclusion the high turbulence intensity from the vortex structures transporting the hot combustion products down the main flow channel continue across the exhaust plane, creating an unsteady, fluctuating exit temperature profile.

This is further evidenced by Figure 41, where the circumferentially averaged temperatures are plotted by normalized radius, to provide insight into where the temperature maximums occur. It is clear, as more turbulence is carried down the main channel flow it directly impacts the temperature distribution profile at the outlet plane, causing numerous large and small variances. For the LMLP condition, it is seen there are two separate peak temperature areas, with the more significant one seen occurring aft of the axial vane on the centerline, with a low normalized radius. However, for other operating conditions here, good radial positioning of the peak temperatures are found.

The large temperature drop on the ATM1 condition is due to a large area of reversed flow on its outlet plane.

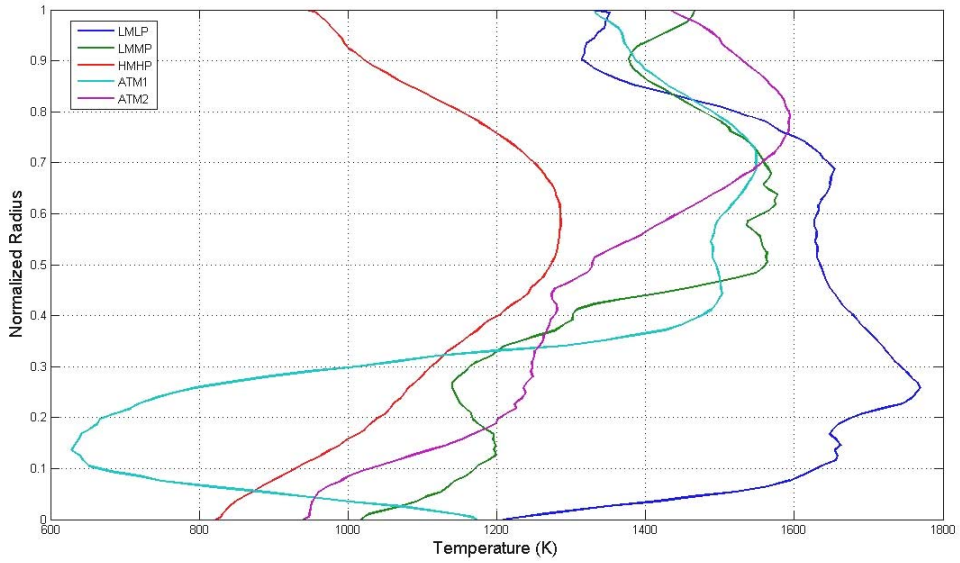

Figure 41: Circumferential averaged temperature plotted by normalized radius for outlet plane of 3-D baseline configuration.

4.3 2-D Short Planar Baseline Model

The third step of the design process is the concept testing of a flat cavity and main channel flow of the 2-D planar geometry to evaluate how the changes in geometry and physical layout affect the flow and performance of the UCC. This is the basis of one concept for recreating and viewing the cavity-vane interaction and RVC flow phenomena. Additionally, it allows the opportunity to remove the centrifugal-force effects from the combustion process to evaluate how the UCC concept works using purely turbulent diffusion flames. This configuration uses a translation periodic boundary for the cavity flow only, and the cavity structure is based on a preliminary

design without a CIAC. Preliminary design and solutions were obtained using Anisko's CFD modeling set-up. However, though the basic model geometry remained the same, the numerical grid was upgraded to the dense parameters now employed on the 3-D models, and the solutions were obtained using the improved *FLUENT* CFD set-up.

One area of difficulty was encountered in obtaining solutions for this configuration. The translational periodic boundary, used on this configuration only, produced intermittent passage for DPM fuel particles. Some particles would "abort" when crossing the periodic boundary, meaning they are abandoned due to numerical round-off errors. While the translational boundary should be fully functional, attempts to find the cause of this problem were unsuccessful. As a result, the LMLP and LMMP conditions had an approximate 5% loss of particles prior to complete evaporation or escape, not enough to significantly alter the solution. For the HMHP condition, the loss was upwards of 30% of particle tracks, a definitive source of error.

The 2-D short planar baseline configuration model is evaluated at 10,000 iterations for the LMLP and LMMP conditions, and 9,000 iterations for the HMHP condition.

4.3.1 Performance and Emissions Data Evaluation. Table 11 presents the emissions and efficiency performance data for the 2-D planar baseline configuration, in comparison with the 3-D baseline configuration. The results are actually quite close to the 3-D baseline, especially considering the modifications made to the geometry and the lack of centrifugal force. The decrease in efficiency is a result of higher UHC emissions, and this is directly attributed to the downwind side of the fuel injection spray cone

propelling some of the larger droplets directly into the main channel flow, outside the hot areas of dilution zone burning from the cavity, so they exit the combustor with minimal evaporation, thus decreasing the efficiency. Also, the flat cavity geometry provides less opportunity for the larger droplets to be captured and entrained in the cavity flow. The fuel droplet particles observed to be entrained in the cavity flow were found to continue re-circulating through the cavity and periodic boundary until evaporation was complete. The only appreciable pressure loss increase was for the HMHP condition, and it can be attributed to the increased drag encountered at higher velocities in a cavity now containing an additional 1.5 in^2 (9.68 cm^2) of surface area from the addition of a cavity floor section in the extension preceding the wall imbedded axial vane with RVC. This 1 inch (25.4 mm) extension was necessary to provide appropriate cavity volume to approximate the 3-D baseline configuration cavity volume and is also useful in beginning the design of the non-periodic sector rigs.

Table 11: Emissions and efficiency performance data for 2-D planar baseline configuration (1.5 inch cavity), comparing to 3-D baseline configuration solution data.

Op Cond	Model	CO(ppm)	CO_2 (%)	O_2 (%)	NO_x (ppm)	UHC (ppm)	η_b (%)	dP/P (%)
LMLP	3-D Baseline	2861.84	3.72	14.82	27.92	15.87	96.22	4.57
	2-D Planar Baseline	3355.21	3.61	14.94	18.80	74.03	93.92	4.22
LMMP	3-D Baseline	2040.90	3.31	15.55	43.48	1.29	97.60	2.23
	2-D Planar Baseline	1611.86	3.43	15.41	25.69	53.51	96.54	2.70
HMHP	3-D Baseline	166.61	1.84	18.08	20.27	0.05	99.62	6.09
	2-D Planar Baseline	247.86	1.73	18.24	16.78	5.62	99.11	7.46

4.3.2 Overall Solution Visualization. Figures 42 and 43 provide an overview of the 2-D planar baseline configuration solution on the LMLP operating condition. Again, there is remarkable resemblance to the 3-D baseline configuration when examining the

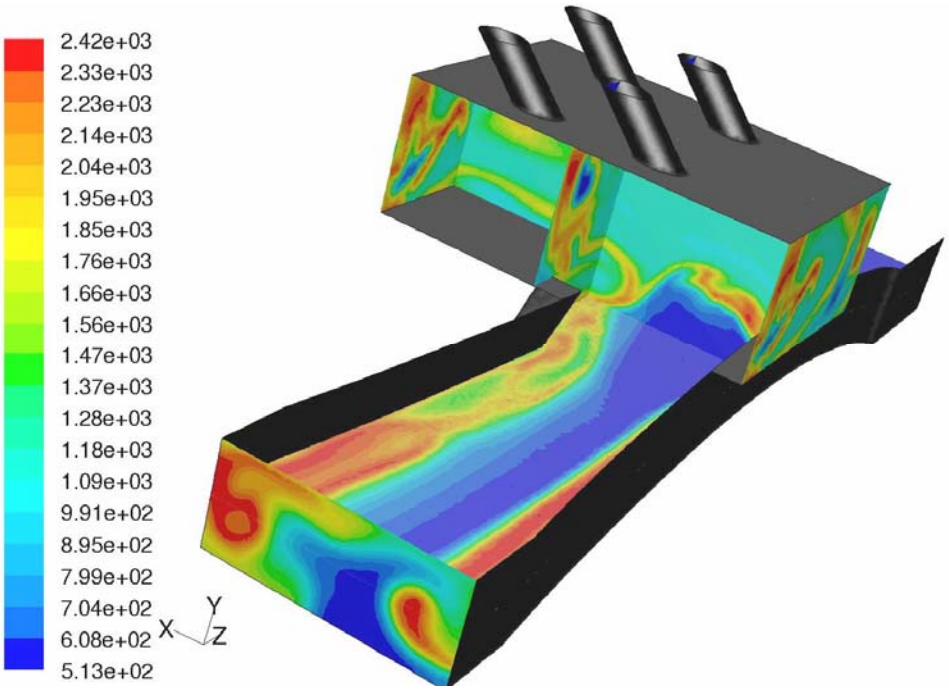

Figure 42: Contours of temperature (K) and 2-D planar baseline configuration layout, LMLP condition. Translational periodic boundary surfaces shown at ends of cavity.

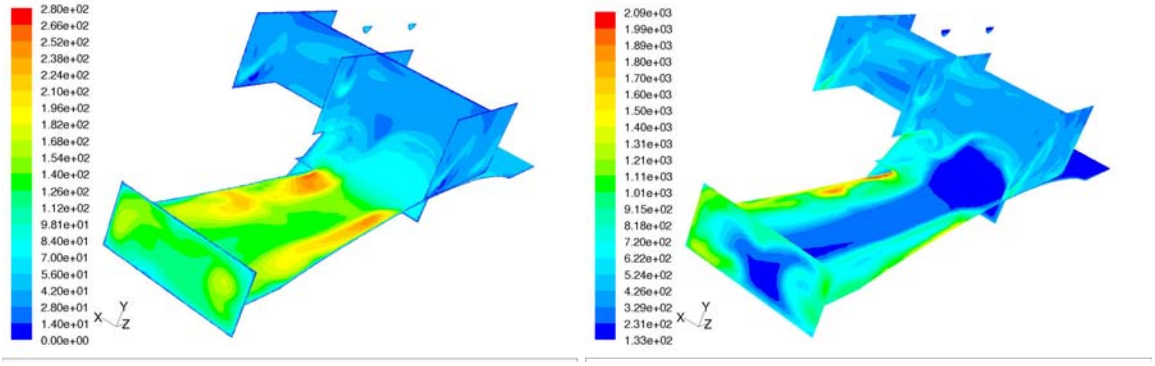

Figure 43: Contours of velocity magnitude (m/s) (left) and turbulence intensity (%, read as e+01) (right) for 2-D planar baseline configuration, LMLP condition.

macro-flow features. Envelopes of hot and cold gases in the cavity indicate turbulent flame propagation through the mixture, though the hottest burning areas appear to be near the lower levels of the cavity and vertically along the aft wall. The flames are slowly propagating into the colder areas, containing the higher mixture fraction and exhibiting elevated temperatures of pre-heating.

The RVC generated vortex is evident, pulling hot combustion gases from the cavity into the main flow, in concert with a weakly developing vortex across the main channel, replicating the phenomena seen on previous configurations for the LMLP condition. The extended combustion process in the dilution zone traveling down the main flow to the outlet is also evident, with the HMHP condition showing a large increase in the burning in this area. The velocity and turbulence intensity patterns are very similar along the appropriate sides of the axial vane (now in different relative positions in the main channel flow), having been generated by the same cavity-vane interaction flow characteristics observed on the two previous configurations. Temperature, velocity, and turbulence intensity are of near identical magnitude as compared to the 3-D baseline configuration LMLP solution, as well as the LMMP and HMHP solutions not shown.

4.3.3 Cavity Flow and Cavity-vane Interaction Evaluation. Table 12 presents the cavity flow parameter data for the 2-D planar baseline configuration, comparing to the 3-D baseline configuration results. The x-component (converted to positive value) and y-component of velocity computed for the 2-D model are equivalent to tangential and radial components on the 3-D axi-symmetric configurations, based on the U_θ plane

orientation of the 3-D configurations is on the centerline coincident with the cartesian coordinate origin plane (x=0 plane). The slight CLP reduction between the 2-D and 3-D configurations is based on a slightly larger cavity volume for the 2-D planar configuration. Cavity mass entrainment has decreased significantly on the LMLP and LMMP conditions, to less than three times the cavity air injection rate. The HMHP condition essentially remains the same, considering the 3-D baseline cavity cross section plane mass flow figure is thought to be a low fluctuation.

Table 12: Cavity flow parameters for 2-D planar baseline configuration, with mass weighted average velocities for U_θ plane, comparing with 3-D baseline configuration solution data.

Op Cond	Model	CLP	$\dot{m}_{cav}$ $\frac{lbm}{\min}$ $\left(\frac{kg}{\min}\right)$	$\dot{m}_{cavplane}$ $\frac{lbm}{\min}\left(\frac{kg}{\min}\right)$	U_θ (m/s)	U_r (m/s)
LMLP	3-D Baseline	0.366	1.072 (0.486)	3.549 (1.610)	40.40	-7.75
	2-D Planar Baseline	0.343	1.072 (0.486)	2.862 (1.298)	43.28	-5.72
LMMP	3-D Baseline	0.259	1.032 (0.468)	3.691 (1.674)	34.01	-6.37
	2-D Planar Baseline	0.239	1.032 (0.468)	2.741 (1.243)	35.09	-4.14
HMHP	3-D Baseline	0.351	2.120 (0.962)	5.949 (2.698)	60.76	-9.42
	2-D Planar Baseline	0.318	2.120 (0.962)	6.223 (2.823)	67.04	-8.03

An increase in U_θ, is noted for all conditions, over that found in the 3-D baseline configuration, a surprising result considering the geometry of flattening the cavity should decrease the x-component from the air inlet jets (angle remains constant from the radial or vertical). Further, it is noted U_r actually decreases for all conditions, but as with the tangential velocity, the geometry flattening should lead to a radial velocity increase. However, for the UCC, the decrease of U_r for the flattened cavity indicates the loss of buoyancy effects in the cavity flow, to be expected since the centrifugal-force effect has been removed.

Figure 44 is the close-in cutaways for the cavity fuel and cavity-vane planes displaying velocity vectors with temperature, for the LMLP condition, to closely examine the cavity flow. As previously observed, the high temperature burning areas are located along the cavity side walls and floor, leaving the central area as a cooler mixing area for the fuel rich air into which the diffusion flame can propagate. On the cavity fuel plane, the detail of the RVC generated vortex into the main channel flow is clear, and it is observed to have a mixture of hot and cold gases entrained. The origin of the second vortex structure across the main flow approaching the upwind side of the axial vane is also evident, again entraining and transferring hot and cold masses between the cavity and main flow. The first vortex structure mixing effect can then be seen in the cavity-vane plane as mixed areas of burning in the RVC, contrasting with previous 3-D cutaways showing much higher combustion activity in the RVC. The last item to note is the location of the impinging air inlet jets on the cavity-vane plane, observing their cold temperature signature is just above the cavity mid-radius.

Next, evaluation of the tangential velocity profile of the cavity cross-section is accomplished in Figure 45. The range of tangential velocities on each condition remains essentially the same in comparison with the 3-D baseline configuration data from Figure (36), but the shape of the profile has altered. The cavity air inlet jets influence is the large distinct peak just above mid-radius. Below these peaks the localized acceleration by decreasing height is slower than the 3-D configurations, due to lack of curvature, until the bottom of the cavity, where the RVC vortex creates a large acceleration in pulling mass from the cavity into the RVC and main flow.

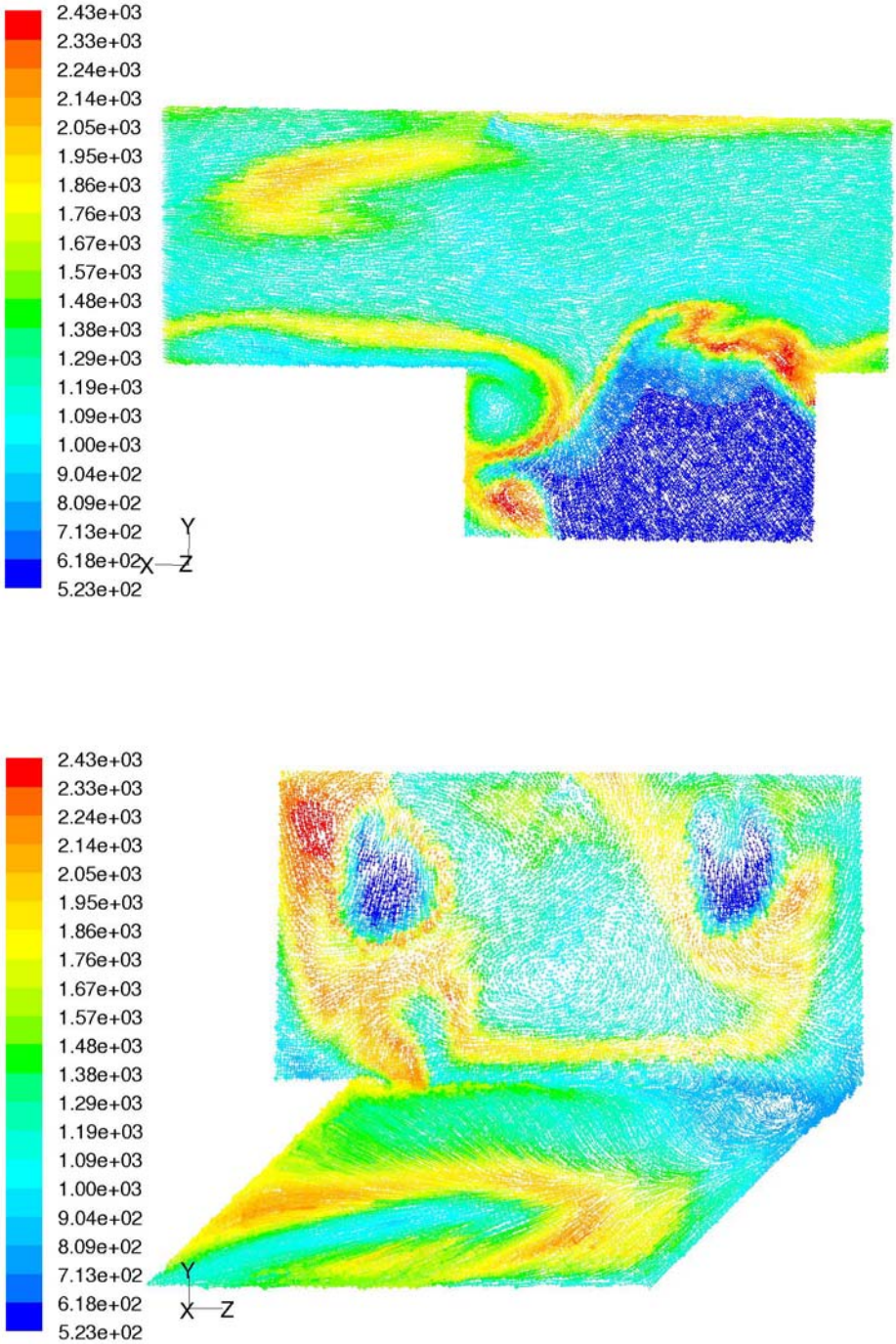

Figure 44: Cavity fuel plane (top, cavity flow left to right) and cavity-vane plane (bottom, cavity flow out of page) velocity vectors colored by temperature (K) for 2-D planar baseline configuration, LMLP condition.

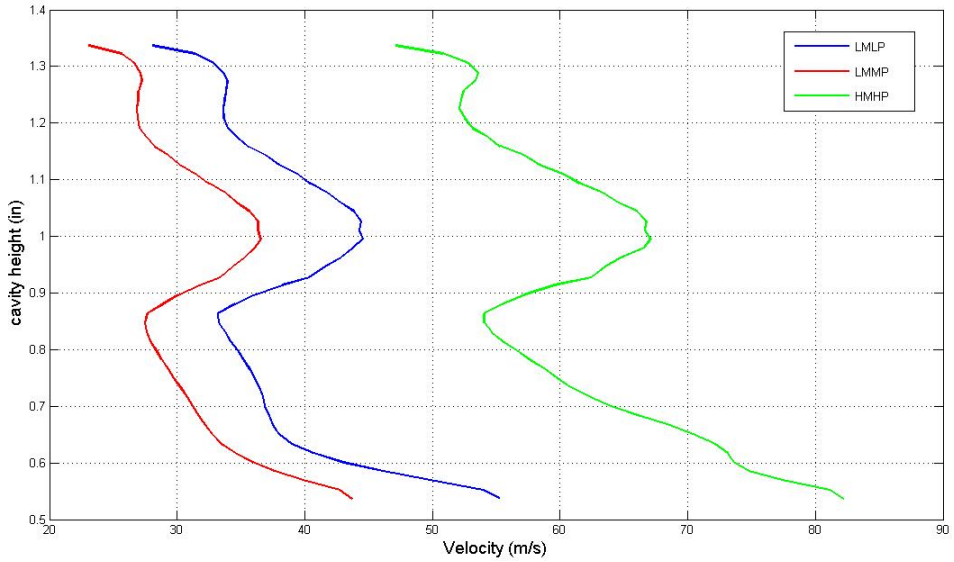

Figure 45: Circumferentially averaged x-component velocities plotted by cavity height on U_θ plane for 2-D planar baseline configuration.

As an overview, the cavity-vane flow interaction in the 2-D planar baseline configuration follows the dynamics observed on the 3-D configurations, with the largest difference being the combustion state of the gases involved in the mass exchanges. The 2-D configuration tends to have less complete combustion occurring in the cavity, with more residual burning occurring in the main channel flow dilution zone, concurring with the observed decrease in efficiency.

4.3.4 Exhaust Temperature Distribution Evaluation. The new main channel and outlet geometry for the 2-D configurations does not allow for computing of useful circumferential averaged radial temperatures, nor would a comparison with the 3-D configuration outlet shape be valid with this data. Therefore, 2-D configuration exhaust temperature will be evaluated quantitatively with pattern factor and qualitatively by

inspection of the outlet temperature contours for comparison with the 3-D baseline configuration. This is also justified as the sector rigs are designed for cavity-vane interaction, and the exhaust outlet flow is significantly degraded in relation to the 3-D configurations.

Table 13 displays the temperature and pattern factor results for the 2-D planar baseline configuration in comparison with the 3-D baseline configuration. Maximum temperature and pattern factor compares favorably with the 3-D baseline data for the LMLP and LMMP conditions. The HMHP condition indicates a higher maximum temperature and pattern factor, resulting from the observed higher rate of residual burning in the main channel flow to the outlet.

Table 13: Exhaust temperature pattern factor data for 2-D planar baseline configuration, comparing with 3-D baseline configuration solution data.

Op Cond	Model	T_{4avg}	T_{4max}	Pattern Factor
LMLP	3-D Baseline	1151.96	2428.74	2.059
	2-D Planar Baseline	1145.81	2423.77	2.081
LMMP	3-D Baseline	1085.92	2449.59	2.501
	2-D Planar Baseline	1113.28	2421.75	2.286
HMHP	3-D Baseline	873.69	2032.04	3.610
	2-D Planar Baseline	848.67	2261.40	4.776

The outlet temperature contours for the 2-D planar baseline configuration are viewed from Figure 42, and compared with the 3-D baseline in Figure 32. In comparing the differing configuration geometries, the extended axial vane is located on the sides of the 2-D and the centerline of the 3-D configuration, so these are equivalent reference lines for visual comparison with the 30^o geometry rotation. The general profiles between the two are similar, reflecting the hot areas of the shed vortex's residual burning

occurring along each side of the vane, with cooler air in the mid-vane area. It can be estimated the 2-D maximum temperature band (T_{mr}) would occur roughly mid-height, again corresponding with the 3-D baseline configuration.

4.4 2-D Curved Cavity Sector Rig

The 2-D curved sector rig design evolved from the 2-D planar baseline configuration main channel section, combined with an enclosed 120^{o} curved cavity section replicating the cavity characteristics of the 3-D baseline model, as viewed in Figure 46. The curved cavity center of radius is coincident with the extended plane of the axial vane wall. As a result of using only a double section for the cavity, 120^{o} of cavity circumference to reproduce re-circulation and mass entrainment, and not desiring to increase the individual cavity air inlet mass flow rates, the achievement of the full cavity mass entrainment observed on the 3-D configurations will not be achieved. Maintaining a simple design and laboratory limitations are also considered in this decision.

Several design variations were tested and evaluated to determine the best method to manage the exhaust of cavity air not joining the main channel flow, with the problem of too much entrainment from the main flow into the cavity exhaust the most significant, far outweighing the mass gain from the cavity at the RVC interaction. The resultant design is a cavity exhaust area of smaller cross-sectional area, created by extending the top cavity wall until directly over the far main channel wall. While mass entrainment from the main flow into the cavity is higher than desired, it is nonetheless an existing dynamic of the UCC flow, and accepted here because the primary intent is to evaluate the cavity-vane flow interactions. The exhaust outlet performance parameters are evaluated

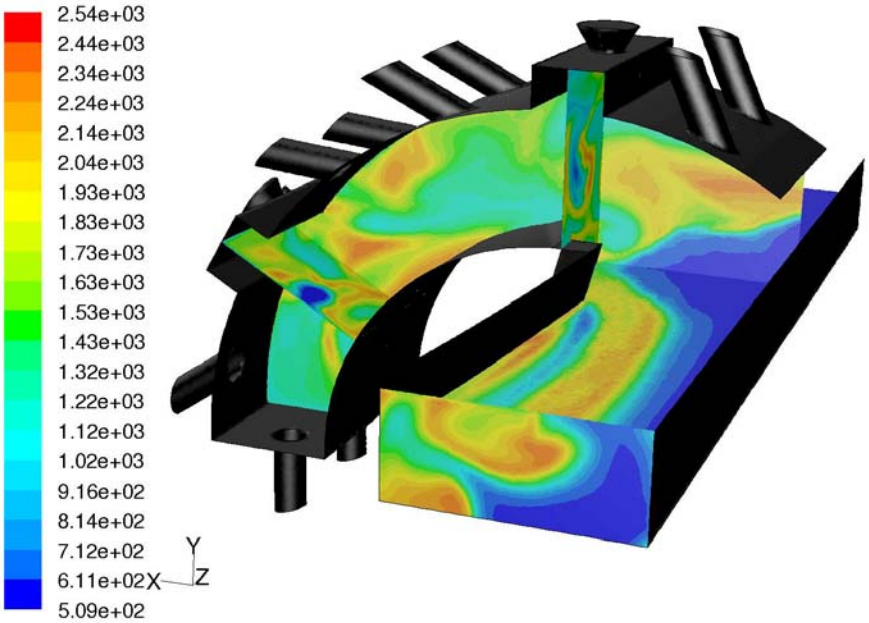

Figure 46: Contours of temperature (K) for the 2-D curved sector rig, LMLP condition. Viewed from exhaust, main channel flow out of page, cavity flow is clockwise left to right.

at approximately 30% less mass flow rate than the 3-D configurations, and therefore comparison with the 3-D data is for reference and comparison only. Cavity exhaust data was not collected beyond observing the cavity outlet mass flow rate

4.4.1 Performance and Emissions Data Evaluation. Table 14 displays the emissions and performance data for the 2-D curved sector rig at the one pressurized operating condition (LMLP, 10,000 iterations) and the two atmospheric conditions (ATM1, ATM2 at 11,000 iterations). The data leads to several general conclusions to be expected with the significantly altered mass flow patterns in the now non-recirculating combustor. The very high CO emissions, combined with elevated NO_x emissions, are due to the reduced effect of dilution zone in the main flow with 30% less clean air. This is also evidenced in Figure 46 on the temperature contour overview.

Table 14: Emissions and performance data for 2-D curved sector rig, comparing with 3-D baseline configuration data.

Op Cond	Model	CO(ppm)	CO_2 (%)	O_2 (%)	NO_x (ppm)	UHC (ppm)	η_b (%)	dP/P (%)
LMLP	3-D Baseline	2861.84	3.72	14.82	27.92	15.87	96.22	4.57
	Crv Sct Rig	13014.07	2.52	15.76	53.64	20.98	94.36	1.35
ATM1	3-D Baseline	1498.03	3.28	15.66	6.85	19.06	97.71	7.86
	Crv Sct Rig	12386.63	3.39	14.40	25.42	9.94	95.10	2.85
ATM2	3-D Baseline	2793.39	3.29	15.50	9.45	13.12	94.49	4.35
	Crv Sct Rig	18399.67	3.36	13.90	33.50	4.98	92.86	1.83

The UHC emissions data is useful information, as it indicates good evaporation of the fuel droplets, especially at the atmospheric test conditions. Pressure loss efficiency is significantly lower, but this is due to the cavity exhaust pressure being set as identical to the main exhaust pressure (as it will be in the laboratory), and the main flow entrainment into the cavity merely leaves less flow to create drag in the second half of the combustor.

4.4.2 Overall Solution Visualization. Figure 46 displays the 2-D curved sector rig's temperature contours on the LMLP condition, for an examination of the combustion profile. Interesting burning profiles are indicated through the cavity, particularly in the area of the first fuel injection. However, an investigation of the fuel droplet trajectories provides an explanation. At the first fuel injection point, near the start of the cavity flow, the mass flow and velocity has not built up to the full entrained level, so the fuel droplet cone spray trajectory is largely unaffected, and most particles bounce off the cavity floor before completing evaporation, creating a rich area for burning near the bottom of the cavity, as evidenced on the temperature contours. An area of burning in the upper cavity and downwind from the fuel injection is also present, spreading along the outer radius in the flow direction and over an area of colder gas located between the fuel injection

points. The area around the second fuel injection point, over the axial vane, exhibits behavior consistent with our previous 3-D configurations, and the combustion continues strongly along the cavity flow into the cavity exhaust, enhanced by the extra turbulent mixing of the main flow entrainment and exhaust suction. Also, as already noted, large areas of burning are visible in the RVC shed vortex trailing down the main flow, conforming to known behavior.

Figure 47 provides the overview of velocity and turbulence intensity patterns for this configuration, LMLP condition, with the results in the area of the cavity to main flow interaction exhibiting the flow characteristics desired from the 3-D configurations. The velocity contours indicate increased lateral dissipation of the turbulent flow down the main channel (also observed on the temperature contours), likely due to the absence of the accompanying aerodynamic vane and elimination of the nozzle effect of the intervene passage. Finally, but most importantly, the peak areas of turbulence intensity in the wake of the RVC are of reduced magnitude for this configuration. This is most likely caused by the reduced cavity mass flow crossing over the axial vane, reducing the intensity of the cavity-vane turbulent interaction.

The atmospheric condition cutaways display similar patterns, with the exception of the temperature contours, where greater cavity burning is achieved for ATM2, due to the increased evaporation rate, and the turbulence intensity again decreases as mass flow decreases. Cutaways for select contours and velocity vectors for the visualization planes for ATM2 are contained in Appendix B.

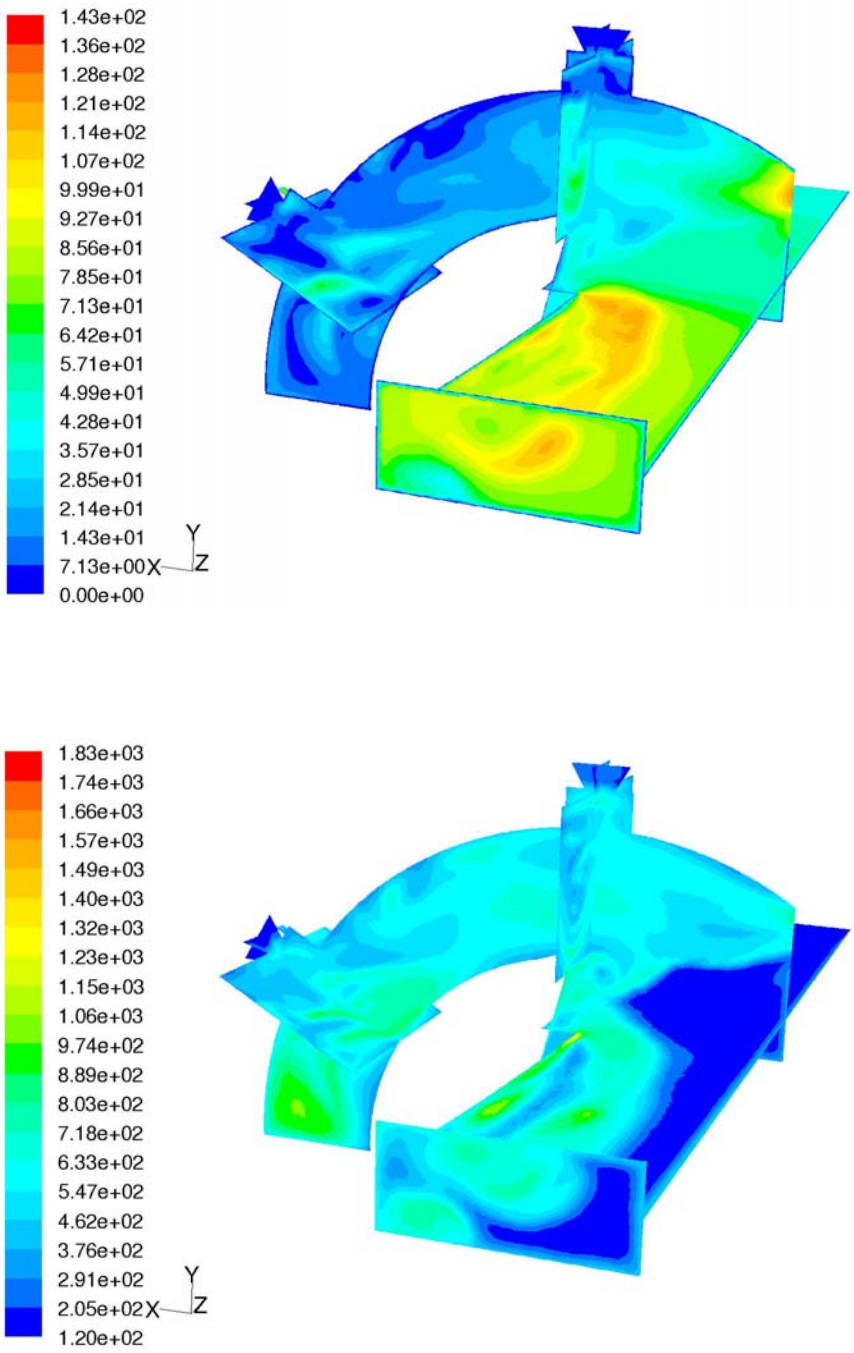

Figure 47: Contours of velocity magnitude (m/s) (top) and turbulence intensity (%, read as e+01) (bottom) for 2-D curved sector rig, LMLP condition.

4.4.3 Cavity flow, G-loading, and Cavity-vane Interaction Evaluation. Table 15 displays the cavity flow data for the 2-D curved sector rig, in comparison with the 3-D baseline configuration it is attempting to reproduce, where cavity inlet mass flow is indicative of four air inlets for 3-D and ten air inlets for the sector rigs. CLP values are higher for the sector rigs for this reason. The cavity cross-section plane mass flow rate and U_θ velocities are important measures of performance for the sector configuration. As expected based on design and cavity mass injection, the mass flow rate only doubled, not fully achieving the entrainment level of the periodic 3-D baseline configuration. However, average tangential velocities are reproduced to within a reasonable accuracy. Radial velocities are on the order of 50% less.

Table 15: Cavity flow parameters for 2-D curved sector rig, with average velocities for U_θ plane, compared with 3-D baseline configuration.

Op Cond	Model	CLP	$\dot{m}_{cav}$ $\frac{lbm}{\min}$ $\left(\frac{kg}{\min}\right)$	$\dot{m}_{cavplane}$ $\frac{lbm}{\min}\left(\frac{kg}{\min}\right)$	U_θ (m/s)	U_r (m/s)
LMLP	3-D Baseline	0.366	1.072 (0.486)	3.549 (1.610)	40.40	-7.75
	Crv Sct Rig	0.487	2.680 (1.216)	2.602 (1.180)	40.39	-3.41
ATM1	3-D Baseline	1.081	0.536 (0.243)	1.883 (0.854)	58.67	-8.44
	Crv Sct Rig	1.433	1.340 (0.608)	1.323 (0.600)	56.78	-4.47
ATM2	3-D Baseline	0.924	0.429 (0.195)	1.780 (0.807)	48.71	-5.30
	Crv Sct Rig	1.168	1.072 (0.486)	1.013 (0.460)	44.13	-2.61

Figures 48 and 49 provide the velocity vector colored by temperature visualization of the cavity fuel and cavity-vane planes for the 2-D curved cavity sector rig compared with the 3-D baseline configuration. Beyond the previously discussed temperature contour combustion locations, the mixing from buoyancy effects is evident, together with distinct flame fronts throughout the cavity cross-section. On the cavity fuel

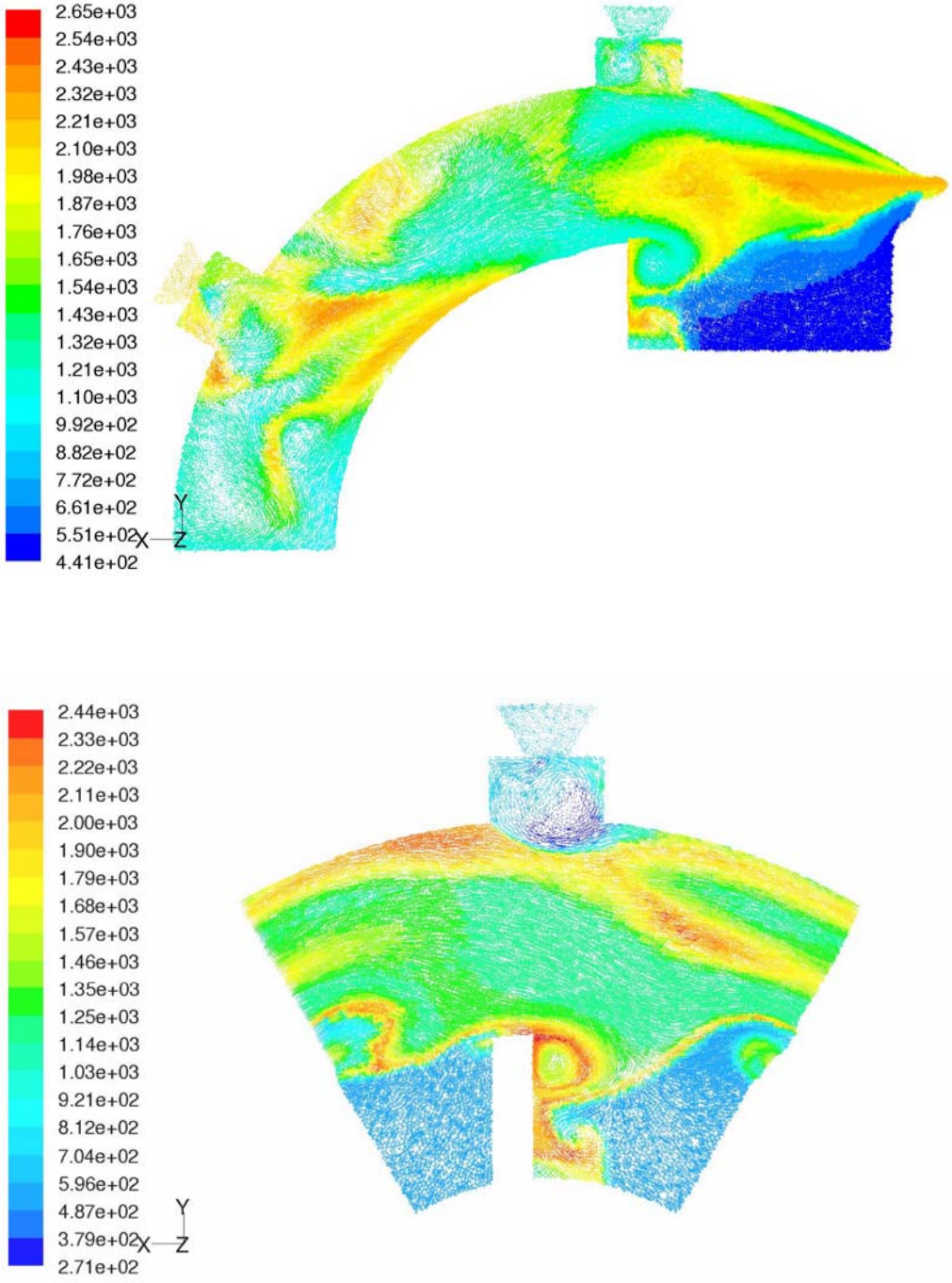

Figure 48: Comparison of 2-D curved cavity sector rig cavity fuel plane (top, cavity flow clockwise left to right) and 3-D baseline configuration cavity fuel plane (bottom, cavity flow clockwise left to right). Velocity vectors colored with temperature (K), viewed from exhaust, LMLP condition.

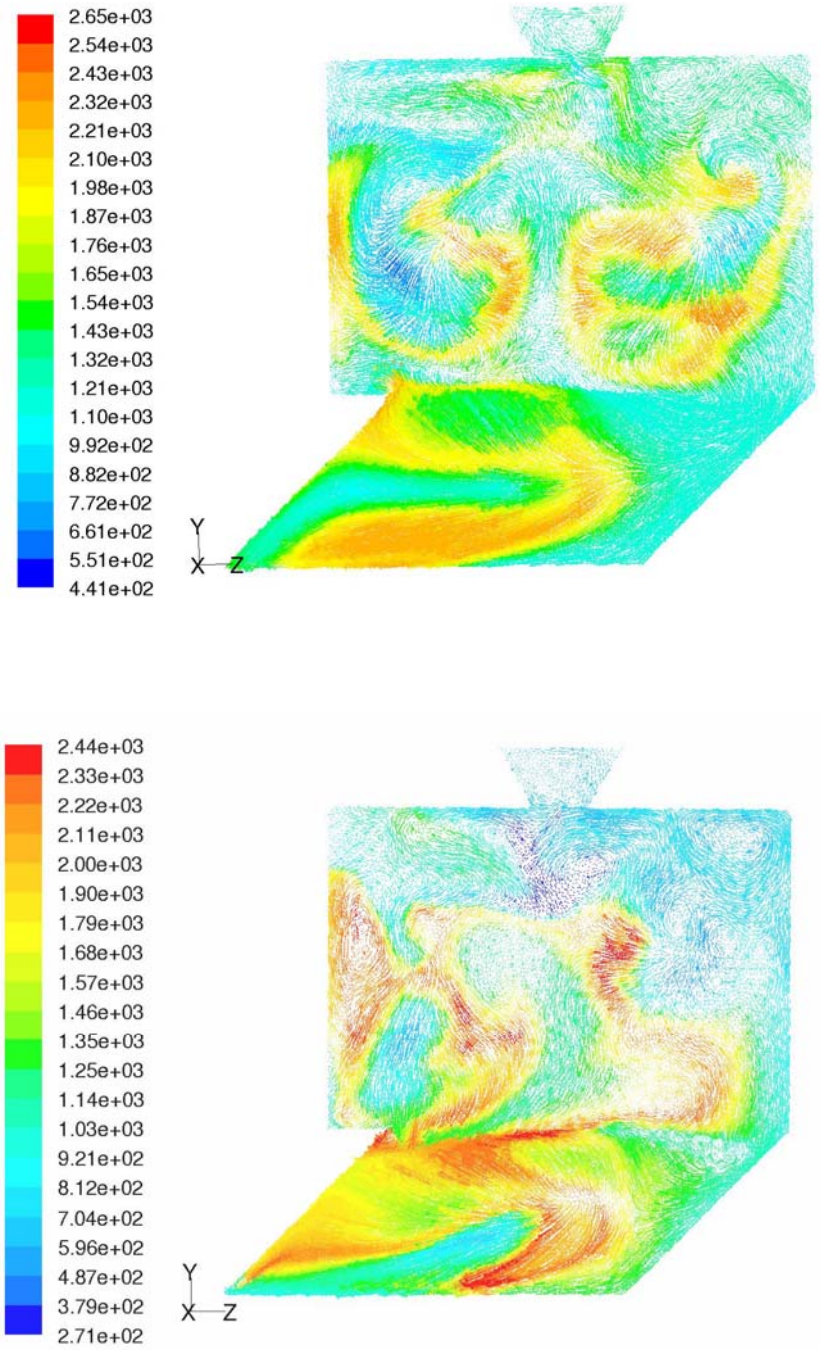

Figure 49: Comparison of 2-D curved cavity sector rig cavity-vane plane (top, cavity flow out of page) and 3-D baseline configuration cavity-vane plane (bottom, cavity flow out of page). Velocity vectors colored with temperature (K), LMLP condition.

plane, the distinct RVC vortex is visible, with its accompanying swirl pattern down the axial length of the RVC in the cavity-vane plane view. Generating this important flow characteristic driving the cavity to main flow interaction is confirmation this sector rig design is successfully reproducing the 3-D flow.

Additional information to be observed on this cutaway is the cause of the decrease in radial velocity on the cavity-vane plane. The cavity fuel plane cutaway clearly shows the cavity flow when crossing over the main channel flow, becomes dominated by the acceleration into the cavity exhaust, effectively pulling the cavity flow horizontally across the main channel width. This effect contributes to both decreasing the downward radial velocity and artificially increasing the tangential velocity measured on the cavity cross-section plane.

Figures 50 and 51 plot the average tangential velocity and calculated g-loading by radius for the U_θ plane. The expected inlet jet peaks are evident on the LMLP and ATM1 condition, where the ATM2 condition is approaching the smoother profile associated with the shortened cavity under proper loading. A velocity and g-loading range equivalent to the 3-D baseline range is produced on the LMLP condition, and reduced peak and range for ATM1 and ATM2 is observed. The large tangential velocity reduction at the lower radius, the tail, is produced by a larger diameter RVC vortex extending up into the U_θ and swirling this area of flow downward. Overall, the tangential velocity and g-loading profiles adequately reproduce the flow from the 3-D baseline configuration.

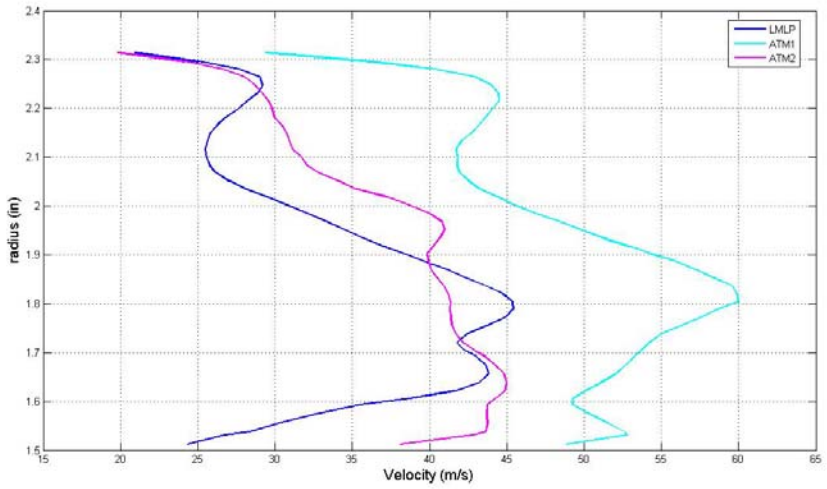

Figure 50: Circumferential averaged tangential velocities plotted by radius on U_θ plane for 2-D curved sector rig.

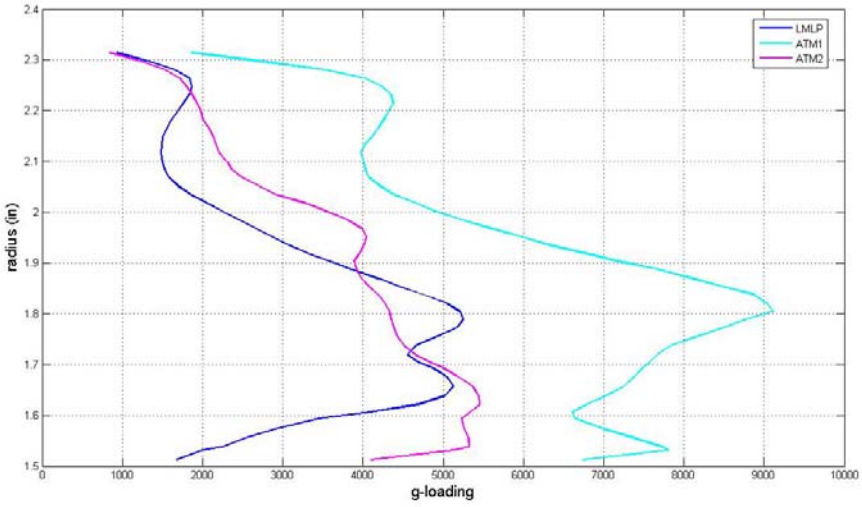

Figure 51: Circumferential averaged g-loading plotted by radius on U_θ plane for 2-D curved sector rig.

4.4.4 Exhaust Temperature Distribution Evaluation. A brief overview of temperature distribution at the exhaust outlet is conducted from Table 16, displaying pattern factor data, and Figure 46, for the outlet temperature contours. Differences with

the 3-D baseline configuration include an approximately 30% exhaust mass flow reduction due to cavity exhaust entrainment and a reconfigured planar main channel containing only half an axial vane. Pattern factor data comparison is mixed with the atmospheric conditions showing improvement, however the pattern factor changes are mostly a resultant of 100 K temperature shifts in T_{4avg}. Visual evaluation of the 2-D curved sector rig outlet plane temperature contours follows from the previous observation of a wider lateral distribution and dissipation of the RVC vortex, carrying hot combustion products from this vortex across a wider area. Additionally, due to the lack of an upwind axial vane section on the second main channel wall, and the high mass entrainment into the cavity, the second vortex and hot combustion flow down the channel along the upwind side of the axial vane is not present in any condition for the curved sector rig.

Table 16: Exhaust temperature pattern factor data for 2-D curved sector rig compared with 3-D baseline configuration.

Op Cond	Model	T_{4avg}	T_{4max}	Pattern Factor
LMLP	3-D Baseline	1151.96	2428.74	2.059
	Crv Sct Rig	1019.49	2343.27	2.714
ATM1	3-D Baseline	1064.43	2330.460	2.377
	Crv Sct Rig	1159.21	2324.58	1.857
ATM2	3-D Baseline	1073.25	2342.39	2.340
	Crv Sct Rig	1189.97	2313.32	1.707

4.5 2-D Planar Cavity Sector Rig

The second sector rig is a flat cavity design, based on the 2-D planar baseline configuration that used periodic boundaries, and is viewed in Figure 52. The greatest benefit to this test configuration for experimental testing is the ease of manufacture and simplicity of alignment for accurate laser diagnostics. The cavity was again doubled

leading into a single section main flow, again to recreate some cavity entrainment prior to interaction with the axial vane RVC and main channel flow. Main mass entrainment losses to the cavity exhaust for this configuration slightly exceeded the level of the curved cavity sector rig.

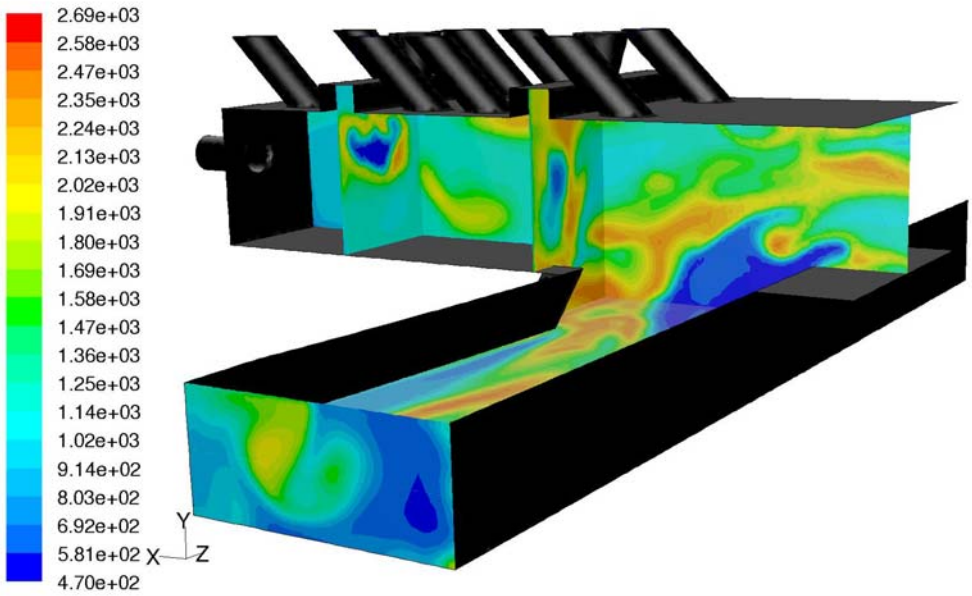

Figure 52: Contours of temperature (K) for 2-D planar sector rig, LMLP condition.

4.5.1 Performance and Emissions Data Evaluation. Table 17 displays the emissions and performance data for the 2-D planar sector rig, in comparison with the 3-D baseline configuration, evaluated at 10,000 iterations (LMLP) and 11,000 iterations (ATM1, ATM2). Note the high combustion efficiencies computed at the main exhaust outlet (cavity exhaust parameters not collected or analyzed, except mass flow), resultant from decreased UHC emissions. This is attributable to good evaporation rates through the combustor, including the atmospheric conditions, such that a minimal number of

particles with trajectories into the main flow actually escaped. Some particles escaping prior to evaporation through the cavity exhaust were noted. Also of note in the emissions data is an increase in the NO_x emissions.

Table 17: Emissions and efficiency performance data for 2-D planar sector rig, compared with 3-D baseline configuration.

Op Cond	Model	CO(ppm)	CO_2 (%)	O_2 (%)	NO_x (ppm)	UHC (ppm)	η_b (%)	dP/P (%)
LMLP	3-D Baseline	2861.84	3.72	14.82	27.92	15.87	96.22	4.57
	Planar Sct Rig	402.68	2.14	17.58	102.81	8.79	99.76	1.00
ATM1	3-D Baseline	1498.03	3.28	15.66	6.85	19.06	97.71	7.86
	Planar Sct Rig	2586.95	2.85	16.23	43.13	1.35	99.12	1.80
ATM2	3-D Baseline	2793.39	3.29	15.50	9.45	13.12	94.49	4.35
	Planar Sct Rig	1665.53	3.05	16.01	42.43	0.72	99.45	1.15

4.5.2 Overall Solution Visualization. Figures 52 and 53 provide the flow overview for the planar sector rig. The temperature contours are indicative of turbulent diffusion flames, since the centrifugal-force effects have been removed, and seem to again offer less volume of combustion activity in the cavity. The now standard RVC generated vortex is again evident transferring mass between the cavity and main flow channel via the RVC. The velocity contours bear resemblance to the curved sector rig in the form of accelerating flow toward the cavity exhaust and a wider area of velocity acceleration in the main channel flow, also corresponding with a wider area of hot reacting gases in the main channel flow exhaust area. Turbulence intensity peaks are again greatly diminished compared with the 3-D baseline configuration on the LMLP condition examined here, as well as on the atmospheric conditions. ATM2 operating condition selected flow visualization cutaways are contained in Appendix C.

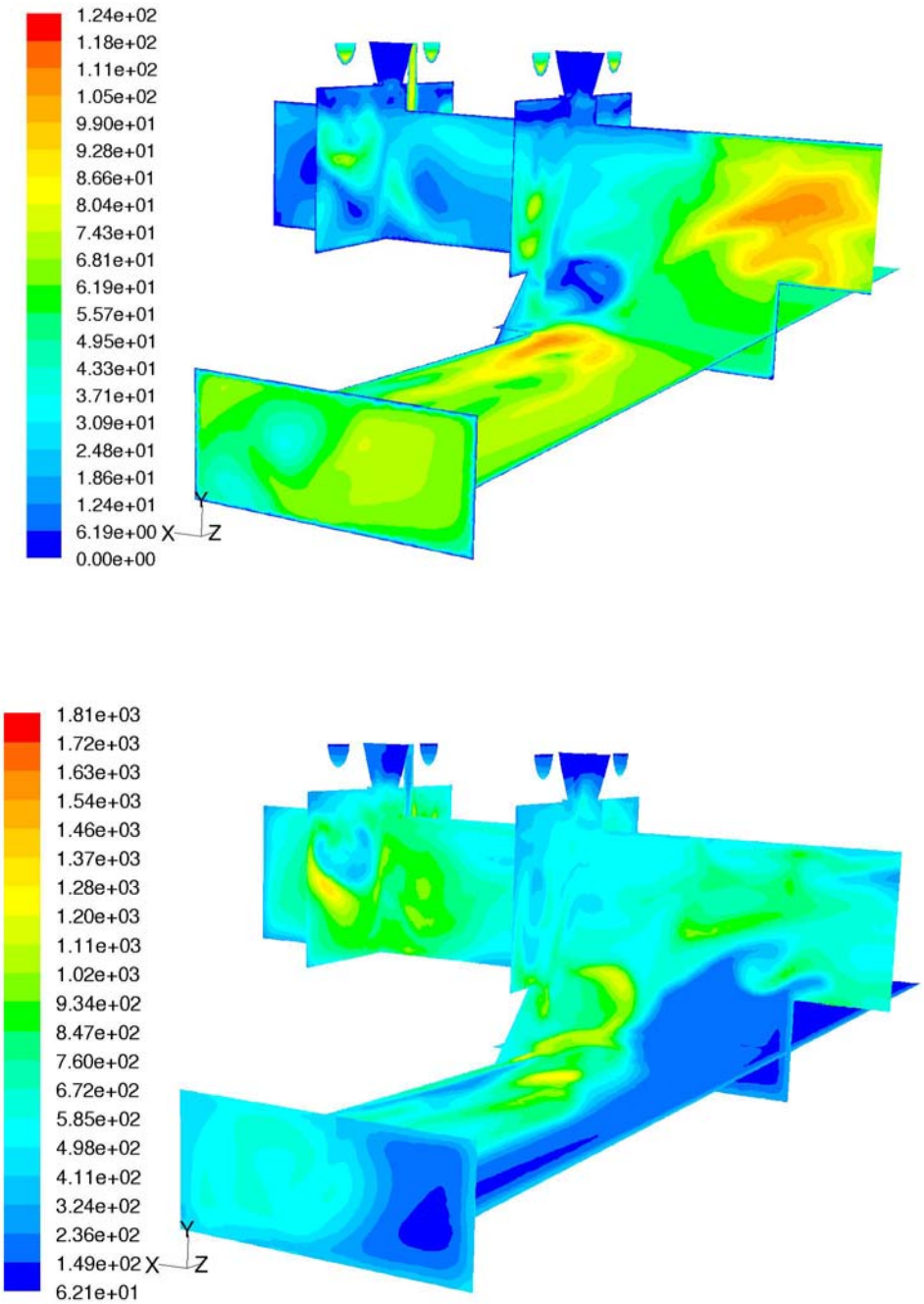

Figure 53: Contours of velocity magnitude (m/s) (top) and turbulence intensity (%, read as e+01) (bottom) for 2-D planar sector rig, LMLP condition.

4.5.3 Cavity flow and Cavity-vane Interaction Evaluation. Table 18 presents the cavity flow parameter data for the 2-D planar sector rig in comparison with the 3-D baseline configuration data. The cavity mass flow entrainment of double the 3-D cavity inlet flow is achieved, but still not reaching the level of entrainment of the 3-D configurations, by design. For the flat cavity, the tangential velocities are slightly lower and the radial velocities slightly higher than the 3-D baseline configuration. This shift is directly attributable to the geometry of the flattened cavity and cavity air inlet's lateral position being closer to the fuel injection plane, as was discussed for the 2-D planar baseline configuration, and again works to the benefit of improved interaction in the cavity-vane flow area.

Table 18: Cavity flow parameters for 2-D planar sector rig, with average velocities for U_θ plane, comparing with 3-D baseline configuration.

Op Cond	Model	CLP	$\dot{m}_{cav}$ $\frac{lb_m}{\min}\left(\frac{kg}{\min}\right)$	$\dot{m}_{cavplane}$ $\frac{lb_m}{\min}\left(\frac{kg}{\min}\right)$	U_θ (m/s)	U_r (m/s)
LMLP	3-D Baseline	0.366	1.072 (0.486)	3.549 (1.610)	40.40	-7.75
	Planar Sct Rig	0.505	2.680 (1.216)	2.580 (1.170)	36.41	-11.26
ATM1	3-D Baseline	1.081	0.536 (0.283)	1.883 (0.854)	58.67	-8.44
	Planar Sct Rig	1.506	1.340 (0.608)	1.289 (0.585)	52.20	-16.48
ATM2	3-D Baseline	0.924	0.429 (0.195)	1.780 (0.807)	48.71	-5.30
	Planar Sct Rig	1.219	1.072 (0.486)	1.015 (0.460)	42.86	-14.66

Next, Figures 54 and 55 provide the velocity vector colored by temperature visualization of the cavity fuel and cavity-vane planes for the 2-D planar sector rig compared with the 3-D baseline configuration for the LMLP condition. The now familiar flow patterns highlighted by the RVC generated vortex pulling hot combustion gases through the RVC into the main channel flow to complete burning. However, for this condition on the cavity fuel plane, the RVC vortex has taken somewhat of a new form,

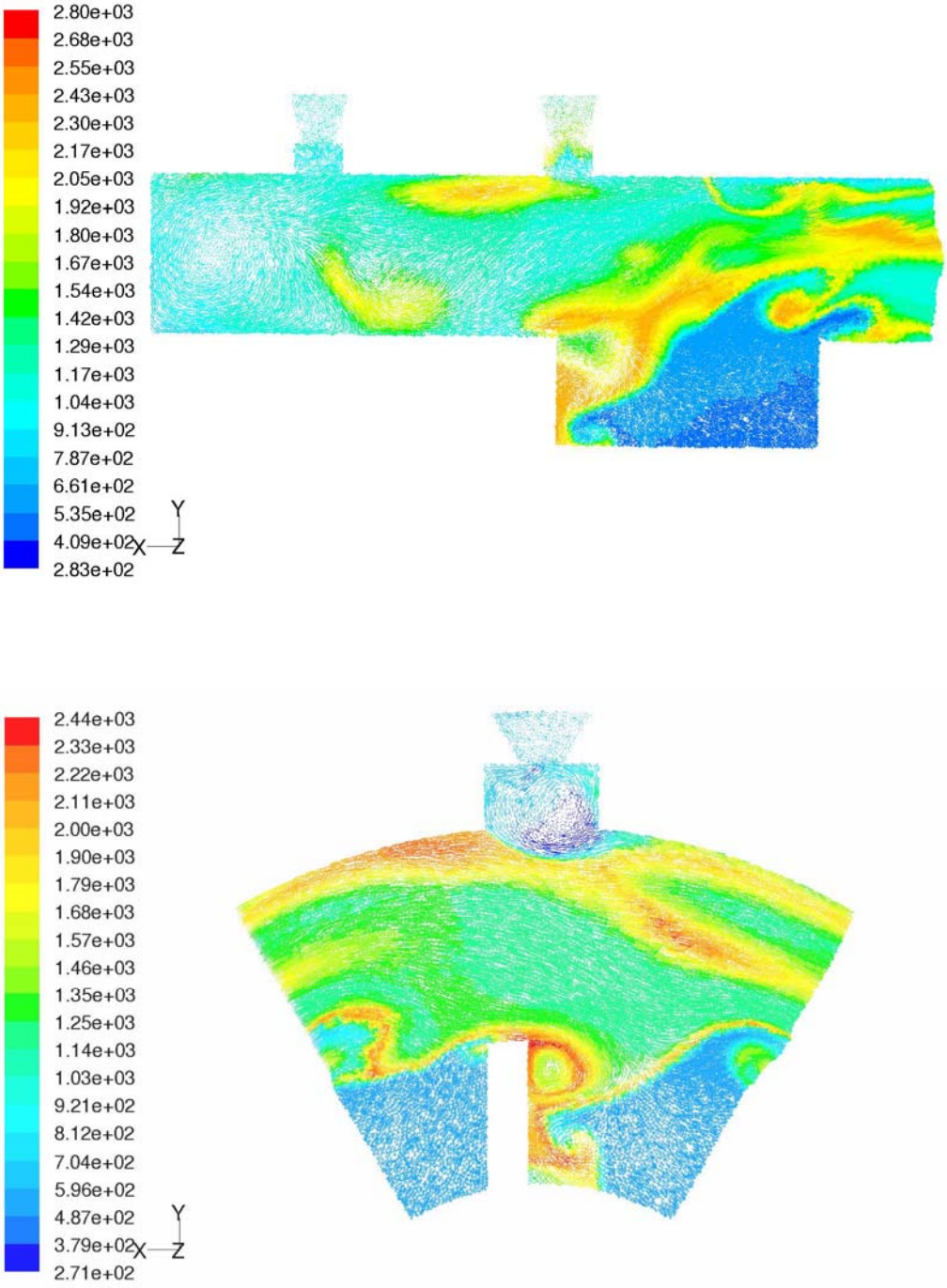

Figure 54: Comparison of 2-D planar sector rig cavity fuel plane (top, cavity flow left to right) and 3-D baseline configuration cavity fuel plane (bottom, cavity flow clockwise left to right). Velocity vectors colored with temperature (K), viewed from exhaust, LMLP condition.

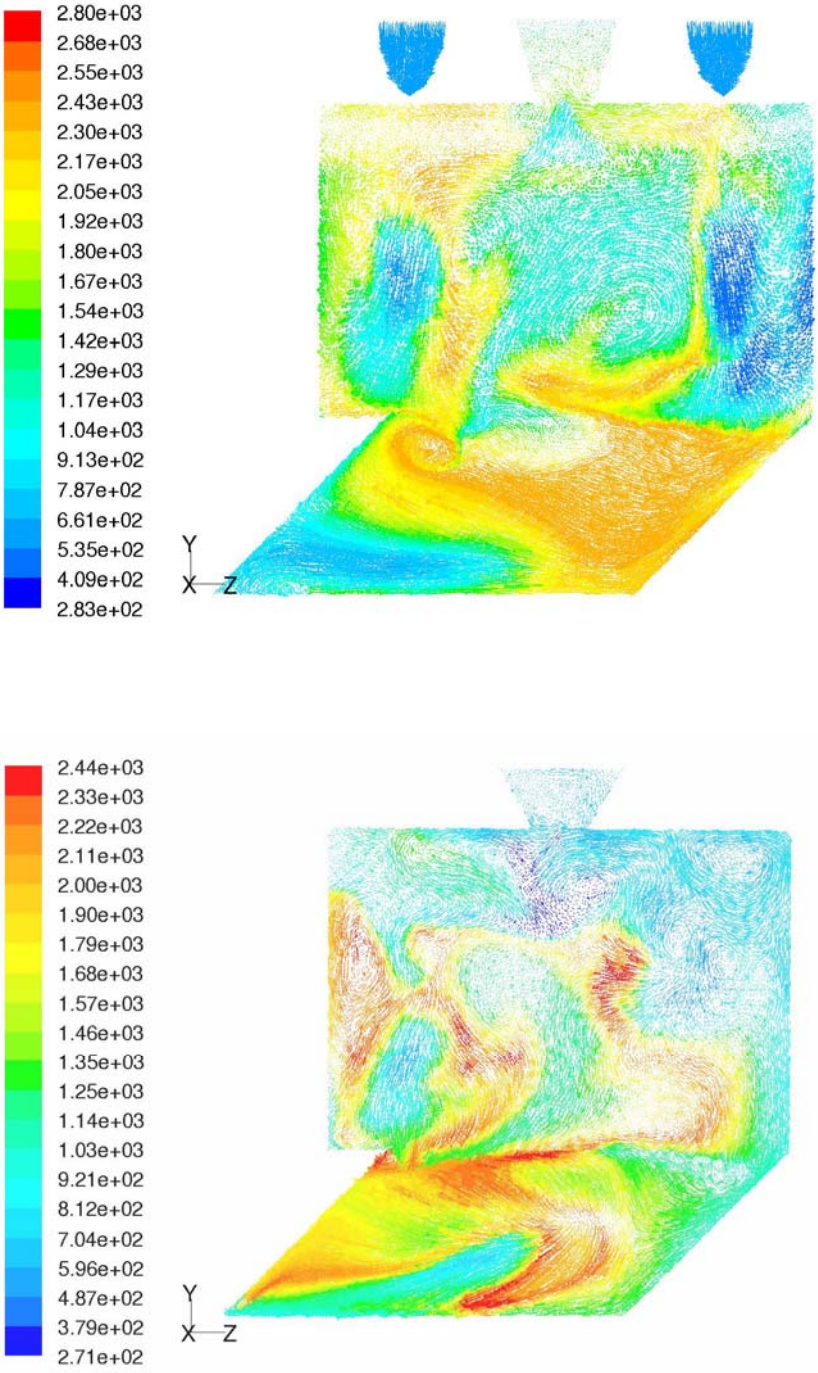

Figure 55: Comparison of 2-D planar sector rig cavity-vane plane (top, cavity flow out of page) and 3-D baseline configuration cavity-vane plane (bottom, cavity flow out of page). Velocity vectors colored with temperature (K), LMLP condition.

where the portion near the upper RVC area is experiencing shear from the cavity exhaust upstream. This has weakened the vortex's structure and intensity. A set of secondary, smaller swirling vortices have formed beneath it at mid vane height and lower (from close-in inspection of velocity vectors). The cavity-vane plane view demonstrates the cavity is not burning very much in the central area, but more along the rear wall and bottom areas, just as observed with the 2-D planar baseline configuration. The large main flow entrainment into the cavity exhaust area is also strongly evident, with the effects felt upstream back into the cavity-vane plane vicinity.

The U_θ plane plot of tangential velocity by radius is given in Figure 56. This plot displays smooth acceleration as radius decreased, until the area of the cavity air inlet jet impingement peaks, which in this case contain the largest radial range for a maximum

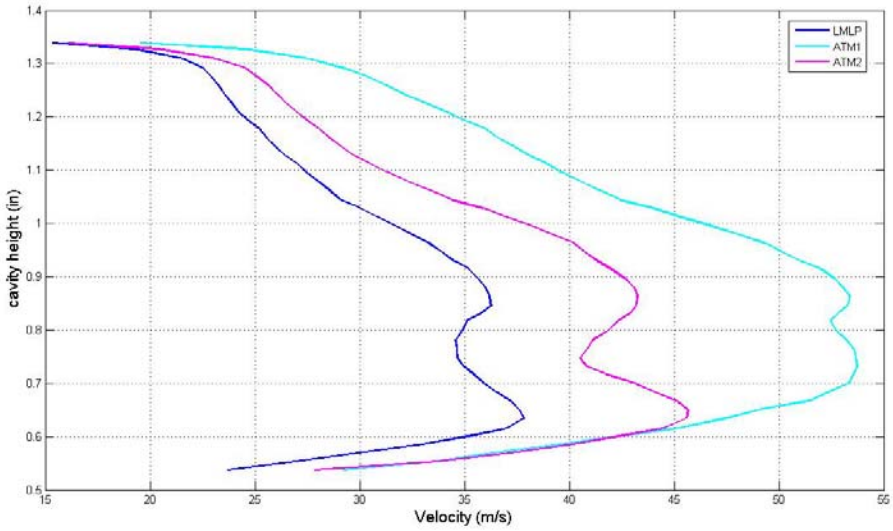

Figure 56: Circumferential averaged tangential velocities plotted by radius on U_θ plane for 2-D planar sector rig.

tangential velocity, with this configuration only lacking the greater magnitude of velocity of the 3-D baseline configuration. The long, decelerating tails of the plotted profiles are again a result of the RVC vortex effects in the lower cavity at the axial vane. Overall, the cavity-vane parameters for the 2-D planar sector rig reasonably reproduce the 3-D configurations flow characteristics, at a lower level of turbulent intensity, but sufficient to merit experimental analysis.

4.5.4 Exhaust Temperature Distribution Evaluation. Table 19 displays the data for pattern factor of the 2-D planar sector rig in comparison with the 3-D baseline configuration. The LMLP condition, with associated 30% reduced outlet mass flow, has achieved a large temperature drop in both average and maximum outlet temperatures, but the pattern factor increases. The two atmospheric pressure conditions show little change. The qualitative analysis of the outlet plane temperature contours is accomplished examining Figure 52 for the LMLP condition, showing in fact the maximum temperature is reduced, and the dilution zone burning has come to an earlier conclusion, reducing the temperature signature on the outlet plane. The observed hot area's center is just above the mid-line level, creating a useable temperature profile with the hottest spot and corresponding band likely just above the mid-line.

Table 19: Exhaust temperature pattern factor data for 2-D planar sector rig, comparing with 3-D baseline configuration.

Op Cond	Model	T_{4avg}	T_{4max}	Pattern Factor
LMLP	3-D Baseline	1151.96	2428.74	2.06
	Planar Sct Rig	883.74	2053.07	3.32
ATM1	3-D Baseline	1064.43	2330.46	2.38
	Planar Sct Rig	1027.78	2339.22	2.64
ATM2	3-D Baseline	1073.25	2342.39	2.34
	Planar Sct Rig	1069.11	2347.27	2.38

V. Conclusions

5.1 Overview of Research Results

A computational fluid dynamics (CFD) numerical model was developed, building upon previous research, to improve the detail and accuracy of a steady state flow solution for the centrifugal-force enhanced Ultra Compact Combustor concept using *FLUENT* commercial CFD software. Solutions on the experimental configuration of the UCC were compared with experimental data from testing at AFRL Propulsion Directorate to verify the model accuracy. This CFD model was then used in the development of two UCC sector rig designs for use in experimentally evaluating internal flow dynamics and characteristics not able to be directly measured or observed on the full axi-symmetric UCC test rig.

5.1.1 CFD Modeling. The CFD model developed first utilized greatly increased cell density on the numerical grid to increase the detail and resolution of turbulent flow details of the combusting flow. The dense grid was found not only to improve the turbulent flow detail, but to also allow increased transport of species and flow dynamics throughout the solution space, as evidenced by the accurate exhaust temperature distribution profiles compared with the coarse grid CFD model.

The second CFD modeling area of investigation was the comparison of the standard k-ε turbulence model with the RNG k-ε turbulence model containing enhancements for greater accuracy in highly strained and swirling flow. This analysis on the UCC experimental configuration for a steady state solution produced greatly

improved detail and resolution in the turbulent characteristics for the RNG *k-ε* model, but at the expense of decreased solution stability. The transient nature of the UCC turbulent flow and the similar transient nature of the highly responsive RNG *k-ε* turbulence model produced solutions at varying stages of convergence residual levels and performance criteria over a long series of iterations, similar to what an unsteady, time accurate CFD solution would be. The greater solution detail of the RNG *k-ε* turbulence model is better suited to predicting experimental flow measured using high accuracy laser diagnostic methods, and was used throughout this research.

5.1.2 3-D UCC Flow Analysis. A detailed analysis of both the experimental configuration and a modified baseline configuration modeled as 60 degree axi-symmetric periodic sections was conducted using experimental operating conditions. Previously unresolved flow characteristics were identified. The anticipated buoyancy bubbles of hot and cold pockets in the cavity primary combustion zone resulting from centrifugal-force combustion effects at high g-loadings were clearly defined. Shed vortices generated by the axial vane's radial-vane-cavity (RVC) drawing combusting gases from the cavity into the main flow and then trailing along the axial vane while conducting dilution zone burning were found to be the primary transport avenue of combustion products to the combustor exhaust outlet. An additional vortex was evident located midway between the axial vanes, exchanging mass between the main flow and cavity, and served as the main source of main flow entrainment into the cavity.

Tangential velocity and g-loading profiles by radius for a cavity cross-section flow were measured and analyzed, revealing a smooth gradient of velocity and

centrifugal-force effects exists, generally decreasing as radius increases in the cavity. Exhaust outlet temperature distribution patterns of improved accuracy were produced, revealing a suitable profile exists, with the distribution pattern a direct resultant of the shed vortex from the RVC carrying combustion products to the exhaust.

5.1.3 Design of UCC Sector Rigs. To enable experimental measurement and observation of the shed vortices and other turbulent flow characteristics below the cavity radius in the main flow of the UCC, sector test rigs were designed with a rectangular main channel flow shape for placement of quartz crystal walls on two sides to allow laser diagnostic visual access to these flow phenomena. An intermediate 2-D flat cavity configuration was first developed and modeled with periodic cavity flow to evaluate the planar model concept. Subsequently, two non-recirculating sector rigs were designed, each with the cavity section doubled in length, leading into a single section main flow area, to simulate cavity mass flow entrainment. The resulting sector rigs are the 2-D curved cavity and 2-D planar cavity sector rigs. Each sector rig was simulated with the CFD model at one experimental operating and two atmospheric pressure operating conditions for comparison with the 3-D baseline model. Analysis of the sector rig CFD solutions showed cavity and cavity-vane flow characteristics consistent with the 3-D baseline model, but with decreased turbulent intensity, therefore meeting the goal of reproducing the full UCC cavity-vane effects for experimental observation.

5.2 Future Research

In addition to the aforementioned experimental testing on the designed UCC sector rigs to examine the cavity-vane flow interaction and current research efforts, other avenues of research of interest are identifiable from the results found here.

CFD is increasingly becoming the design tool of choice, therefore improvement of the numerical models used and a further use of its capabilities are important in the UCC development. The limits of the steady state CFD modeling are evidenced in the transient nature of the RNG k-ε turbulence modeling used here. This turbulence model is well suited to model unsteady, transient flows of the nature of the UCC, so its use in developing a time accurate solution is a logical step in the overall design process. Despite this, excellent utility exists in the steady state modeling, as developed here, to guide and evaluate UCC configuration adjustments toward combustor optimization. Additionally, validation and improvements to the modeling of the fuel droplet size, two-phase interaction and evaporation in the CFD modeling can lead to further fuel spray optimization.

Appendix A: 3-D Baseline Configuration Flow Cutaways ATM2

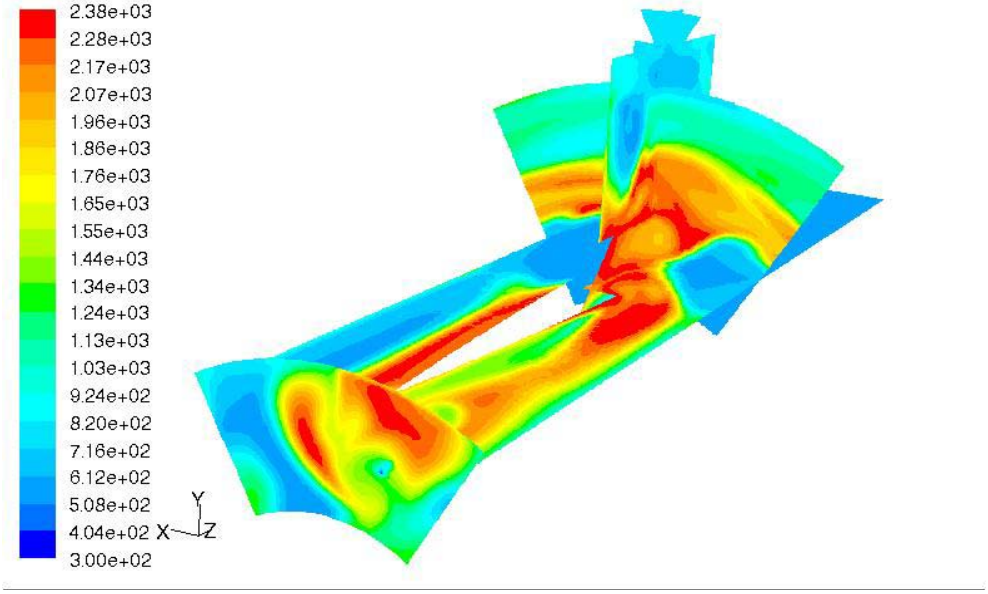

Figure 57: Contours of temperature (K) on 3-D baseline configuration, ATM2 operating condition.

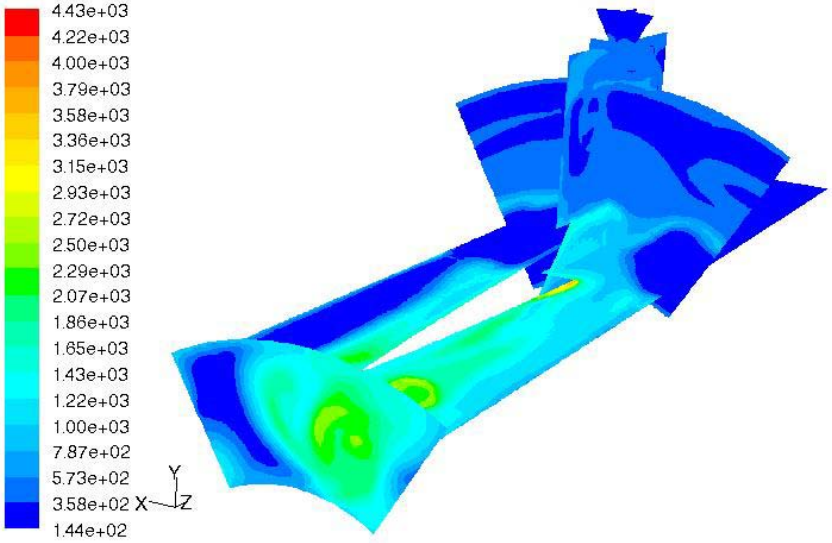

Figure 58: Contours of turbulence intensity (%, read as e+01) on 3-D baseline configuration, ATM2 operating condition.

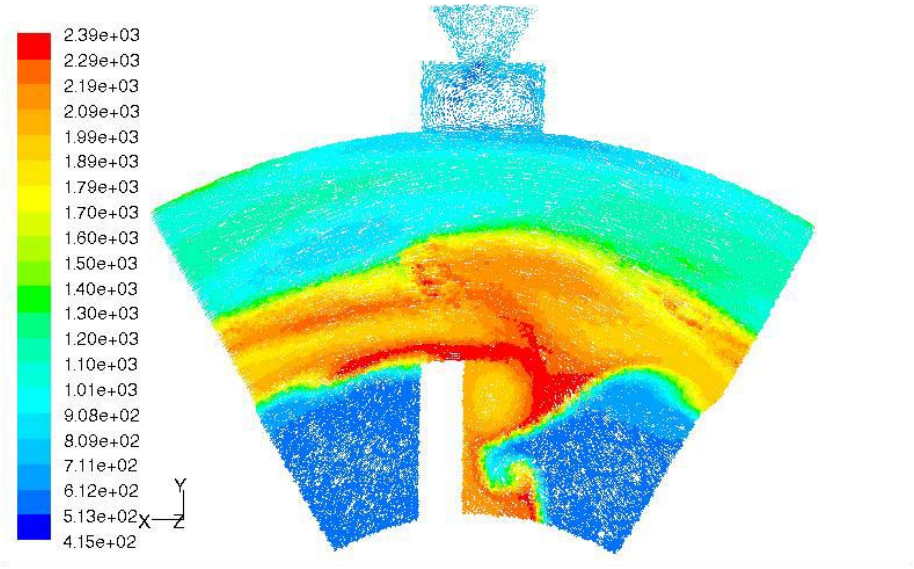

Figure 59: Velocity vectors with temperature (K) on cavity fuel plane for 3-D baseline configuration, ATM2 operating condition. Viewed from exhaust, cavity flow is clockwise.

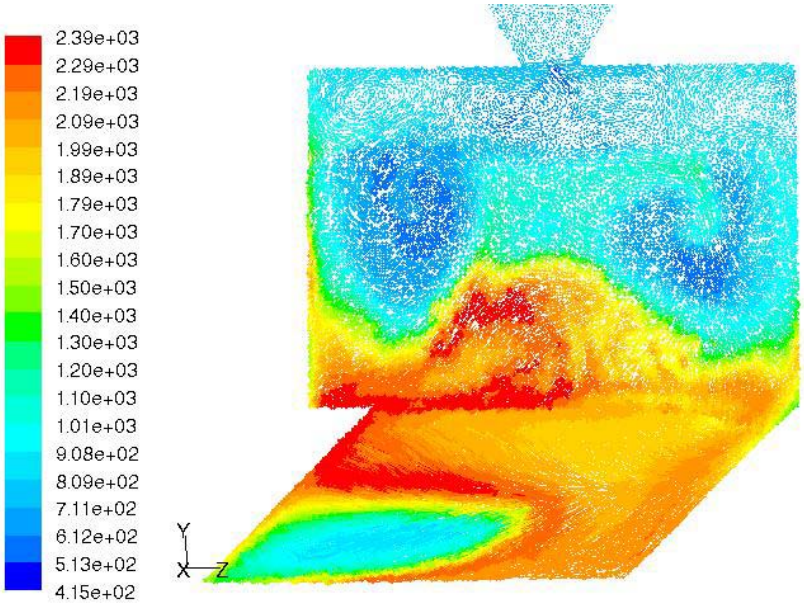

Figure 60: Velocity vectors with temperature (K) on cavity-vane plane for 3-D baseline configuration, ATM2 operating condition. Cavity flow is out of page.

Appendix B: 2-D Curved Cavity Sector Rig Flow Cutaways ATM2

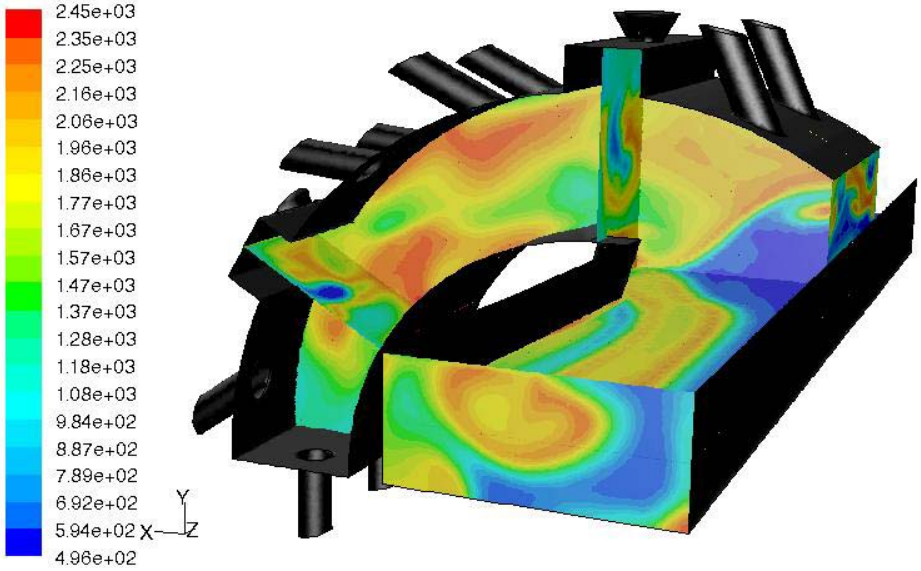

Figure 61: Contours of temperature (K) on 2-D curved cavity sector rig, ATM2 operating condition.

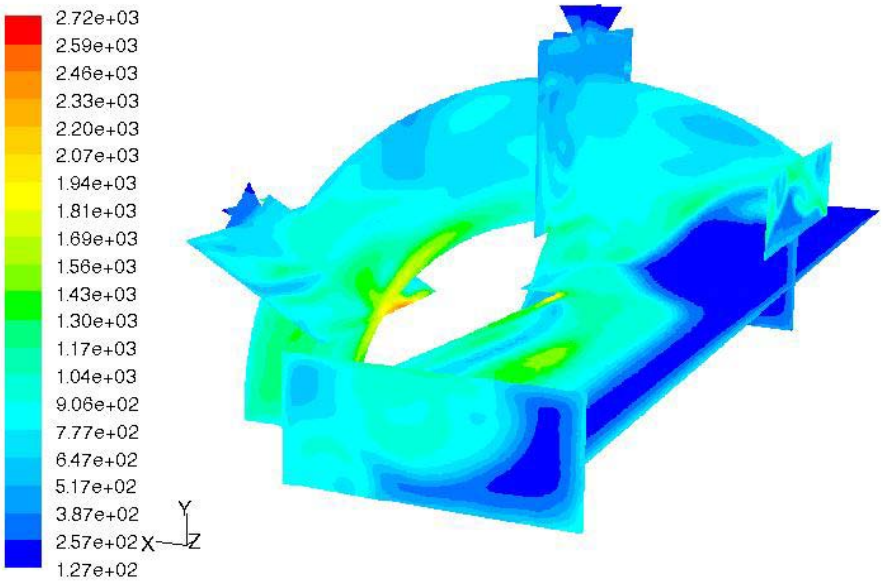

Figure 62: Contours of turbulence intensity (%, read as e+01) on 2-D curved cavity sector rig, ATM2 operating condition.

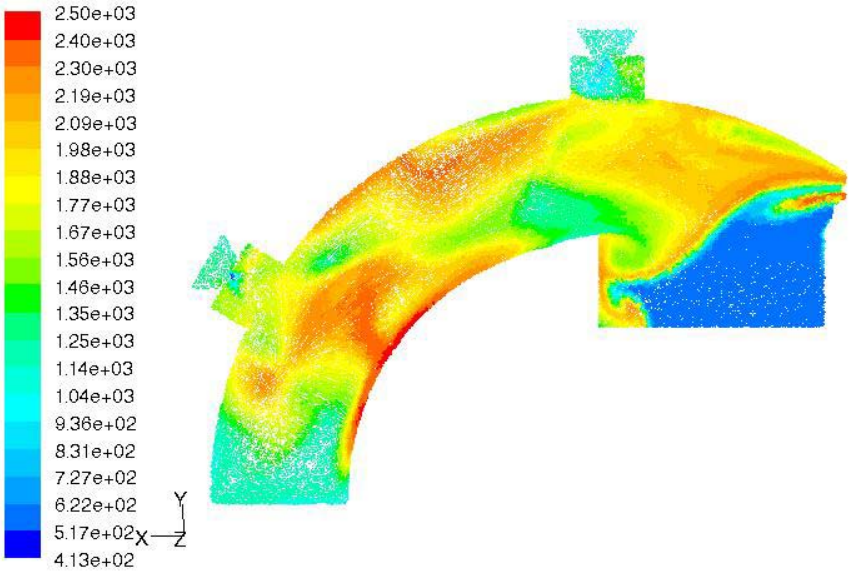

Figure 63: Velocity vectors with temperature (K) on cavity fuel plane for 2-D curved cavity sector rig, ATM2 operating condition. Viewed from exhaust, cavity flow is clockwise, left to right.

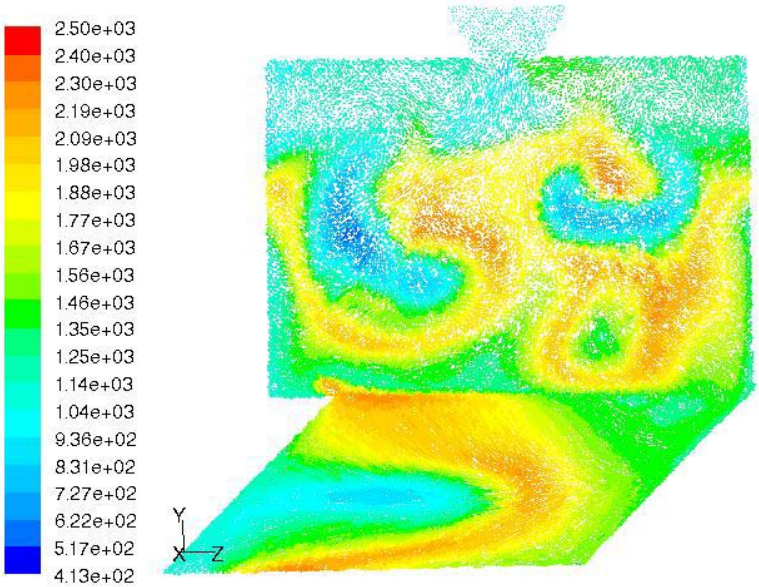

Figure 64: Velocity vectors with temperature (K) on cavity-vane plane for 2-D curved sector rig , ATM2 operating condition. Cavity flow is out of page.

Appendix C: 2-D Planar Cavity Sector Rig Flow Cutaways ATM2

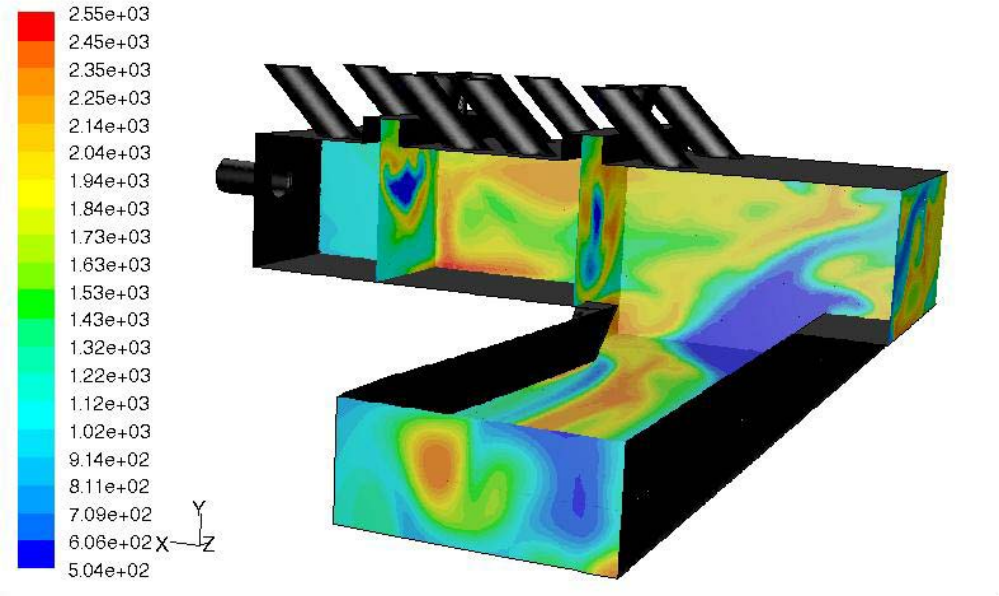

Figure 65: Contours of temperature (K) for 2-D planar cavity sector rig, ATM2 operating condition.

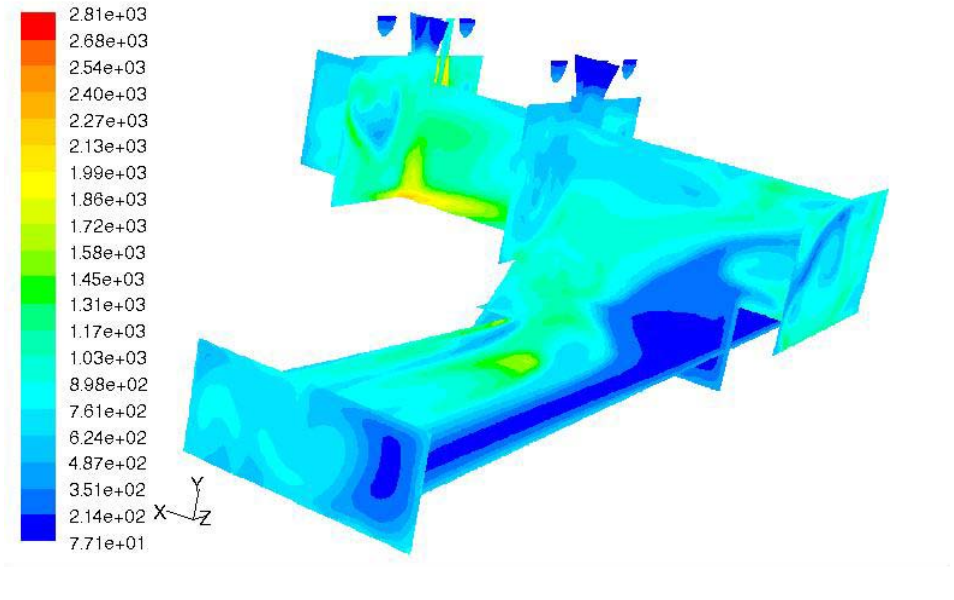

Figure 66: Contours of turbulence intensity (%, read as e+01) for 2-D planar cavity sector rig, ATM2 operating condition.

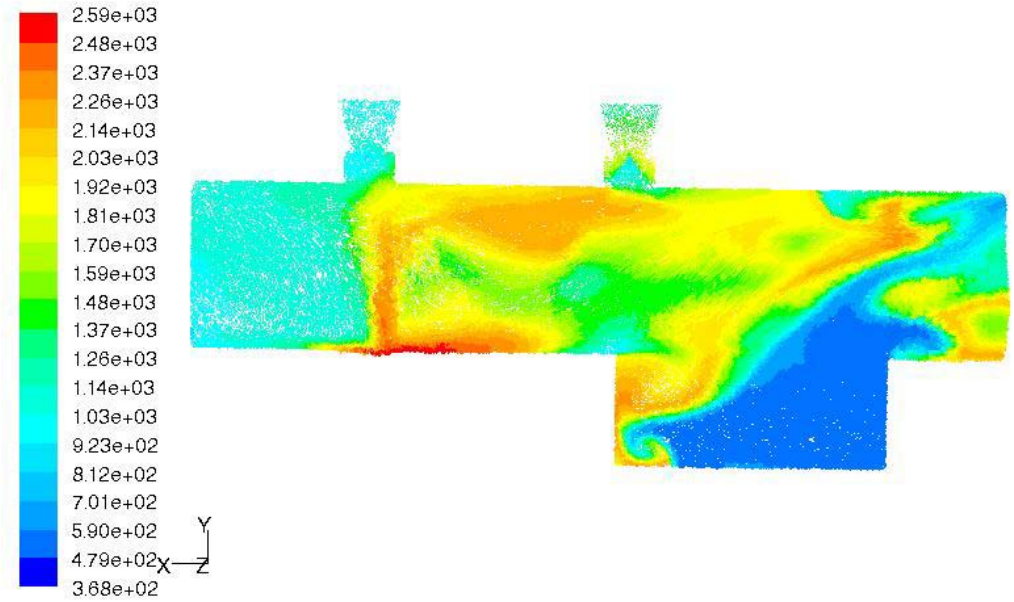

Figure 67: Velocity vectors with temperature (K) on cavity fuel plane for 2-D planar cavity sector rig, ATM2 operating condition. Viewed from exhaust, cavity flow is left to right.

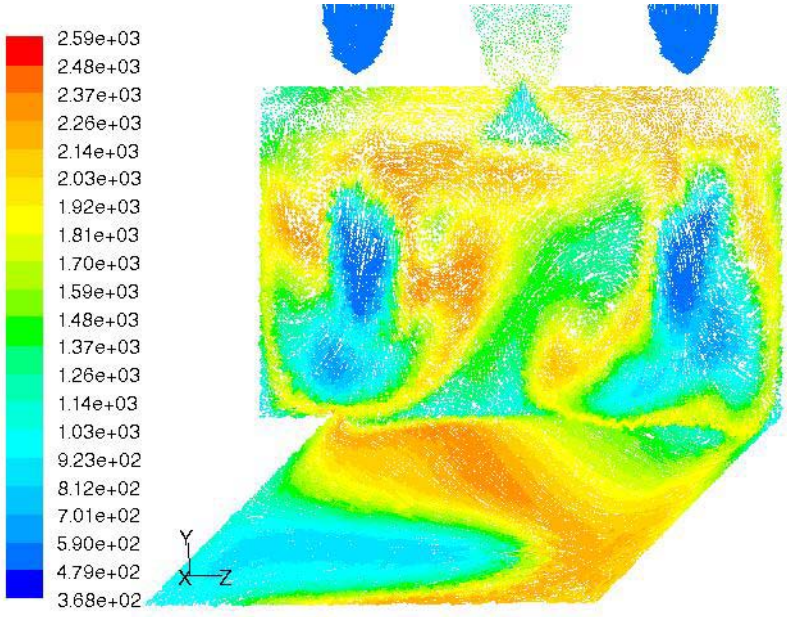

Figure 68: Velocity vectors on cavity-vane plane for 2-D planar cavity sector rig, ATM2 operating condition. Cavity flow is out of page.

Bibliography

Anisko, Jonathon. *Numerical Investigation of Cavity-Vane Interactions Within the Ultra Compact Combustor.* Master's thesis, Graduate School of Engineering, Air Force Institute of Technology (AU), Wright-Patterson AFB OH, March 2006. AFIT/GAE/ENY/06-M01.

Anthenien, R.A., R.A. Mantz, W.M. Roquemore, and G. Sturgess. "Experimental Results for a Novel, High Swirl, Ultra Compact Combustor for Gas Turbine Engines". Air Force Research Laboratory, Wright-Patterson AFB OH, 2001.

ARP1533. "Procedure for the Calculation of Gaseous Emissions from Aircraft Turbine Engines". *Society of Automotive Engineers*, June 1996.

Filipiak, Mark. "Mesh Generation". Edinburgh Parallel Computing Centre, The University of Edinburgh, Version 1.0, November 1996.

----. *FLUENT 6.2 User's Guide*. Fluent Inc., Lebanon NH, January 2005.

Greenwood, Roger T. *Numerical Analysis and Optimization of the Ultra Compact Combustor.* Master's thesis, Graduate School of Engineering, Air Force Institute of Technology (AU), Wright-Patterson AFB OH, March 2005. AFIT/GAE/ENY/05-M10.

Heywood, John B. *Internal Combustion Engine Fundamentals*. McGraw Hill, 1988.

Hsu, K.-Y., L.P. Goss, and W.M. Roquemore. "Characteristics of a Trapped-Vortex Combustor". *Journal of Propulsion and Power*, Volume 14, No. 1, January-February 1998.

Incropera, Frank P. and David P. DeWitt. *Fundamentals of Heat and Mass Transfer.* John Wiley and Sons, Inc, fifth edition, 2002.

Lefebvre, Arthur H. *Gas Turbine Combustion.* Hemisphere Publishing Corporation, 1983.

Lewis, George D. *Centrifugal-Force Effects on Combustion.* Pratt and Whitney Aircraft, West Palm Beach, FL, 1973.

Little, B.H. and R.R. Whipkey. "Locked Vortex Afterbodies". *Journal of Aircraft*, Volume 16, No. 5, May 1979.

Liu, Feng and William A. Sirignano. “Turbojet and Turbofan Engine Performance Increases Through Turbine Burners”. AIAA-2000-0741, January 2000.

Mawid, M.A., T.W. Park, H. Thornburg, B. Sekar, and J. Zelina. “Numerical Analysis of Inter-Turbine Burner (ITB) Concepts for Improved Gas Turbine Engine Performance”. AIAA 2005-1162, January 2005.

Mawid, M.A., H. Thornburg, B. Sekar, and J. Zelina. “Performance of an Inter-Turbine Burner (ITB) Concept with Three-Different Vane Cavity Shapes”. AIAA 2006-4740, July 2006.

Quaale, Ryan J., Ralph A. Anthenien, Joseph Zelina, and Jeffrey Ehret. “Flow Measurements Within a High Swirl Ultra Compact Combustor for Gas Turbine Engines”. ISABE-2003-1141.

Roquemore, W.M., Dale Shouse, Dave Burrus, Art Johnson, V.R. Katta, G.J. Strugess, and Illari Vihinen. “Trapped Vortex Combustor Concept for Gas Turbine Engines”. AIAA 2001-0483, January 2001.

Sirignano, W.A. and F. Liu. “Performance Increases for Gas-Turbine Engines Through Combustion Inside the Turbine”. *Journal of Propulsion and Power*, Volume 15, No. 1, January-February 1999.

Zelina, Joseph, Dale T. Shouse, and Craig Neuroth. “High Pressure Tests of a High-g, Ultra-Compact Combustor”. AIAA 2005-3779, July 2005.

Zelina, Joseph, G.J. Sturgess, Adel Manour, and Robert D. Hancock. “Fuel Injector Design for an Ultra-Compact Combustor”. ISABE-2003-####.

Zelina, Joseph, G.J. Sturgess, and Dale T. Shouse. “The Behavior of an Ultra-Compact Combustor (UCC) Based on Centrifugally-Enhanced Turbulent Burning Rates”. AIAA 2004-3541, July 2004.

Vita

LCDR David S. Moenter graduated from Fountain Valley (CA) High School in 1987. He was selected for an NROTC scholarship and attended the University of Southern California, graduating in May 1991 with a Bachelor of Science in Aerospace Engineering, a minor in Astronomy, and earning his commission as an Ensign in the U.S. Navy.

LCDR Moenter was selected for Naval Aviation pilot training, subsequently earning his 'Wings of Gold' as an unrestricted Naval Aviator in November 1993 upon completion of the helicopter pilot training pipeline. Following fleet replacement squadron training for the H-46D helicopter, he reported to his first operational assignment with Helicopter Combat Support Squadron FIVE (HC-5), on Guam, in November 1994. His three year assignment included two Arabian Gulf shipboard deployments in support of Operations Desert Storm and Southern Watch.

LCDR Moenter's next assignments included Helicopter Training Squadron EIGHTEEN (HT-18), Pensacola, Florida, as a helicopter flight instructor, December 1997 to October 2000, a ship's company as Air Officer aboard the USS Ogden (LPD-5), November 2000 to May 2002, deploying for Operation Enduring Freedom, and finally another fleet squadron tour as a department head with Helicopter Combat Support Squadron ELEVEN (HC-11) from September 2002 to July 2004, deploying as Detachment THREE OIC aboard the USS Bridge (AOE-10) for Operation Iraqi Freedom in 2003.

REPORT DOCUMENTATION PAGE

Form Approved
OMB No. 074-0188

1. REPORT DATE *(DD-MM-YYYY)*	**2. REPORT TYPE**	**3. DATES COVERED** *(From – To)*
08-09-2006	**Master's Thesis**	Jan. 2006 - Sept 2006

4. TITLE AND SUBTITLE

Design and Numerical Simulation of Two Dimensional Ultra Compact Combustor Model Sections for Experimental Observation of Cavity-Vane Flow Interactions

5a. CONTRACT NUMBER

5b. GRANT NUMBER

5c. PROGRAM ELEMENT NUMBER

6. AUTHOR(S)

Moenter, David S., Lieutenant Commander, USN

5d. PROJECT NUMBER

5e. TASK NUMBER

5f. WORK UNIT NUMBER

7. PERFORMING ORGANIZATION NAMES(S) AND ADDRESS(S)

Air Force Institute of Technology
Graduate School of Engineering and Management (AFIT/EN)
2950 Hobson Way
WPAFB OH 45433-7765

8. PERFORMING ORGANIZATION REPORT NUMBER

AFIT/GAE/ENY/06-S07

9. SPONSORING/MONITORING AGENCY NAME(S) AND ADDRESS(ES)

AFOSR/NA
Dr. Julian Tishkoff
801 N. Randolph Street
Arlington, VA 22203-7765

10. SPONSOR/MONITOR'S ACRONYM(S)

11. SPONSOR/MONITOR'S REPORT NUMBER(S)

12. DISTRIBUTION/AVAILABILITY STATEMENT

APPROVED FOR PUBLIC RELEASE; DISTRIBUTION UNLIMITED.

13. SUPPLEMENTARY NOTES

14. ABSTRACT

An improved computational fluid dynamics (CFD) model was developed for numerical simulation of the Ultra Compact Combustor (UCC) concept to enhance turbulent flow characterization of the circumferentially traveling, centrifugal-force enhanced combustion, cavity flow into the engine main flow passage via a radial cavity in the turbine axial guide vanes. The CFD model uses a dense grid on a 60^{o} periodic, axi-symmetric combustor section, with the RNG k-ε turbulence model to resolve turbulent flow details. An overall analysis and performance evaluation of the experimentally tested UCC configuration and an axially shortened cavity baseline configuration was conducted at various experimentally documented operating conditions.
This CFD model is then applied in designing two sector test rigs to simulate a portion of the UCC flow to allow optical access to the cavity-vane flow interaction, an area inaccessible on a full test rig. The design steps include a 2-D planar, periodic model eliminating centrifugal-force effects and the design of two non-periodic test sections with an extended cavity simulating mass entrainment before interacting with the cavity-vane and main flow. The planar and curved sector rigs were evaluated and cavity flow parameters analyzed at experimental and atmospheric conditions for comparison with the 3-D baseline configuration.

15. SUBJECT TERMS

Combustion, Combustors, Computational Fluid Dynamics, Turbulent Flow, Emissions, Efficiency.

16. SECURITY CLASSIFICATION OF:			**17. LIMITATION OF ABSTRACT**	**18. NUMBER OF PAGES**	**19a. NAME OF RESPONSIBLE PERSON**
REPORT	**ABSTRACT**	**c. THIS PAGE**			Ralph A. Anthenien, Jr., ENY
U	**U**	**U**	**UU**	163	**19b. TELEPHONE NUMBER** *(Include area code)* (937) 255-6565,

Standard Form 298 (Rev: 8-98)

Prescribed by ANSI Std. Z39-18